DEVELOPMENT OF A SELF-CONSISTENT COUPLED ATOMISTIC-CONTINUUM MODEL TO STUDY THE BRITTLE AND DUCTILE FRACTURE IN METALLIC MATERIALS.

by

Subhendu Chakraborty

A dissertation submitted to The Johns Hopkins University in conformity with the requirements for the degree of Doctor of Philosophy.

Baltimore, Maryland

March, 2020

Abstract

Modeling fracture and failure of material is a complex phenomenon that needs atomic-scale understanding of the kinetics and energetics of different deformation mechanisms. Several efforts has been made over the years to model the fracture at continuum scale e.g, cohesive zone model, phase-field model. The success of these continuum scale fracture models rely on the appropriate incorporation of the interaction between the crack and the different deformation mechanisms within the material such as interatomic decohesion, dislocation nucleation, mobility of the dislocations, dislocation reaction, twining etc. Hence, there is a need to develop a systematic framework to quantify these interactions and develop physics-based constitutive laws that can be used in continuum scale fracture models.

This dissertation develops a concurrent coupled atomistic-continuum model to capture the interaction between different deformation mechanisms on the propagation of crack. The atomistic region is modeled using time-accelerated Molecular Dynamics(MD) and for the continuum region, the density-based Crystal Plasticity Finite Element(CPFE) model is used. Hyperdynamics is used for the time accelera-

tion of the MD. The atomistic-continuum coupling is achieved by enforcing geometric compatibility and force equilibrium in the interface region. A sequence of steps is performed to characterize and quantify the dislocations at the interface and then transfer those dislocations from the atomistic to the continuum region in the density form. The propagation of the dislocations in the density form is modeled by solving the transport equation of a conserved quantity, also known as the advection equation. The mesh-less Reduced Kernel Particle Method(RKPM) is used to solve the advection equation over the continuum domain.

The developed concurrent coupled atomistic-continuum model is used to study the brittle and ductile propagation of a crack in a nickel single crystal. A parametrized form of crack propagation law and the evolution of dislocation density is extracted from the model. The concurrent model has also been used to construct the free energy functional of the phase-field model where the evolution of different energy contributions during the fracture process is obtained. These evolution laws can be employed in full continuum scale models to study the fracture process at a larger spatial scale.

Thesis Committee

Professor Somnath Ghosh (Primary Advisor)

Department of Civil and Mechanical Engineering

Johns Hopkins University, Baltimore

Professor Todd C. Hufnagel

Department of Material Science and Engineering

Johns Hopkins University, Baltimore

Professor Jaafar El-Awady

Department of Mechanical Engineering

Johns Hopkins University, Baltimore

Professor James K. Guest

Department of Civil Engineering

Johns Hopkins University, Baltimore

Acknowledgments

I would like to express my heartfelt gratitude to my PhD advisor, Prof. Somnath Ghosh, for his unwavering support and encouragement throughout my PhD study. His dedication for science and passion for research was evident in many fruitful discussions. The technique of problem-solving and critical thinking that I have learned from him will definitely help me in my future professional life.

I am grateful to Prof. Hufnagel, Prof. Guest and Prof. El-Awady for being in my thesis committee. I am thankful to Shinu, Rajeev, Jasim, Kamal and Vignesh for their help during my early years here in USA. Jiaxi was a wonderful partner in my research, I am thankful to him for many wonderful discussion and fruitful guidance at the beginning of my PhD. I also want to thank George, Deniz, Xiaohui, Maxwell, Jinlei, Xiaofan, Shravan, Preetam, Saikat, Maloth, Arunava, Arunjyoti, Chandra, Qingcheng and previous lab members of CMRL for their help and the good time that we had together.

I want to express my appreciation to Mike Bernard and Kevin Adams for their help whenever I asked for it. The financial support provided by the Air Force Office

of Scientific Research Structural Mechanics and Prognosis Program through Grant No. FA-RT1645 (Program Manager: Dr. J. Tiley) and the computer supports provided by the Homewood High Performance Computing Center (HHPC) and Maryland Advanced Research Computing Center (MARCC) are gratefully acknowledged.

Finally, I would like to express my gratitude to my parents, brother and sister for their encouragement to pursue higher studies and their support during my PhD.

Dedication

I would like to dedicate my work to my parents, sibling and my wife for their unconditional love and support.

Contents

Abstract ii

Acknowledgments v

List of Tables xiii

List of Figures xiv

1 Introduction 1

2 The Concurrent Framework to Couple Molecular Dynamics(MD) with Crystal Plasticity(CP) 9

2.1 Equilibrium equation of the coupled system 11

2.2 Incremental solution of the Coupled Model 15

2.3 Crystal Plasticity based Material model for the Continuum Region . . 17

2.3.0.1 An Unified Expression for the Dislocation Velocity . 26

2.4 Material Model for the Atomistic Region: Time accelerated Molecular Dynamics 28

3 Framework to Transfer and Propagate the Dislocations from the Atomistic to the Continuum 32

3.1 The Framework to Transfer the Dislocations from Atomistic to Continuum at the Interface 33

3.2 Modeling the Propagation of Dislocation in the Density form in the Continuum 38

3.3 Smooth Particle Hydrodynamics(SPH) 40

3.3.1 Kernel Approximation and the Integral Representation of the Interpolation Function 40

3.3.2 Particle Approximation 43

3.3.3 Correction of SPH for finite domain using RKPM method . . 45

3.3.3.1 Reproducing condition for first derivative 50

3.4 Numerical Implementation of the Dislocation Propagation Scheme . . 56

3.4.1 Point Collocation Method 58

3.4.2 Imposing the Boundary Condition 59

3.4.3 Nodal Integration Scheme 60

3.4.4 Stabilizing the Smooth Particle Hydrodynamics method . . . 61

3.4.5 Optimizing the computational cost by seeking for the solution at a localized regions 63

4 Time Acceleration of Molecular Dynamics using Strain Boost Hyperdynamics 67

4.1 Methods of Time-scale Accelerated Molecular Dynamics Simulations . 69

4.1.1 The Parallel Replica Dynamics (PRD) 70

4.1.2 The Temperature Accelerated Dynamics (TAD) 71

4.1.3 Hyperdynamics (HD) 72

4.2 Strain Boost Hyperdynamics 76

4.2.1 Hyperdynamics for driven systems 80

4.2.2 Determination of V_{max} 84

4.2.3 Determination of q_c 87

4.2.4 Determination of N_b 88

4.3 Implementation of the Strain-Boost Hyperdynamics in LAMMPS and Accelerated MD Simulations 90

4.3.1 Validation of the Strain-Boost Hyperdynamics Model with Conventional MD Results 93

4.4 Numerical Simulation of a Crystalline Material with an Embedded Crack 96

4.4.1 MD model of a Single Crystal Nickel with an Embedded Crack 96

4.4.2 Results of Hyperdynamics MD Simulations 99

4.4.2.1 Results for lattice orientation-1 100

4.4.2.2 Results for lattice orientation-2 101

4.5 Concluding Remarks 105

5 Bridging the Time Scale Between the Atomistic and the Continuum Model **109**

5.1 Coupled Accelerated Time Marching Algorithm 110

5.2 Solution Steps in the Coupled Concurrent Problem 112

5.2.1 Anisotropic Elastic Constitutive Model for the Continuum Domain Ω_c 113

5.2.2 Setting up the Initial Configuration of the Atomistic Domain (Ω_A) 115

5.2.3 Steps in Each Load Increment 117

5.3 Validation of the Hyperdynamics Accelerated Concurrent Model . . . 119

5.4 Conclusions 124

6 Extracting the Crack Propagation Law Using the Concurrent Model during Brittle Fracture **127**

6.1 Crack Propagation Simulations at Lower Strain-Rates 128

6.1.1 Effect of Strain-Rate and Temperature on the Crack Propagation-Rate 130

6.1.2 Developing a Phase-Field Model from Multiscale Simulations for Brittle Fracture 132

6.2 Conclusions 137

7 Extracting the Evolution laws for Crack Propagation and Plasticity

Evolution for Ductile Fracture **139**

7.1 Details of the Computational Domain 140

7.1.0.1 Determining the Size of the Computational Domain and the Dislocation Free Zone 140

7.1.0.2 Determining the Size of the Atomistic Domain 142

7.2 Validation and Assessment of the Concurrent Model in comparison with a full MD model 146

7.2.1 Comparison of Critical Stress Intensity Factor for Dislocation Nucleation 149

7.2.2 Comparison of Nucleated Dislocation Density 152

7.2.3 Comparison of Computational Cost 154

7.3 Developing the Evolution Law for the Nucleated Dislocations from the Crack-tip 155

7.4 Deriving the energy functional of the Phase-field model for ductile failure using the concurrent model 161

7.5 Conclusions 167

8 Conclusion And Future Work **169**

Vita **187**

List of Tables

2.1 Slip systems. 19

5.1 Three first order and six second order elastic stiffness coefficients (unit:GPa) of nickel single crystal calibrated in [1, 2]. 115
5.2 A comparative study of the computational cost (expressed in CPU-hours) by hyperdynamics and sub-stepping accelerated MD models at different strain-rates ($\dot{\epsilon}$). (* computed by extrapolation) 125

6.1 Calibrated values of the crack propagation parameters in equation (5.11) from simulations with the concurrent model at different strain-rates. 130
6.2 Comparison of computed values of γ_s on the (100) plane from the concurrent model simulations with reported values in the literature. . 134
6.3 Elastic stiffness coefficients for the phase field simulations. 136

7.1 CPFE material parameters [3]. 148
7.2 Material parameters assosciated with nucleation of crack from a crack tip of nickel single crystal, obtained from [4, 5]. 151
7.3 Comparison of critical SIF(in $MPa.\sqrt{m}$). 152
7.4 Comparison of computational cost between full MD simulation and the concurrent model. 155
7.5 Calibrated values of the dislocation density parameters in equation (7.10) obtained from the simulations with the concurrent model at different strain-rates. 159

List of Figures

1.1 Schematic representation of the interaction between a crack and dislocations inside a grain: (a) polycrystalline domain containing large amount of preexisting dislocation, (b) a micro-crack is nucleated inside a grain causing the creation of a localized dislocation-free zone near the crack, (c) the crack becomes a potential source for new dislocation nucleation. 4

2.1 Schematic representation of the computational domain for concurrent atomistic-continuum simulation, showing models for the atomistic, continuum and interface regions. 10
2.2 Dislocation velocity as function of resolved shear stress: (a) velocity data for a free gliding dislocation inside a nickel perfect crystal is fitted with the functional form of eq. 2.22, (b) velocity profile of a dislocation gliding through preexisting dislocations represented by higher CRSS value. 28
2.3 Details division of the atomistic domain into multiple sub-regions. Showing only the atomistic region. 31

3.1 Steps for extraction of the dislocations from a given atomic configuration. (a) The concurrent model with dislocations in the atomistic region. (b) The dislocations and the stacking fault are identified by using Common Neighbor Analysis(CNA). The red atoms represent the core of the leading and trailing partial dislocations. The blue atoms represent the stacking fault between the two partials. (c) Dislocations are converted from atomic representation to the discrete form. (d) The extracted dislocations are smoothed out to mitigate the noise due to thermal vibration. 35

3.2 Contour plot of the stress due to the presence of a dislocation. Stress due to an edge dislocation (a)σ_{xx}, (b)σ_{yy} and (c)σ_{xy}. The stress due to screw dislocation (d)σ_{xz} and (e)σ_{yz}. (f)The Gaussian distribution used to represent the stretch of the dislocation core. 37
3.3 A dislocation is transformed from it (a)discrete representation to the (b)density form. 38
3.4 KernelFunction associated with a particle located at (a)far from the boundary and (b)close to the boundary. 45
3.5 Reproducing capability of SPH shape function for (a) a linear function, (s) slope of the linear function, (c) sine function and (d) slope of the sine function. 46
3.6 The spatial variation of the RKPM coefficient (a)$\boldsymbol{C(x)}$ *and* (*b*)$\boldsymbol{C'(x)}$ for a 1-D problem. 55
3.7 Reproducing capability of RKPM shape function for (a) a linear function, (s) slope of the linear function, (c) sine function and (d) slope of the sine function. 57
3.8 Instability associated with particle based method while solving the advection equation for the propagation of localized density. (a)The initial Gaussian peak of a scalar density gets (b)distorted due to the instability during the propagation. (c)The same Gaussian peak (d)remains preserved during propagation afer stabilization of the method. 65
3.9 Schematic representation of the local solution domain for the propagation of the dislocation density in the continuum region. 66

4.1 Schematic illustration of the hyperdynamics method. The solid line corresponds to the original system potential, while the biased potential is shown with the dashed line. 73
4.2 Time evolution of potential energy and η^{Mises} of a typical atom in the ensemble at $T = 2K$. 80
4.3 Time evolution of potential energy and η^{Mises} of a typical atom in the ensemble at $T = 300K$. 86
4.4 Plot of the potential energy as a function of applied strain corresponding to different temperatures in the quenching bath for determining q_c. 89
4.5 (a) A 3D atomic domain of single crystal nickel with an embedded crack for MD simulations, and (b) zoomed in view of the boost region for HD based accelerated MD simulations. The color of atoms is based on the second invariant of atomic strain (η_i^{Mises}) corresponding to 1% macroscopic strain. 90
4.6 A flowchart showing the strain-boost hyperdynamics implementation in LAMMPS. Tasks inside the dashed box are added for the hyperdynamics acceleration in conjunction with the conventional MD operations. 91

4.7 Validation of the strain-boost hyperdynamics-based MD model with conventional MD results: Comparisons of (a) volume averaged stress and (b,c)dislocation densities, as a function of the macroscopic strain. 94
4.8 Efficiency of the hyperdynamics-based MD model for different strain-rates and temperatures. 95
4.9 Geometric details of the MD model with boundary conditions: (a) physical representation of the specimen with an embedded crack; crystal orientations with respect to specimen coordinate axes for: (b) orientation-1, and (c) orientation-2. 97
4.10 Initial crack-tip dislocation segments for orientation-1 at strain-rates of (a) $2 * 10^7/sec$ by conventional MD, and (b) $10^4/sec$ by accelerated MD. 103
4.11 Evolution of macroscopic stress as a function of engineering strain for orientation-2 by conventional MD and accelerated MD (AMD). . . . 105
4.12 Snapshots of plastically deformed atomic configuration in orientation-2, ploted using AtomEye [6] with color based on common neighbor analysis (CNA [7]), showing deformation mechanisms at different strain-rates: (a) leading partial nucleation at the onset of plasticity irrespective of strain rate; (b) leading partial followed by another leading partial in the parallel slip plane (twining partial) at high strain-rates, and (c) leading partial is followed by a trailing partial at lower strain-rates. 106

5.1 Time marching scheme for the concurrent coupled model, where the time of atomistic simulation is determined by the strain-boost hyperdynamics. A slower time evolution indicates that the system is very close to an infrequent event to occur. 110
5.2 (a) The 3D computational domain for the concurrent simulation with a crack embedded in it, and (b) expanded view of the crack-tip boost region. Atom color represents the value of the second invariant of the atomic strain (η_i^{Mises}) at 1% macroscopic strain. AtomEye [6] is used for visualization of the atomistic domain. 114
5.3 Computational specimen modeled by the concurrent atomistic-continuum model for crack propagation, (a) geometry and dimensions of the specimen with loading, and (b) discretization of the continuum and atomistic domains. 120
5.4 Comparison of results by the concurrent model with and without hyperdynamics-accelerated MD for an applied strain-rate $\dot{\epsilon} = 10^{07}$: (a) rate of crack propagation as a function of SIF, and (b) strain energy release rate as a function of crack length. 124

6.1 Contour plot of σ_{yy} showing crack advance for volume-averaged strains: (a) $\epsilon_{11} = \epsilon_{22} \approx 1.0\%$, (b) $\epsilon_{11} = \epsilon_{22} \approx 3.3\%$. Stress in the atomistic region corresponds to the per-atom virial stress. 129
6.2 Crack propagation rates as a function of the applied stress intensity factor for different strain-rates: (a) $\dot{\epsilon} = 10^7$ ($K_{IC} = 0.805$ and $c = 0.655$), (b) $\dot{\epsilon} = 10^6$ ($K_{IC} = 0.813$ and $c = 0.634$), (c) $\dot{\epsilon} = 10^4$ ($K_{IC} = 0.823$ and $c = 0.577$). 131
6.3 Strain-rate and temperature dependence of: (a) critical stress intensity factor (K_{IC}) and (b) value of c in equation (5.11). 132
6.4 Evolution of fracture energy and crack length as a function of the applied strain 135
6.5 Comparison of (a) fracture energy and (b) crack length as a function of applied macroscopic strain, by the concurrent and the phase field models with $g_c = 4.6\ J/m^2$. 137

7.1 Resolved shear stress based on LEFM. Spatial distances are in nm and the stress is in GPa. 143
7.2 Determining the size of the atomistic domain Ω_A by studying the stretch of the stacking fault: (a)the coupled model, (b) zoomed in view of the atomistic region. 144
7.3 The variability of the maximum stretch of stacking fault for different strain rates of $\dot{\epsilon} = 1.0e^6$ *and* $1.0e^5$ and two different temperatures of $T = 300K$ *and* $200K$. 145
7.4 Comparison of the performance of the concurrent model with respect to the full MD model: (a)specimen details for the simulation, (b)evolution of dislocation in concurrent and MD model. 147
7.5 Evolution of dislocation density in the concurrent model and the MD model. 154
7.6 Computational specimen modeled by the concurrent atomistic-continuum model for crack propagation,(a) the details of the geometry, the dimensions and loading and (b) discretization of the atomistic and the continuum domain. 157
7.7 Contour plot of the Dislocation Density. At macroscopic strain of (a)$\epsilon_{11} = \epsilon_{22} = 3.1\%$ and (b)$\epsilon_{11} = \epsilon_{22} = 3.4\%$ 158
7.8 Evolution of (a) dislocation density and (b) crack length as a function of applied strain at rate $\dot{\epsilon} = 1.0e6$. 159
7.9 Applied strain rate(in logarithmic scale) and temperature dependence of: (a) critical stress intensity factor (K_{IC}), (b) the value of a_1 and (c) the value of a_2 in Eq. 7.10. 160

7.10 Comparison of the evolution of the crack length and different energies between the concurrent model and the phase field model. Evolution of (a) crack length (b) fracture energy and (c) defect energy as a function of applied macroscopic strain. 165
7.11 Contour plot of the phase-field parameter (s). (a) Initial configuration of the crack. Evolution of the crack at macroscopic strain of $\epsilon_{11} = \epsilon_{22} \approx 3.4\%$ (b)without and (c)with consideration of the additional plasticity contribution from the crack tip. 167

Chapter 1

Introduction

Metallic materials are one of the most widely used structural materials in modern civilization. The usage of metallic materials span across many engineering sectors such as automotive, aerospace, mining, defense etc. Like any other materials, the metals and alloys are also susceptible to failure during its life span. A study conducted in 1983 [8] estimated that the structural failure due to fracture costs the U.S. economy about 119 billion per year. Very recently a series of accidents such as 'Train Derailment at Hatfield in 2000'[9], 'crash of China Airlines Flight 611 in 2002'[10], 'Viareggio train derailment in 2009'[11] etc is a vivid reminder of the loss of life and property that metal fatigue and fracture can incur. These accidents can provide a glimpse of the importance and urgency for the development of better fracture-resistant material. The first step towards this direction is to understand the fracture process at the lowest scale possible and then extract the required information to develop a

robust fracture model to predict the failure.

Modeling the crack growth and plasticity during the ductile failure of metallic material is a crucial requirement to design and develop new structural materials. This is due to the fact that, during ductile failure, the propagation of a crack involves complex interactions between the crack and the other deformation mechanisms. Hence, for any successful model, it is of utmost importance to capture this interaction as accurately as possible. The plastic deformation mechanisms are governed by phenomena like interatomic decohesion, dislocation nucleation, mobility of the dislocations, dislocation reaction, etc. These phenomena can be modeled accurately at the atomic length scale using molecular statics(MS) or molecular dynamics(MD). Due to this, to computationally model the fracture in metallic materials, the atomic length scale can be considered as a good starting point to accurately capture the interaction between the crack and the other plastic deformation mechanisms.

Figure 1.1 shows a schematic representation of a typical interplay between a crack and dislocations. Most of the structural metallic materials are polycrystalline in nature. These polycrystalline materials consist of preexisting dislocations within individual grains (figure1.1(a)). Under mechanical loading(monotonic or cyclic), the deformation of the material mainly involves elastic bond stretch and plastic slip due to the preexisting dislocations. At this stage, dislocation density evolves mainly due

to the expansion of the dislocation loop and subsequent reaction with other dislocations. As dislocations start to form a cluster around a localized region within a grain, the region becomes a potential location for the development of a micro-crack (figure 1.1(b)). Due to the high stress gradient around the crack tip, a localized region is created which is free form preexisting dislocations. Preexisting dislocations near the crack is either driven further due to the high shear stress near the crack tip or dislocations annihilates at the free surface of the crack. Upon further loading, the crack-tip itself becomes a potential source of new dislocations (figure 1.1(c)). These nucleated dislocations play a major role in the material behavior and ultimate failure of the material. Hence for any successful continuum-based fracture model, accurate incorporation of the plastic contribution from these nucleated dislocations is necessary.

Molecular dynamics (MD) is one of the most effective simulation tools currently in use to investigate the behavior of many materials at the atomistic scale. With increasing computational power, large scale atomistic simulations are routinely being conducted with several million or even billion atomic systems, e.g. in [12, 13] to study deformation and fracture in metallic systems. MD simulations have been used to study deformation mechanisms due to crack tip plasticity at finite temperatures in [14, 15, 16]. One of the major limitations of the MD based study is the spatial length scale that can be modeled using MD is limited to the micron scale. A way-out from this bottleneck of MD based model is to couple the MD with continuum-based noel

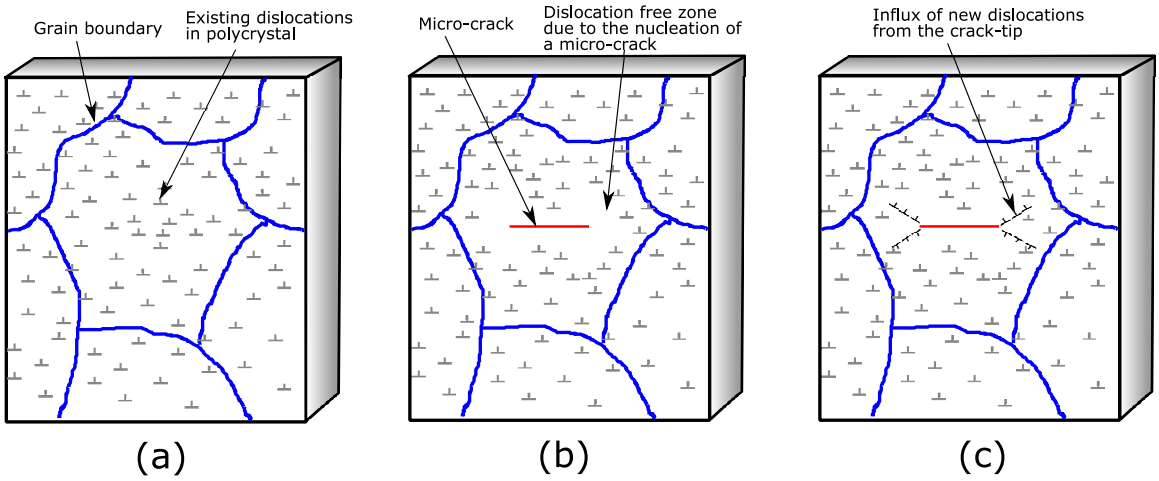

Figure 1.1: Schematic representation of the interaction between a crack and dislocations inside a grain: (a) polycrystalline domain containing large amount of preexisting dislocation, (b) a micro-crack is nucleated inside a grain causing the creation of a localized dislocation-free zone near the crack, (c) the crack becomes a potential source for new dislocation nucleation.

within a concurrent framework.

Concurrent multiscale models combine lower scale atomistic models with continuum descriptions at higher scales into a single, coupled description for a simultaneous depiction of the material behavior at multiple scales [17, 18, 19, 20]. Regions of the computational domain that exhibit critical or extreme events like cracks or twins are modeled at the atomistic resolution, while the rest corresponding to macroscopic loading is treated with continuum laws. The subdomains of atomistic resolution are typically modeled using discrete methods like molecular statics (MS) or molecular dynamics (MD). On the other hand, the lower resolution computational domain is typically represented by continuum models, e.g. elasticity models in [18, 21, 19, 1, 2]. Concurrent models are able to simulate larger spatial domains than what is typically

accommodated in pure atomistic simulations. These models allow both the atomistic and continuum simulations to evolve simultaneously, often with traction reciprocity and displacement compatibility enforced in the interface region between the two subdomains. This interface region works as a platform for information transfer between the discrete and continuum models. In these regions, the atomistic model simulations provide displacement boundary conditions for nodal points of the continuum simulation model, e.g. finite element model, that are located in the interface. The continuum nodes, on the other hand, provide traction boundary conditions for atoms in the interface region of the atomistic domain. Several methods have been developed to couple the atomistic and the continuum scale. These methods differ mainly on the type of model that is being used for the continuum scale and the information that is being passed from the atomistic to the continuum region. A detailed overview of these different methods can be found in [22]. In it's simplest form, the continuum region is modeled using linear elasticity [17, 23, 21, 20, 24, 19, 15] or nonlinear elasticity [2, 1, 25]. Plasticity is either completely ignored in both the atomistic and the continuum region or is limited only within the atomistic region.

Very recently efforts have been made to incorporate dislocation based plasticity in both the atomistic as well as in the continuum region [26, 27, 28]. In [26], a coarse-graining technique using the rhombohedral 3D element is used so that the element boundary will coincide with the slip planes of the fcc crystal. The use of this special type of rhombohedral 3D element facilitates the passage of dislocations from

the atomistic to the continuum region and also maintain the plane of propagation for the individual dislocations. In [27], the nonlocal quasicontinuum [29] method is extended to incorporate the adaptive refinement of a localized continuum region up to the atomic resolution. Due to this adaptivity, any local region can be represented at an atomic resolution as defects migrate from one region to another. In ($CADD-3D$) [28, 30, 31], 3D Discrete-Dislocation Dynamics is used to model the plasticity in the continuum region. In this method, an atomistic template of the dislocation core structure is used to transfer the dislocations from the atomistic to the continuum region at the interface. One common feature in the above-mentioned methods is that each dislocation needed to be represented and traced individually. This may increase the computational cost significantly as the simulation progresses. The problem would become intractable, as the simulation progresses, due to the continuous incoming of dislocation flux from the atomistic to the continuum region. Contrary to this, the dislocations in the continuum region can be represented in the density form and density-based crystal plasticity [32, 33] model can be used to model the continuum region of the concurrent model.

In this work, a novel method is developed to incorporate the crystal plasticity within the framework of coupled concurrent atomistic-continuum model[2, 1, 25]. In this method, the continuum region is modeled using a density-based crystal plasticity model [32, 33, 34, 3, 35]. A sequence of steps is performed to characterize [16], quantify and transfer the dislocations at the interface from their discrete representation to the

density form. Once in the continuum region, the propagation of the dislocation in the density form is modeled by solving the transport equation of a conserved quantity, also known as advection equation. The concept of representing a dislocation in the density form inherently incurs a large spatial density gradient to represent the core of the dislocation. A finite element based approach to solving the advection equation for dislocation propagation would necessitate a very fine mesh that is computationally prohibitive. For this reason, a mesh-less method is adopted here. The Reduced Kernel Particle Method(RKPM) along with point collocation and nodal integration technique is used to solve the advection equation for the dislocation propagation.

Another major limitation for dynamics simulations with these concurrent models is the inherent time-scale mismatch between the atomistic and continuum domains. Time integration schemes used in MD simulations, e.g. the Verlet algorithm, use extremely small time-steps that are governed by the time-scale ($\approx$ 1-10 *pico-seconds (ps)*) of atomic vibrations. It limits the largest time step that can be used to numerically integrate the equations of atomic motion to approximately $1-10$ *femto-seconds (fs)*. This is orders of magnitude smaller than time steps typically used for continuum simulations of materials subjected to high strain-rate loading. This discrepancy requires the two sub-domains to experience strain-rates that differ by several orders of magnitude. The underlying deformation mechanisms at different strain-rates are generally different [36] and hence, extrapolating predictions from simulations at discrepant strain-rates can lead to erroneous inferences. Various efforts have been made

to bridge the time-scale mismatch between atomistic and continuum models, one of them being the time acceleration of atomistic domain evolution. In the present study, a variant of Hyperdynamics named 'Strain Boost Hyperdynamics' [37] is incorporated to accelerate the time evolution of the atomistic domain. A time matching algorithm is developed to make sure that the time evolution after each load increment in both the atomistic and the continuum region is the same.

The concurrent model is used to study the evolution of a crack embedded within a Nickle single crystal and the nucleation of dislocations from the crack tip. A three-parameter evolution equation for dislocation density is adopted to quantify the evolution of the dislocation density. The strain rate and temperature dependence of the parameters are also investigated. The work also outlines an approach to use this concurrent atomistic-continuum model to augment the free energy density functional of the phase-field model. The equivalence of dynamics and energetics of the crack between the concurrent model and the phase-field model is used to derive some critical phase field parameters.

Chapter 2

The Concurrent Framework to Couple Molecular Dynamics(MD) with Crystal Plasticity(CP)

The computational domain in the concurrent model is divided into three sub-domains, As depicted in figure 2.1. They are the continuum domain of finite element (FE) simulations (Ω_C), the atomistic domain of MD simulations (Ω_A) and a *interface* handshake domain ($\Omega_I = \Omega_A \bigcap \Omega_C$). Ω_I is needed to impose constraints of kinetic reciprocity and kinematic compatibility between the MD and FE simulation domains. MD simulations are carried out by the parallel Large-scale Atomic/Molecular Massively Parallel Simulator *LAMMPS* [38]. The FE model in Ω_C uses a dislocation density-based crystal plasticity constitutive model. Inertia effects are neglected in

the FE analysis of the continuum domain under quasi-static conditions. Ω_I is comprised of a layer of finite elements with nodes characterized as interface nodes and a band of underlying interface atoms. Each FE node in the interface region is associated with a group of atoms that are located inside of a Voronoi cell, generated by 3D Voronoi tessellation involving neighboring nodes [39]. Compatibility conditions are enforced between each interface FE node and the associated group of interface atoms. Spatially-averaged displacements of interface atoms are equated to the displacement fields of the interface FE node for atom-node compatibility.

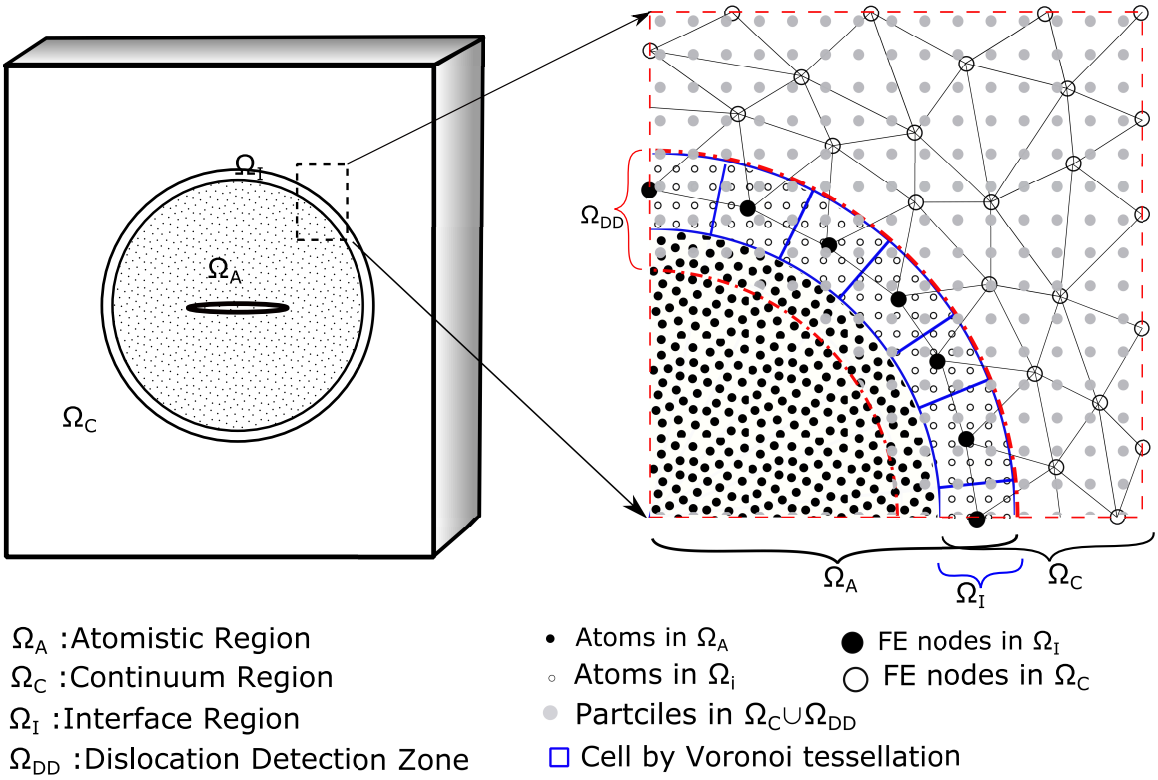

Figure 2.1: Schematic representation of the computational domain for concurrent atomistic-continuum simulation, showing models for the atomistic, continuum and interface regions.

2.1 Equilibrium equation of the coupled system

The equilibrium condition under quasi static condition is obtained by minimizing the total potential energy of the system. An incremental formulation is adopted here. The incremental energy of the whole system has contribution from the continuum Ω_C , the atomistic Ω_A and the interface region Ω_I as:

$$\Delta\Pi_{tot} = \Delta\Pi_C + \Delta\Pi_A + \Delta\Pi_I \tag{2.1}$$

where $\Delta\Pi_C$, $\Delta\Pi_A$, $\Delta\Pi_I$ are the potential energy functionals in Ω_C, Ω_A and Ω_I respectively. The contribution from the continuum domain Ω_C is expressed as,

$$\Delta\Pi_C = \int_{\Omega_C} \boldsymbol{S} : \Delta\boldsymbol{E} d\Omega - \int_{\partial\Omega_C} \boldsymbol{T} \cdot \Delta\boldsymbol{u}^C d\partial\Omega = \{\boldsymbol{f}_{\text{C-int}} - \boldsymbol{f}_{\text{C-ext}}\} \cdot \{\Delta\boldsymbol{u}^C\} \tag{2.2}$$

where, $\boldsymbol{S}$ is the second Piola-Kirchoff stress and $\boldsymbol{E}$ is the Green-Lagrange strain tensor. $\boldsymbol{S}$ is the energy conjugate of $\boldsymbol{E}$. $\boldsymbol{T}$ is the externally applied traction loading on the surface Ω_C. $\boldsymbol{f}_{\text{C-ext}}$ and $\boldsymbol{f}_{\text{C-int}}$ are the external and internal force vector at FE nodes in ω_C. $\Delta\boldsymbol{u}^C$ is the incremental nodal displacement vector in ω_C. There are other energy conjugate measure of stress and corresponding measure of deformation, they are related as:

$$\int_{\Omega_0} \boldsymbol{S} : \Delta \boldsymbol{E} d\Omega = \int_{\Omega_0} \boldsymbol{P} : \Delta \boldsymbol{F} d\Omega = \int_{\Omega} \boldsymbol{\sigma} : \Delta \boldsymbol{D} d\Omega \tag{2.3}$$

where, $\boldsymbol{P}$, $\boldsymbol{F}$, $\boldsymbol{\sigma}$ and $\boldsymbol{D}$ are the first Pikola-Kirchoff stress, deformation gradient tensor, Cauchy's stress and rate of deformation tensor respectively. It should be noted that third term has it's integration over the deformed configuration Ω while other two has their integration over the reference configuration Ω_0. A detailed discussion on the construction of $\boldsymbol{S}$ and $\boldsymbol{E}$ will be provided during the discussion on the crystal plasticity based material model for the continuum region in section 2.3.

The second term in equation 2.1, i.e, the incremental energy contribution coming from the atomistic region is gives as,

$$\Delta \Pi_A = \sum_{p \in \Omega_A} \Delta \Phi_p(\bar{\boldsymbol{r}}) - \sum_{p \in \Omega_A} \boldsymbol{f}^p_{\text{A-ext}} \cdot \Delta \bar{\boldsymbol{r}}_p \tag{2.4}$$

Here, $\Delta \Phi_p(\bar{\boldsymbol{r}})$ is the increment in the potential energy of the atomistic system due to the inter-atomic interaction between an atom p with position vector $\boldsymbol{r}$ and it's neighbors. $\boldsymbol{f}^p_{\text{A-ext}}$ is the increase in the potential due to the externally applied force other than the inter-atomic interaction. A detailed discussion of different kinds of external forces that the atomic domain experience is discussed in section 2.4. The third term in equation 2.1 i.e, $\Delta \Pi_A$ is the contribution from the interface region Ω_I due to the constrain of maintaining geometric continuity at the interface. Lagrange multiplier method is used to impose this constrain as,

$$\Delta\Pi_I = \sum_{\beta\in\Omega_I} \boldsymbol{\lambda}_\beta \cdot \boldsymbol{C}_\beta \tag{2.5}$$

where, $\boldsymbol{\lambda}_\beta$ is the set of set of Lagrange multiplier associated to the constraint $\boldsymbol{C}_\beta$. The constrain function $\boldsymbol{C}_\beta$ can be described as the displacement of any interface node β is equal to the average displacement of all the atoms belonging to the associated Voronoi cell G_β, as shown in figure 2.1. The compatibility constraint can be written as:

$$C_\beta(\Delta\boldsymbol{u}^C, \Delta\boldsymbol{u}^A) = \Delta\boldsymbol{u}^C_\beta - \sum_{p\in G_\beta} w_p \cdot \Delta\boldsymbol{u}^A_p = 0 \quad \forall\beta \in \Omega_I \tag{2.6}$$

where $\boldsymbol{u}^A_p = \boldsymbol{r_p} - \boldsymbol{r^0_p}$ and $\boldsymbol{u}^C_\beta$ are the displacement of an atom p and the interface node β respectively. w_p is a weighting function corresponding to the contribution of an atom p in the Voronoi cell G_β to the weighted average displacement. It is expressed as $w_p = \frac{1}{N_\beta}$, where N_β is the total number of atoms in G_β.

The equilibrium configuration of the coupled system is obtained by invoking the variational principle, i.e, the first variation of the total potential in equation 2.1 is equal to zero. Substituting equations 2.2, 2.4 and 2.5 into equation 2.1 and taking

the first variation, the equilibrium equation becomes,

$$\frac{\partial \Delta \Pi_{tot}}{\partial \Delta u^i_\alpha} = f^i_\alpha = \begin{cases} (f^i_\alpha)_{\text{int}} - (f^i_\alpha)_{\text{ext}} + \lambda^i_\alpha & \text{for node } \alpha \in \Omega_I \\ (f^i_\alpha)_{\text{int}} - (f^i_\alpha)_{\text{ext}} & \text{for node } \alpha \in \Omega_C \backslash \Omega_I \end{cases} = 0 \tag{2.7a}$$

$$\frac{\partial \Delta \Pi_{tot}}{\partial \Delta \bar{r}^i_p} = f^i_p = \begin{cases} \frac{\partial \Delta \Phi(\boldsymbol{r})}{\partial \Delta \bar{u}^i_p} - (f^i_p)_{\text{ext}} - w_p \lambda^i_\alpha & \text{for atom } p \in G_\alpha \text{ in } \Omega_I \\ \frac{\partial \Delta \Phi(\boldsymbol{r})}{\partial \Delta \bar{u}^i_p} - (f^i_p)_{\text{ext}} & \text{for atom } p \in \Omega_A \backslash \Omega_I \end{cases} = 0 \tag{2.7b}$$

where $i = 1, 2, 3$ represent directions in a fixed reference coordinate system. In equation (2.7a) the total conjugate force f^i_α at a node α is from contributions $(f^i_\alpha)_{\text{int}}$ due to strain energy, external forces $(f^i_\alpha)_{\text{ext}}$ and Lagrange multipliers λ^i_α. The latter represents reaction force due to compatibility constraint on node α from the atoms in Ω_A. f^i_p represents the total force on an atom p in Ω_A due to contributions from interatomic interaction $(\frac{\partial \Delta \Phi(\boldsymbol{r})}{\partial \Delta \bar{u}^i_p})$, external applied force $((f^i_p)_{\text{ext}})$ and the compatibility constraint force to an atom p $(w_p \lambda^i_\alpha)$, where w_p is a weighting function. The constraint relation is given as:

$$(\lambda^i_\alpha)^C + (\sum_{p \in G_\beta} w_p \lambda^i_\alpha)^A = 0 \tag{2.8}$$

2.2 Incremental solution of the Coupled Model

A staggered solution approach is implemented for the coupled concurrent model. It seeks equilibrium conditions of the continuum and atomistic domains sequentially with force and displacement compatibility enforced at the interface. Equilibrium of the continuum domain is first achieved with subsequent equilibrating of the atomistic domain by letting the system evolve dynamically for a predetermined period of time. The equation (2.7a) is solved incrementally by the FE method with interface traction reciprocity and displacement compatibility constraints by using successive iteration. For a time increment $t \rightarrow t + \Delta t$ let $\Delta \boldsymbol{U}^C(t) = \boldsymbol{U}^C(t + \Delta t) - \boldsymbol{U}^C(t)$ be the FE nodal solution to the incremental displacement field in Ω_C. $\Delta \boldsymbol{U}^C(t)$ can be further decomposed into two groups belonging to complementary sub-domains as:

$$\Delta \boldsymbol{U}^C(t) = \begin{Bmatrix} \Delta \boldsymbol{U}^{C_I}(t) \\ \Delta \boldsymbol{U}^{C_O}(t) \end{Bmatrix} \tag{2.9}$$

where $\Delta \boldsymbol{U}^{C_I}(t)$ is the nodal displacement in Ω_I prescribed from the solution of the atomistic domain following equation (2.6), and $\Delta \boldsymbol{U}^{C_O}(t)$ is the displacement increments of all other FE nodes. The discretized equilibrium equation (2.7a) is then given

as:

$$\begin{Bmatrix} \boldsymbol{f}_{\text{int}}^{C_I}(t+\Delta t) \\ \boldsymbol{f}_{\text{int}}^{C_O}(t+\Delta t) \end{Bmatrix} - \begin{Bmatrix} \boldsymbol{f}_{\text{ext}}^{C_I}(t+\Delta t) \\ \boldsymbol{f}_{\text{ext}}^{C_O}(t+\Delta t) \end{Bmatrix} + \begin{Bmatrix} \boldsymbol{\lambda}(t+\Delta t) \\ 0 \end{Bmatrix} = 0 \tag{2.10}$$

$\boldsymbol{f}_{\text{int}}^{C_I}$ and $\boldsymbol{f}_{\text{int}}^{C_O}$ are internal nodal force vectors in Ω_{C_I} and Ω_{C_O} respectively, while $\boldsymbol{f}_{\text{ext}}^{C_I}$ and $\boldsymbol{f}_{\text{ext}}^{C_O}$ correspond to applied loads on $\partial\Omega_{C_I}$ and $\partial\Omega_{C_O}$ respectively. $\boldsymbol{\lambda}$ corresponds to the Lagrange multipliers due to displacement constraints in Ω_I. In a linearized incremental formulation, these vectors are additively decomposed as:

$$\begin{aligned} \{\boldsymbol{f}_{\text{int}}^{C}(t+\Delta t)\} &= \{\boldsymbol{f}_{\text{int}}^{C}(t)\} + \{\Delta\boldsymbol{f}_{\text{int}}^{C}\} \\ \{\boldsymbol{f}_{\text{ext}}^{C}(t+\Delta t)\} &= \{\boldsymbol{f}_{\text{ext}}^{C}(t)\} + \{\Delta\boldsymbol{f}_{\text{ext}}^{C}\} \\ \{\boldsymbol{\lambda}(t+\Delta t)\} &= \{\boldsymbol{\lambda}(t)\} + \{\Delta\boldsymbol{\lambda}\} \end{aligned} \tag{2.11}$$

Higher order terms are neglected in the linearized iterative solution. For the $k-th$ iteration, the internal nodal force vector $\{\Delta\boldsymbol{f}_{\text{int}}^{C}\}$ are expressed in terms of the infinitesimal nodal displacement vector $\{\Delta\boldsymbol{U}^{C}\}$ as:

$$\{\Delta\boldsymbol{f}_{\text{int}}^{C}\}^k = \{\frac{\partial\Delta\boldsymbol{f}_{\text{int}}^{C}}{\partial\Delta\boldsymbol{U}^{C}}\}^k \cdot \{\Delta\boldsymbol{U}^{C}\}^k = [\boldsymbol{K}^{C}]^k\{\Delta\boldsymbol{U}^{C}\}^k \tag{2.12}$$

where $[\boldsymbol{K}^C]^k$ is the tangent stiffness matrix. Since the system is equilibrated at time t, the incremental form of equation (2.10) in the $k-th$ iteration is written as:

$$\begin{bmatrix} \boldsymbol{K}^{C-II} & \boldsymbol{K}^{C-IU} \\ \boldsymbol{K}^{C-UI} & \boldsymbol{K}^{C-UU} \end{bmatrix}^k \begin{Bmatrix} \Delta \boldsymbol{U}^{C_I} \\ \Delta \boldsymbol{U}^{C_U} \end{Bmatrix}^k - \begin{Bmatrix} 0 \\ \Delta \boldsymbol{f}_{\text{ext}}^{C_U} \end{Bmatrix}^k + \begin{Bmatrix} \Delta \boldsymbol{\lambda} \\ 0 \end{Bmatrix}^k = 0 \tag{2.13}$$

Here it is assumed that the interface boundary $\partial\Omega_{C_I}$ is free from any external load. The Newton-Raphson method is applied to iteratively solve equation (2.13). Constraint forces at the interface FE nodes $(\lambda_\alpha^i)^C$ are evaluated upon attaining equilibrium in Ω_C. Subsequently, the atomistic domain configuration Ω_A is updated for the incremented atomic forces $(\sum_{p\in G_\beta} w_p \lambda_\alpha^i)^A$ in the interface Ω_I.

2.3 Crystal Plasticity based Material model for the Continuum Region

The continuum region of the computation domain is modeled based on a density-based crystal plasticity material model. The material consists of a pure nickel single crystal with an fcc lattice structure. The plasticity in the fcc is mainly originated due to the dislocation activity within the material. For fcc type of crystal, there are four slip planes, each slip plane has three slip directions for full dislocations. A statistical dislocation density-based crystal plasticity material model proposed in [32, 33] and

further developed in [34, 3, 35] for Nickel is adopted in this study.

For large deformation, the kinematics of the deformation involves elastic stretching, rotation of the crystal and plastic slip. The deformation gradient $\mathbf{F}$ is multiplicatively decomposed in two components. One is due to the elastic deformation $\mathbf{F_e}$ and the other one is due to the plastic slip $\mathbf{F_p}$ which is incompressible. i.e,

$$\mathbf{F} = \mathbf{F_e}\mathbf{F_p} \quad , \; det(\mathbf{F_p}) = 1; \tag{2.14}$$

The elastic part contains both the lattice rotation $\mathbf{R}$ and elastic stretch $\mathbf{U_e}$, i.e, $\mathbf{F^e} = \mathbf{R_e}\mathbf{U_e}$. Then the rate of elastic and plastic deformation gradient becomes,

$$\dot{\mathbf{F}}_\mathbf{e} = \mathbf{L}\mathbf{F_e} - \mathbf{F_e}\mathbf{L_p} \;\text{ and }\; \dot{\mathbf{F}}_\mathbf{p} = \mathbf{L_p}\mathbf{F_p} \tag{2.15}$$

where $\mathbf{L} = \dot{\mathbf{F}}\mathbf{F^{-1}}$ and $\mathbf{L_p} = \dot{\mathbf{F}}_\mathbf{p}\mathbf{F_p^{-1}}$. For dislocation mediated plasticity, $\mathbf{L_p}$ can be expressed in terms of plastic shear rate $\dot{\gamma}^\alpha$ on α slip system as:

$$\mathbf{L_p} = \dot{F}_p F_p^{-1} = \sum_{\alpha=1}^{N} \dot{\gamma}^\alpha \mathbf{m_0^\alpha} \otimes \mathbf{n_0^\alpha} = \sum_{\alpha=1}^{N} \dot{\gamma}^\alpha \mathbf{s_0^\alpha} \tag{2.16}$$

where, $\mathbf{s_0^\alpha} \equiv \mathbf{m_0^\alpha} \otimes \mathbf{n_0^\alpha}$ is called Schmid tensor. $\mathbf{m_0^\alpha}$ and $\mathbf{n_0^\alpha}$ are the slip direction and slip plane normal in reference configuration. FCC crystal structure has three slip planes represented by slip plane normal $\mathbf{m_0^\alpha}$. Each slip planes have three slip directions represented by $\mathbf{n_0^\alpha}$. Table 2.1 shows the slip system details for the fcc crystal.

Slip system no.	Slip direction $\mathbf{m}_\mathbf{0}^\alpha$	Slip plane normal $\mathbf{n}_\mathbf{0}^\alpha$	Tangent vector $\mathbf{t}_\mathbf{0}^\alpha$
1	$\frac{1}{\sqrt{2}}\left[1\ \bar{1}\ 1\right]$	$\frac{1}{\sqrt{3}}\left[1\ 1\ 1\right]$	$\frac{1}{\sqrt{6}}\left[2\ \bar{1}\ \bar{1}\right]$
2	$\frac{1}{\sqrt{2}}\left[\bar{1}\ 1\ 0\right]$	$\frac{1}{\sqrt{3}}\left[1\ 1\ 1\right]$	$\frac{1}{\sqrt{6}}\left[\bar{1}\ \bar{1}\ 2\right]$
3	$\frac{1}{\sqrt{2}}\left[1\ 0\ \bar{1}\right]$	$\frac{1}{\sqrt{3}}\left[1\ 1\ 1\right]$	$\frac{1}{\sqrt{6}}\left[\bar{1}\ 2\ \bar{1}\right]$
4	$\frac{1}{\sqrt{2}}\left[1\ 0\ 1\right]$	$\frac{1}{\sqrt{3}}\left[1\ \bar{1}\ \bar{1}\right]$	$\frac{1}{\sqrt{6}}\left[\bar{1}\ \bar{2}\ 1\right]$
5	$\frac{1}{\sqrt{2}}\left[0\ 1\ \bar{1}\right]$	$\frac{1}{\sqrt{3}}\left[1\ \bar{1}\ \bar{1}\right]$	$\frac{1}{\sqrt{6}}\left[2\ 1\ 1\right]$
6	$\frac{1}{\sqrt{2}}\left[\bar{1}\ \bar{1}\ 0\right]$	$\frac{1}{\sqrt{3}}\left[1\ \bar{1}\ \bar{1}\right]$	$\frac{1}{\sqrt{6}}\left[\bar{1}\ 1\ \bar{2}\right]$
7	$\frac{1}{\sqrt{2}}\left[\bar{1}\ 0\text{‘}\bar{1}\right]$	$\frac{1}{\sqrt{3}}\left[\bar{1}\ \bar{1}\ 1\right]$	$\frac{1}{\sqrt{6}}\left[1\ \bar{2}\ \bar{1}\right]$
8	$\frac{1}{\sqrt{2}}\left[0\ 1\ 1\right]$	$\frac{1}{\sqrt{3}}\left[\bar{1}\ \bar{1}\ 1\right]$	$\frac{1}{\sqrt{6}}\left[\bar{2}\ 1\ \bar{1}\right]$
9	$\frac{1}{\sqrt{2}}\left[1\ \bar{1}\ 0\right]$	$\frac{1}{\sqrt{3}}\left[\bar{1}\ \bar{1}\ 1\right]$	$\frac{1}{\sqrt{6}}\left[1\ 1\ 2\right]$
10	$\frac{1}{\sqrt{2}}\left[\bar{1}\ 0\ 1\right]$	$\frac{1}{\sqrt{3}}\left[\bar{1}\ 1\ \bar{1}\right]$	$\frac{1}{\sqrt{6}}\left[1\ 2\ 1\right]$
11	$\frac{1}{\sqrt{2}}\left[0\ \bar{1}\ \bar{1}\right]$	$\frac{1}{\sqrt{3}}\left[\bar{1}\ 1\ \bar{1}\right]$	$\frac{1}{\sqrt{6}}\left[\bar{2}\ \bar{1}\ 1\right]$
12	$\frac{1}{\sqrt{2}}\left[1\ 1\ 0\right]$	$\frac{1}{\sqrt{3}}\left[\bar{1}\ 1\ \bar{1}\right]$	$\frac{1}{\sqrt{6}}\left[1\ \bar{1}\ \bar{2}\right]$

Table 2.1: Slip systems.

The elastic stress-strain response is derived by invoking the second Piola-Kirchoff stress tensor $\mathbf{S}$ and it's work conjugate Green-Lagrange strain tensor $\mathbf{E_e}$. A nonlinear elastic stress-strain relation, that has been developed in [1, 2] is used. The constitutive law is given as,

$$\mathbf{S} = \mathbf{C}\left(\mathbf{E_e}\right) : \mathbf{E_e} \tag{2.17}$$

where, $\mathbf{C}\left(\mathbf{E_e}\right)$ is the fourth order nonlinear elasticity tensor. The second Piola-Kirchoff stress $\mathbf{S}$ and the Green-Lagrange strain tensor $\mathbf{E_e}$ are defined as,

$$\mathbf{S} \equiv det(\mathbf{F_e})\mathbf{F_e^{-1}}\sigma\mathbf{F_e^{-T}} \text{ and } \mathbf{E_e} \equiv \frac{1}{2}\left(\mathbf{F_e^T F_e} - \mathbf{I}\right) \tag{2.18}$$

I is the identity tensor and σ is the Cauchy stress tensor.

The plastic shearing rate $\dot{\gamma}^{\alpha}$ is calculated by using Orowan equation [40]. $\dot{\gamma}^{\alpha}$ has a contribution from two different types of dislocations. One is due to the evolution of the pre-existing dislocations and the other one is due to the free glide of the dislocations nucleating from the crack tip. The region near the crack tip experience a high gradient of stress field and the continuum region is located at a significant distance from the crack tip. Hence the preexisting dislocations can be considered as Statistically Stored Dislocation(SSD) and the dislocations nucleating from the crack tip can be considered as Geometrically Necessary Dislocation(GND). Then the plastic shearing rate $\dot{\gamma}^{\alpha}$ can be decomposed into two parts. One due to the preexisting dislocations and their evolution and the second part is due to the dislocations nucleated from the crack tip. i.e,

$$\dot{\gamma}^{\alpha} = \dot{\gamma}^{\alpha}|_{SSD} + \dot{\gamma}^{\alpha}|_{nucl} \tag{2.19}$$

The shearing rate in α slip system due to the preexisting dislocations which are SSD in nature can be expressed as,

$$\dot{\gamma}^{\alpha}|_{SSD} = \rho^{\alpha}_{m_{SSD}} b v^{\alpha} \tag{2.20}$$

where $\rho^{\alpha}_{m_{SSD}}$ is the mobile part of the density of the dislocations within SSD, b is

the magnitude of Burger vector and v^α is the dislocation velocity on α slip system. The dislocation velocity v^α on α slip system is given in equation 2.22.

The shearing rate in α slip system due to the free glide of the nucleated dislocations is expressed as,

$$\dot{\gamma}^\alpha|_{nucl} = \rho^\alpha_{m_{nucl}} b v^\alpha \tag{2.21}$$

where $\rho^\alpha_{m_{nucl}}$ is the mobile part of the nucleated dislocations, b is the burger vector and v^α is the velocity of the dislocations. The resolved shear stress for nucleation of dislocation is generally much higher than the critical resolved shear stress(CRSS) required for a preexisting dislocation to glide. Hence, the nucleated dislocations, immediately after nucleation, experience a large resolved shear stress. Due to this large resolved shear stress, the initial velocity of dislocation is close to the shear-wave speed of the material. As the dislocation moves away from the high stress gradient region the propagation velocity also reduces significantly. Consequently, the velocity of dislocations can be expressed in an exponential form with a strong dependence on the resolved shear stress, as

$$v^\alpha = \lambda_1 v_\infty \left[\frac{\exp\left(-\frac{Q_{act}}{k_B \theta}\right)}{1 + \lambda_2 \exp\left(-\frac{\langle \tau^\alpha - \tau_{pass} \rangle}{\tau_{cut}}\right)} \right] sgn(\tau^\alpha) \tag{2.22}$$

Here, v_∞ is the upper bound of the dislocation velocity which is the shear-wave speed of the material and is expressed as $v_\infty = \sqrt{G/\rho}$. λ_1 *and* λ_2 are material

constants. G and ρ are shear modulus and mass density of the material respectively. τ_α is the resolved shear stress on α slip system. $\langle\bullet\rangle$ is the Maculay bracket and $sgn(\bullet)$ is the sign-function. Q_{act} is the activation energy required for a dislocation to overcome the local barrier without the aid of any applied shear stress, k_B is the Stephen-Boltzmann constant, θ is the absolute temperature in Kelvin. τ_{pass} and τ_{cut} are passing stress and cutting stress respectively. The passing stress τ^α_{pass} represents resistance for a mobile dislocation to slip due to the presence of other dislocations in the same slip plane and the cutting stress τ^α_{cut} represents the resistance for mobile dislocation to slip due to the presence of other dislocations perpendicular to the slip plane. They are expressed as,

$$\begin{aligned} \tau^\alpha_{pass} &= c_1 G b \sqrt{\rho^\alpha_P + \rho^\alpha_{m_{SSD}} + \rho^\alpha_{m_{nucl}}} \\ \tau^\alpha_{cut} &= \frac{Q\sqrt{\rho^\alpha_F}}{c_2 b^2} \end{aligned} \tag{2.23}$$

where c_1 and c_2 are material constants. G is the shear modulus and Q is the activation energy.

In the continuum region the plastic activity is considered to be dominated by the Statistically Stored Dislocations(SSDs) with a localized contribution of Geometrically Necessary Dislocations(GNDs) near the crack tip. The rate of evolution of SSD density has four major components in it. The SSDs due to lock formation($\dot{\rho}^{\alpha+}_{SSD_{lf}}$), dipole

formation $\dot{\rho}^{\alpha+}_{SSD_{df}}$, athermal annihilation $\dot{\rho}^{\alpha-}_{SSD_{aa}}$ and thermal annihilation $\dot{\rho}^{\alpha-}_{SSD_{ta}}$. i.e,

$$\dot{\rho}^{\alpha}_{SSD} = \dot{\rho}^{\alpha+}_{SSD_{lf}} + \dot{\rho}^{\alpha+}_{SSD_{df}} + \dot{\rho}^{\alpha-}_{SSD_{aa}} + \dot{\rho}^{\alpha-}_{SSD_{ta}} \tag{2.24}$$

Superscripts $+/-$ represents whether the contributing term is multiplication or annihilation in nature respectively. Th expression for the time rate of these four dislocation densities are given as [32, 34, 35],

$$\begin{aligned}
\dot{\rho}^{\alpha+}_{SSD_{lf}} &= \frac{c_3}{b}\sqrt{\rho^{\alpha}_{F}}\dot{\gamma}^{\alpha}_{SSD} \\
\dot{\rho}^{\alpha+}_{SSD_{df}} &= \frac{c_4}{b}\frac{\sqrt{3}Gb}{16\pi(1-\nu)}\left(|\tau^{\alpha}| - \tau^{\alpha}_{pass}\right)^{-1}\rho^{\alpha}_{m_{SSD}}\dot{\gamma}^{\alpha}_{SSD} \\
\dot{\rho}^{\alpha-}_{SSD_{aa}} &= -c_5\rho^{\alpha}_{SSD}\dot{\gamma}^{\alpha}_{SSD} \\
\dot{\rho}^{\alpha-}_{SSD_{ta}} &= -c_6\frac{D_0 b^3}{k_B\theta}\exp\left(\frac{-Q_{bulk}}{k_B\theta}\right)(\rho^{\alpha}_{SSD})^2|\tau^{\alpha}|\left(\frac{\dot{\gamma}^{\alpha}_{SSD}}{\dot{\gamma}_{ref}}\right)^{c_7}
\end{aligned} \tag{2.25}$$

Now, it is needed to compute the density of the mobile dislocation. Because it's the mobile dislocations ρ^{α}_{m} that contribute to the plastic strain (see eqn. 2.20). To compute the mobile dislocation density, the density of SSDs are projected as forest and parallel dislocation with interaction strength coefficients $\chi^{\alpha\beta}$ between different slip systems [41, 32],

$$\rho_F^\alpha = \sum_{\beta=1}^{N} \chi^{\alpha\beta} \left[\rho_{SSD}^\beta |\cos\left(\mathbf{n}^\alpha, \mathbf{t}^\beta\right)| \right]$$
$$\rho_P^\alpha = \sum_{\beta=1}^{N} \chi^{\alpha\beta} \left[\rho_{SSD}^\beta |\sin\left(\mathbf{n}^\alpha, \mathbf{t}^\beta\right)| \right] \tag{2.26}$$

The projected density of forest dislocation (ρ_F^α) and parallel dislocation (ρ_P^α) is used to compute the mobile dislocation density. The expression can be given as,

$$\rho_{m_{SSD}}^\alpha = \frac{2k_B\theta\sqrt{\rho_F^\alpha \rho_P^\alpha}}{c_1 c_2 G b^3} \tag{2.27}$$

Another major contribution to the mobile dislocation density is Geometrically Necessary Dislocation or GNDs. GNDs are necessary wherever there is a stress gradient. They preserve the lattice continuity. The conventional way to quantify the GND density is the relation proposed in [42, 43]. In the present work, the region of high stress gradient is the region near the crack tip. Since the crack and substantial region around it is modeled using Molecular Dynamics with an atomistic resolution, hence the GNDs necessary to maintain the lattice continuity in that region automatically gets nucleated from the crack tip. Hence all the dislocations that nucleate from the crack tip can be considered as GND in nature. This assumption is further justified due to the fact that the region near the crack tip is a dislocation free zone with occasional periodic nucleation from the crack tip [44]. Hence, the rate of GND density can be considered same as the rate at which the dislocations get nucleated from the crack

tip in the atomistic region (Ω_A) and enters the continuum region (Ω_C) through the interface (Ω_I) and subsequently propagates through the material. The propagation of these dislocations in the continuum is modeled using the advection equation as,

$$\dot{\rho}^{\alpha}_{nucl} = -\nabla.(\rho^{\alpha}_{nucl}\mathbf{v}^{\alpha}) + \rho_s \tag{2.28}$$

Here, ∇ is the gradient operator, $\mathbf{v}^{\alpha}$ is the velocity vector in α slip system (equation 2.22). The last term in the above equation i.e, ρ_s, is due to the generation of new dislocation density due to the influx of dislocations from the atomistic region Ω_A to the continuum Ω_C through the interface Ω_I. A detailed procedure on the characterization, quantification and subsequent conversion of the dislocations from discrete to the density form in the interface region is discussed in chapter 3.

It should also be noted that the GND density is not decomposed into the forest and parallel densities unlike in [32, 35], rather it contributes directly to the plastic shear rate (eqn. 2.21). The reason behind this is, the source of GND density in the present model is the nucleation of new dislocations at the crack tip. This nucleated dislocations subsequently propagate through a dislocation free zone before interacting with other dislocations. Hence it's more appropriate to consider these GNDs as mobile in nature. i.e,

$$\rho^{\alpha}_{m_{nucl}} = \rho^{\alpha}_{nucl} \tag{2.29}$$

2.3.0.1 An Unified Expression for the Dislocation Velocity

As already mentioned, the concurrent model contains two types of dislocations based on the neighboring dislocation structure it is located in. The preexisting dislocations have mainly formed during the forming process and subsequent strengthening process. These dislocations are mainly part of dislocation cell structures. The velocity of these dislocations is mainly determined by the density of the forest and parallel dislocations[33] and the stress required to get pass those barriers. Hence the critical resolved shear stress(CRSS) is high $O(10^2 MPa)$ and the resulting velocity beyond the CRSS is low. Contrary to this, the dislocations nucleating from the crack-tip experience a very high resolved shear stress in the part of the crystal which is free from the preexisting dislocations. Due to this reason the nucleated dislocations experience very little resistance during propagation. The only resistance the nucleated dislocations experience is due to the lattice friction $O(10MPa)$. Hence, the speed of dislocations after nucleation can reach the shear-wave speed of the material. The equation 2.22 unifies these two velocity profiles with two material parameters viz. λ_1 *and* λ_2. λ_1 controls the maximum velocity of a dislocation. Though the theoretical sound wave speed in nickel is calculated to be $\sqrt{(}G/\rho) = 3746m/sec$ where $G = 125GPa$ *and* $\rho = 8908Kg/m^3$, the maximum velocity of dislocation has been observed to be $O(2000m/s)$[45]. To calibrate the value of λ_1 *and* λ_2, MD simulation is performed to obtain the velocity of a single dislocation under different driving shear stress. The atomistic domain has a physical dimension of $50nm \times 5nm \times 5nm$

which contains around 100thousand nickel atom with FCC lattice structure and lattice constant 3.52Å. The orientation of the crystal with respect to the global axis is $x \rightarrow [11\bar{2}]$, $y \rightarrow [111]$ and $z \rightarrow [1\bar{1}0]$. NPT ensemble is used for MD simulation. Initial dislocation is created by applying a deformation gradient corresponding to the simple shear. Once both the partial dislocations are nucleated, the system is dynamically equilibrated. After equilibration, the dislocation is driven by applying a constant amount of shear stress τ_{app} on the y-plane. The time-averaged velocity of the dislocation is noted under different applied shear stress.

Figure 2.2(a) shows the velocity of the dislocation for different applied shear stress. The critical resolved shear stress(CRSS) for the dislocation glide inside a perfect single crystal is found to be around 10MPa. The dislocation velocity reaches a stable magnitude of $1900m/s$ within an applied shear stress of 200MPa. A similar finding has previously been reported in [46]. The velocity data obtained from the MD simulation is used to obtain the parameters λ_1 *and* λ_2 of equation 2.22. The value of λ_1 *and* λ_2 is found to be 1.3 and 51.2 respectively. While exploring the parameter values it has been assumed that $\tau_{pass} = \tau_{cut} = CRSS$ and $Q_{act} \simeq 1k_B\theta$. Figure 2.2(b) shows the velocity profile of the dislocation under different values of CRSS. A low CRSS value O(10MPa) maybe considered as the glide through a perfect crystal and larger the CRSS values O(100MPa) may be related to the more dense dislocation cell structure.

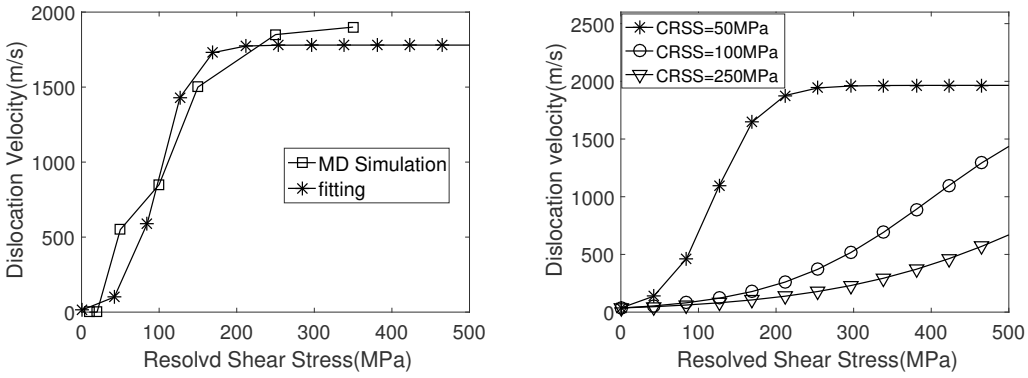

(a) (b)

Figure 2.2: Dislocation velocity as function of resolved shear stress: (a) velocity data for a free gliding dislocation inside a nickel perfect crystal is fitted with the functional form of eq. 2.22, (b) velocity profile of a dislocation gliding through preexisting dislocations represented by higher CRSS value.

2.4 Material Model for the Atomistic Region: Time accelerated Molecular Dynamics

The atomistic region Ω_A is modeled using time accelerated Molecular Dynamics(MD). The Strain Boost Hyperdynamics[37, 47] is used for time acceleration. The Strain Boost Hyperdynamics has been implemented in LAMMPS [47] and also been incorporated into the concurrent framework to study the brittle fracture in Ni single crystal at lower strain rate [25]. In Molecular Dynamics the atomic motion is governed by the Newton's equation of motion,

$$m_p \ddot{\mathbf{u}}_\mathbf{p} = \mathbf{f}_\mathbf{p} \tag{2.30}$$

where m_p and $\ddot{\mathbf{u}}_\mathbf{p}$ are the mass and acceleration of atom p subjected to the force $\mathbf{f}_\mathbf{p}$. The atomistic domian Ω_A is divided in four sub-domain based on the types of forces that the atoms in that region experience. These are,

1. In the subdomain Ω_A^{In}, the motion of atoms is governed by interactions with neighboring atoms only. This inter-atomic interaction is approximated through an Embedded Atom Model(EAM) based potential[5]. The EAM potentials are many body potentials and particularly appropriate to model metallic materials where electrons are spread more like a cloud contrary to the covalently bonded structure. The force experienced by atoms due to the inter-atomic potential (Φ), is written as:

$$\boldsymbol{f}_p^{In} = -\boldsymbol{\nabla}\Phi \tag{2.31}$$

2. The atoms in subdomain Ω_A^I belongs to the interface region. In addition to inter-atomic interactions, these atoms also experience forces due to their interaction with the corresponding coupled Finite Element node. Damping is also applied to this region for maintaining temperature and elastic waves are suppressed by using a Langevin thermostat [48]. The force experienced by these atoms is

computed as:

$$\boldsymbol{f}_p^I = -\boldsymbol{\nabla}\Phi + w_p\boldsymbol{\lambda}_\beta + \boldsymbol{f}^p_{\text{A-ext}} - \gamma m_p\dot{\boldsymbol{r}}_p + \sqrt{2\gamma K_B\theta m_p}R(t) \tag{2.32}$$

where γ is the damping coefficient, k_B is the Stefan-Boltzmann constant, θ is the target temperature and R(t) is a delta-correlated stationary Gaussian process with zero-mean value.

3. Subdomain Ω_A^S of atoms belonging to the surface region. Ghost force corrections are made over atoms of this region to mitigate the free surface effect [2, 1, 25]. The corresponding forces are:

$$\boldsymbol{f}_p^S = -\boldsymbol{\nabla}\Phi - \boldsymbol{f}_p^G - \gamma m_p\dot{\boldsymbol{r}}_p + \sqrt{2\gamma K_B\theta m_p}R(t) \tag{2.33}$$

where $\boldsymbol{f}_p^G$ is the mitigating force for the free surface effect.

4. The atoms in the subdomain Ω_A^B are the most critical one. These atoms forms the crack tip and hence contribute in the nucleation of dislocations. To accelerate the nucleation process in this region the atoms are modeled with hyperdynamics accelerated MD by applying a suitable boost potential [49, 37]. These atoms experience an additional force due to the applied boost potential given as,

$$\boldsymbol{f}_p^B = -\boldsymbol{\nabla}\Phi - \boldsymbol{\nabla}\big\{\Delta V(r)\big\} \tag{2.34}$$

where $\Delta V(r)$ is the boost potential. Figure 2.3 shows the details of all the different subdomains of the atomistic region Ω_A.

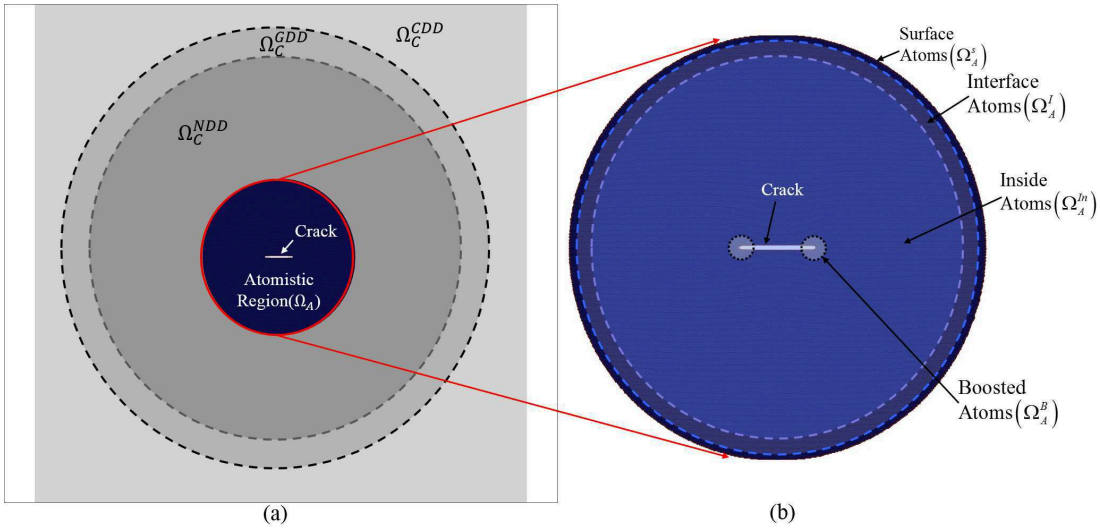

Figure 2.3: Details division of the atomistic domain into multiple sub-regions. Showing only the atomistic region.

Construction of appropriate boost potential $\Delta V(r)$ is very crucial requirement to achieve optimal time acceleration without introducing any spurious deformation mechanism. A detailed construction procedure of appropriate boost potential is discussed in chapter 4.

Chapter 3

Framework to Transfer and Propagate the Dislocations from the Atomistic to the Continuum

In the concurrent model, at the onset of plasticity, dislocations are nucleated from the crack tip. Due to the large negative stress gradient near the crack tip, the nucleated dislocations propagate through the atomistic region and approach towards the interface. These dislocations are needed to be transferred from the atomistic to the continuum domain in a representative way. By 'representative' means, the total dislocation length and the sharp spatial gradient of dislocation density of the dislocation core need to be maintained. Also, an appropriate method should be incorporated such that it is valid for any kind of dislocations viz, straight dislocation

or a curved one. Once transferred, the dislocations need to keep propagating based on the local resolved shear stress corresponding to that slip system at a velocity given in equation 2.22. The dislocation keeps propagating until it reaches a region where the propagation velocity is reduced drastically due to the interaction with pre-existing dislocations. This chapter discusses the framework that is used to transfer the dislocations from the atomistic to the continuum at the interface and also the modeling of the propagation of dislocations in the continuum in the density form.

3.1 The Framework to Transfer the Dislocations from Atomistic to Continuum at the Interface

For an appropriate transfer of dislocations, at the interface, the dislocations are characterized and quantified using Dislocation Extraction Algorithm(DXA) [50]. For a given atomic configuration, DXA first separates all the atoms that are not in the perfect lattice from those which are in perfect lattice position. For this purpose, the atomic structure identification algorithm such as common neighbor analysis (CNA) [7] is used. Once the atoms that contain the defect structure (e.g, dislocation core) are identified, the 'Burger circuit method' is used to trace down the dislocation and represent it as a collection of points also called dislocation bids. Figure 3.1 shows the

steps involved in extracting the dislocations from a given atomic configuration using DXA. Distance between each consecutive pair of bids is considered as a dislocation line segment $\boldsymbol{dl}$. Figure 3.1(d) shows an example of such representation of dislocation with dislocation bids and line segments.

The length of each line segment is the Euclidean distance between the bids it consists of. To represent the dislocations from it's discrete representation to the field form, it's needed to convert the dislocation line lengths ($|\boldsymbol{dl}|$) into a line density form. Following Gaussian distribution function is used for this purpose,

$$w(\boldsymbol{x}, \boldsymbol{X}) = \frac{1}{(\sigma\sqrt{2\pi})^3} e^{-\frac{(||\boldsymbol{x}-\boldsymbol{X}||_3)^2}{2\sigma^2}} \tag{3.1}$$

where $\boldsymbol{X}$ is the position vector of the dislocation segment in the discrete form and $||\bullet||_3$ is the Euclidean distance in 3-dimension. The position vector $\boldsymbol{X}$ of the dislocation segment $\boldsymbol{dl_i}$ is approximated as the midpoint of the pair of bids that construct the length segment. Here, σ (without any subscript) is the standard deviation of the distribution which corresponds to the spread of the dislocation density. σ can be estimated by analyzing the stress field around a dislocation created by the dislocation itself. The stress field due to the presence of a dislocation can be obtained by using Volterra construction within Linear Elastic Solid Mechanics [51]. Two types of dislocations are considered here, straight edge dislocation and straight screw dislocation. Any other dislocation of mixed character can always be decomposed into an edge component and screw component and the stress field can be obtained by superpos-

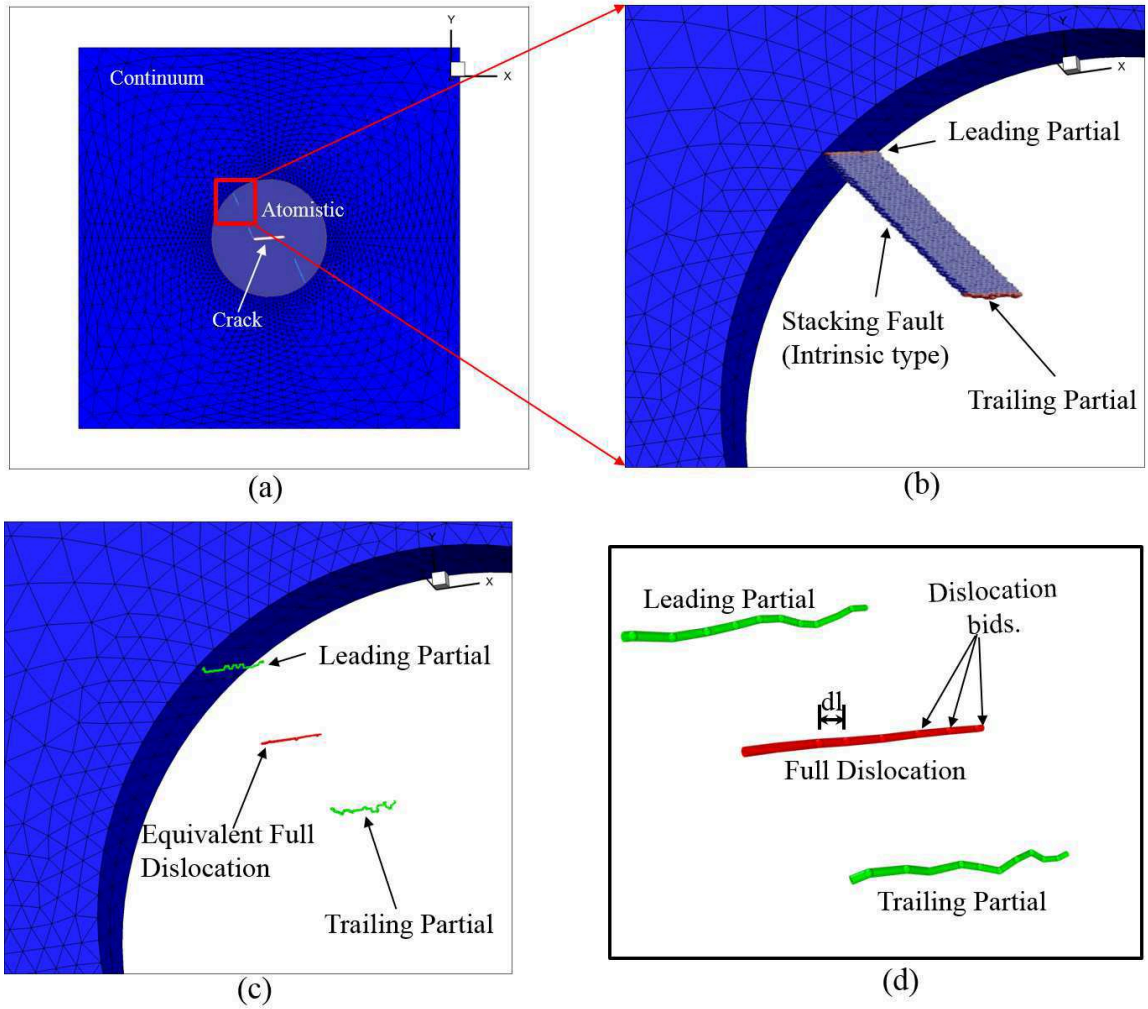

Figure 3.1: Steps for extraction of the dislocations from a given atomic configuration. (a) The concurrent model with dislocations in the atomistic region. (b) The dislocations and the stacking fault are identified by using Common Neighbor Analysis(CNA). The red atoms represent the core of the leading and trailing partial dislocations. The blue atoms represent the stacking fault between the two partials. (c) Dislocations are converted from atomic representation to the discrete form. (d) The extracted dislocations are smoothed out to mitigate the noise due to thermal vibration.

ing the stress field for the individual component. Figure 3.2 shows the contour plot of the stress field around a straight dislocation. To obtain a material independent estimation of the stress field, the magnitude of the normal stresses are normalized

to the Young's modulus and shear stress are normalized to the shear modulus of the material. Spatial dimensions are also normalized to the magnitude of burger vector $|\vec{b}|$. Figure 3.2(a), 3.2(b) and 3.2(c) shows the contour plot of σ_{xx}, σ_{yy} and σ_{xy} of a straight edge dislocation respectively. It can be seen that the normalized stress reduces to less than 5% beyond the spacial distance of $5|\vec{b}|$ from the dislocation core. Similarly figure 3.2(d) and 3.2(e) shows the stress field of σ_{xz} and σ_{yz} around a screw dislocation respectively. It can be seen that for screw dislocation the normalized shear stresses reduce to below 5% beyond a spatial distance of $3|\vec{b}|$ from the dislocation core. For the Gaussian distribution, 95% of the density lies within the 2σ distance from the mean. Hence, the criterion for σ is taken to be the spatial distance beyond which the normalized stress reduces to 5% or less. Hence the value of σ is taken to be $2\sigma = 5|\vec{b}|$, where $|\vec{b}|$ is the magnitude of the Burger vector of the material. For nickel with $|\vec{b}| \approx 2.49$Å, the numerical value of σ becomes ≈ 6.25Å. As already mentioned, for mixed dislocation, the burger vector can always be projected into an edge component and a screw component. Since the non-zero stress components developed by an edge dislocation i.e, σ_{xx}, σ_{yy} *and* σ_{xy} and a screw dislocation i.e, σ_{xz} *and* σ_{yz} are mutually exclusive, hence for mixed dislocation also the normalized stress will reduce below 5% beyond a spatial distance of $5|\vec{b}|$ from the dislocation core.

With the distribution function given in equation 3.1, the dislocation density at any location with position vector ($\boldsymbol{x}$) becomes,

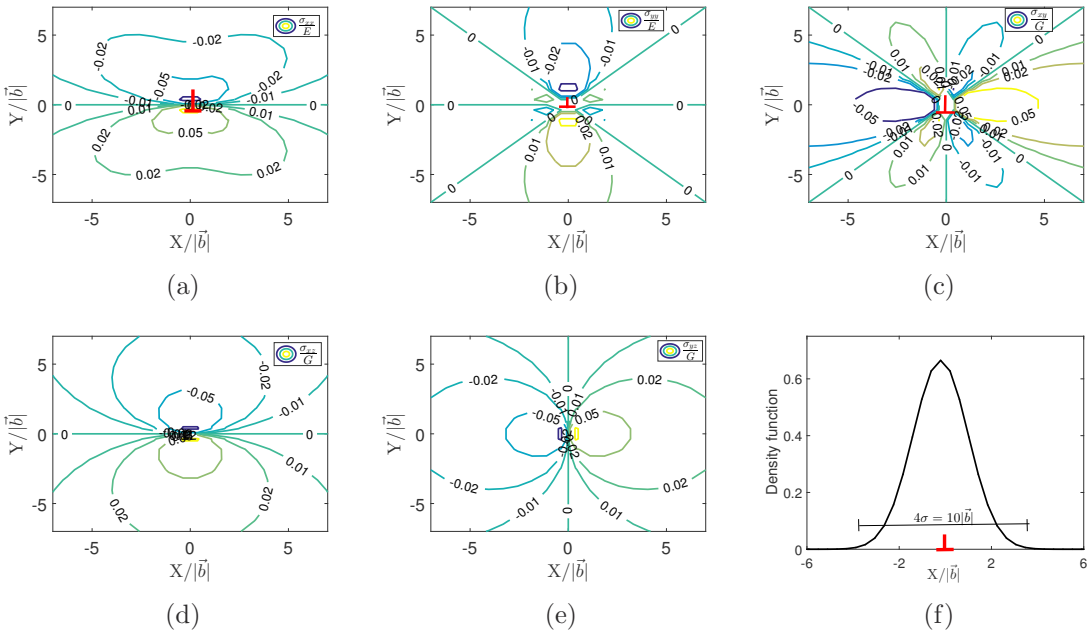

Figure 3.2: Contour plot of the stress due to the presence of a dislocation. Stress due to an edge dislocation (a)σ_{xx}, (b)σ_{yy} and (c)σ_{xy}. The stress due to screw dislocation (d)σ_{xz} and (e)σ_{yz}. (f)The Gaussian distribution used to represent the stretch of the dislocation core.

$$\rho_{nucl}(\boldsymbol{x}) = w(\boldsymbol{x}, \boldsymbol{X})|\boldsymbol{dl}| \tag{3.2}$$

where, $|\boldsymbol{dl}|$ is the length of the dislocation segment and $\rho_{nucl}(\boldsymbol{x})$ is the dislocation density at $\boldsymbol{x}$. Note that, since $\int_\Omega w(\boldsymbol{x}, \boldsymbol{X}) = 1$ hence $\int_\Omega \rho_{nucl}(\boldsymbol{x}) = |\boldsymbol{dl}|$. This implies that the total dislocation length is preserved while converting the representation of dislocation from discrete to density form. In the coupled concurrent model the dislocations are identified at the Dislocation Detection zone(Ω_{DD}). Figure 3.3 shows one of such dislocation transfer at the interface from discrete representation at the atomistic domain to the density representation in the continuum.

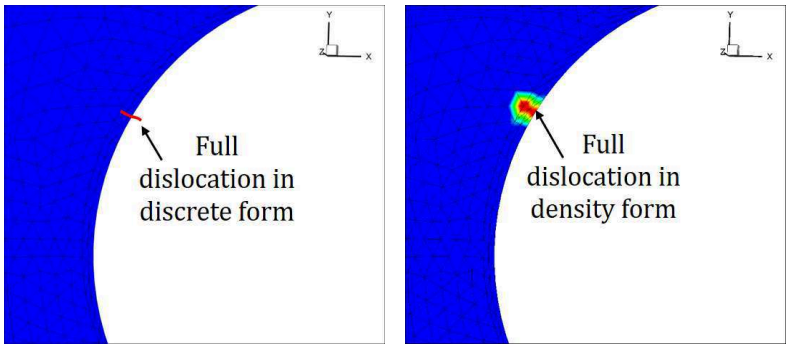

(a) (b)

Figure 3.3: A dislocation is transformed from it (a)discrete representation to the (b)density form.

3.2 Modeling the Propagation of Dislocation in the Density form in the Continuum

At the continuum region, propagation of the dislocations in the density form can be modeled using the transport equation of a conserved quantity. The transport equation without any dispersion is also know as advection equation. For a conserved and scalar quantity ψ , the advection equation is written as,

$$\frac{\partial \psi}{\partial t} + \boldsymbol{\nabla}.(\psi \boldsymbol{v}) = \psi_s \tag{3.3}$$

where, $\boldsymbol{\nabla}$ is the gradient operator, $\boldsymbol{u}$ is the velocity field of the advected scalar quantity ψ and ψ_s is the source term. The advected scalar quantity ψ in the present

scenario is the dislocation density. ψ_s represents the dislocation density generation from both due to the incoming dislocations from the atomistic region and also due to the expansion of the dislocation loop. In the present study, due to the the specific orientation of the crystal, the dislocations are straight-dislocation, hence the source term ψ_s will mainly represent the density generation due to the incoming dislocation from the atomistic region. The equation 3.3 can further be expanded as,

$$\frac{\partial \psi}{\partial t} + \boldsymbol{v}.\boldsymbol{\nabla}\psi + \psi\boldsymbol{\nabla}.\boldsymbol{v} = \psi_s \tag{3.4}$$

In equation 3.4 the second term contains the spatial gradient of dislocation density ψ and the third term contains the divergence of the dislocation velocity $\boldsymbol{v}$. The spatial length scale over which dislocation density (ψ) varies is $\sim |\vec{b}| \sim 1.0e^{-10}m$, where $|\vec{b}|$ is the magnitude of the burger vector of that material. On the other hand the spatial dimension over which dislocation velocity ($\boldsymbol{v}$) varies is $\sim\ 100e^{-9}m$. Hence, the spatial gradient of ψ is at-least three order of magnitude larger than the spatial gradient of $\boldsymbol{v}$. For this reason the third term in the left hand side of equation 3.4 can be ignored. Then the simplified form of the above equation becomes,

$$\frac{\partial \psi}{\partial t} + \boldsymbol{v}.\boldsymbol{\nabla}\psi = \psi_s \tag{3.5}$$

Equation 3.5 is needed to be numerically solved over the continuum domain for the propagation of the dislocation in density form. It has already been seen from section

3.1 that for an individual dislocation the core is spread over a spatial dimension of not more than $10|\vec{b}|$ which is $\approx$ 25Å for nickel. For this reason, to maintain the characteristic sharp gradient of dislocation density in a very localized zone, the discretization size needed to be $O(5\text{Å})$. An element-based discretization would be computationally prohibitive. Hence, a mesh-free particle-based method is the most suitable choice for the numerical solution of equation 3.5 over the continuum domain. In the present study, Smooth Particle Hydrodynamics(SPH) is used as a discretization scheme along with point collocation to solve the equation 3.5 over the continuum domain. The Smooth Particle Hydrodynamics(SPH) is discussed next.

3.3 Smooth Particle Hydrodynamics(SPH)

Smooth Particle Hydrodynmaics(SPH) was first proposed by [52]. In this method, the computational domain is discretized by the distribution of a set of points throughout the domain, called particles.

3.3.1 Kernel Approximation and the Integral Representation of the Interpolation Function

According to kernel approximation the value of a function $f(x)$ at any point s can be approximated in an integral form as,

$$f(x) \simeq \int_{\Omega} f(s)\delta(x-s)ds \tag{3.6}$$

where, $\delta(x-s)$ is the Dirac delta function, which is defined as,

$$\delta(x-s) = \begin{cases} \infty & \text{for } s = x \\ 0 & \text{otherwise} \end{cases} \tag{3.7}$$

$$\int_{-\infty}^{\infty} \delta(s)ds = 1 \tag{3.8}$$

Since $\delta(x-s)$ is not a smooth function, the Dirac delta function in equation 3.7 is replaced by a smoothing function $W(x-s,h)$. Then equation 3.6 becomes,

$$f(x) \simeq \int_{\Omega} f(s)W(x-s,h)ds \tag{3.9}$$

where h is the smoothing length and $W(x-s,h)$ is called 'smoothing kernel function' or just 'kernel function'. The 'kernel function' $W(x-s,h)$ is chosen to be an even function and also need to satisfy following requirements.

First, the normalization condition. i.e,

$$\int_{-\infty}^{\infty} W(x-s,h)ds = 1 \tag{3.10}$$

This condition is similar to equation 3.8 of Dirac delta function.

Second, is the 'Delta function property',

$$\lim_{h\to 0} W(x-s,h) = \delta(x-s) \tag{3.11}$$

i.e as the smoothing length(h) approaches to zero, the kernel function reproduces the Dirac delta function.

Third is the requirement of compact support. The kernel function are required to be non-zero positive in a small domain while zero everywhere else. i.e,

$$W(x-s,h) = 0 \quad \text{when} \quad |x-s| > \kappa h \tag{3.12}$$

where κ is a measure of the extent of the support domain within which the kernel function $W(x-s)$ is non-zero positive. The importance of this third requirement will be clear when the gradient of a function $f(x)$ using kernel approximation is derived next.

To derive the gradient of a generic function $f(x)$, kernel approximation of equation 3.9 can be used. Then the gradient of $f(x)$ becomes,

$$\Delta f(x) = \int_{\Omega} \Delta f(x) W(x-s,h) ds \tag{3.13}$$

By applying the integration by parts equation 3.13 becomes,

$$\Delta f(x) = \int_{\Omega} \Delta[f(s)W(x-s,h)]ds - \int_{\Omega} f(s)\Delta W(x-s,h)ds \tag{3.14}$$

Now, applying divergence theorem on the first term, the equation 3.14 becomes,

$$\Delta f(x) = \int_{\partial\Omega} f(s)W(x-s,h)nd\partial s - \int_{\Omega} f(s)\Delta W(x-s,h)ds \tag{3.15}$$

where the integral in the first term is over the boundary($\partial\Omega$) of the compact support region of the kernel function and n is the unit normal to the boundary surface $\partial\Omega$. Since the kernel function $W(x-s,h)$ is defined to have a compact support hence, $W(x-s,h)$ is zero everywhere on the boundary $\partial\Omega$. This renders the first integral of equation 3.15 to be zero. Then the equation 3.15 becomes,

$$\Delta f(x) = -\int_{\Omega} f(s)\Delta W(x-s,h)ds \tag{3.16}$$

3.3.2 Particle Approximation

In the SPH method the entire domain is represented by the distribution of finite number of particles. With this particle approximation of the domain, the continuous integrals involved in equation 3.9 and 3.16 can be converted into the discretized summation over all the particles in the domain.Then equation 3.16 can be written as,

$$f(x) \simeq \sum_{i=1}^{N_I} f(x_i) W(x - x_i, h) \Delta\Omega_i \tag{3.17}$$

Similarly the gradient of the function $f(x)$ (equ. 3.15) becomes,

$$\Delta f(x) \simeq -\sum_{i=1}^{N_I} f(x_i) \Delta W(x - x_i, h) \Delta\Omega_i \tag{3.18}$$

where N_I is the number of particles belong within the support domain of the kernel function and $\Delta\Omega_i$ is the weight associated to the i^{th} particle. The term $W(x_i - x, h)\Delta\Omega_i$ is also called SPH shape function corresponding to particle I.

Figure 3.4(a) and 3.4(b) show the kernel function in $1D$ for two particles, one well within the domain and the other particle close to the domain boundary respectively. It can be seen in figure 3.4(b) that the kernel function is incomplete and it does not have the compact support. Due to this lack of compact support for particles close to the boundary, the normalization requirement of the kernel function (equation 3.10) breaks down.

Figure 3.5(a) and 3.5(b) show the reproducing capability of the SPH shape function for a linear function and it's derivative using equation 3.17 and 3.18 respectively. It can be seen that the SPH shape function is good enough to reproduce the function and it's gradient for the particles away from the boundary, but it fails to reproduce the function and it's gradient for particles close to the boundary. This is mainly due to the loss of compact support for those particles close to the boundary. A similar

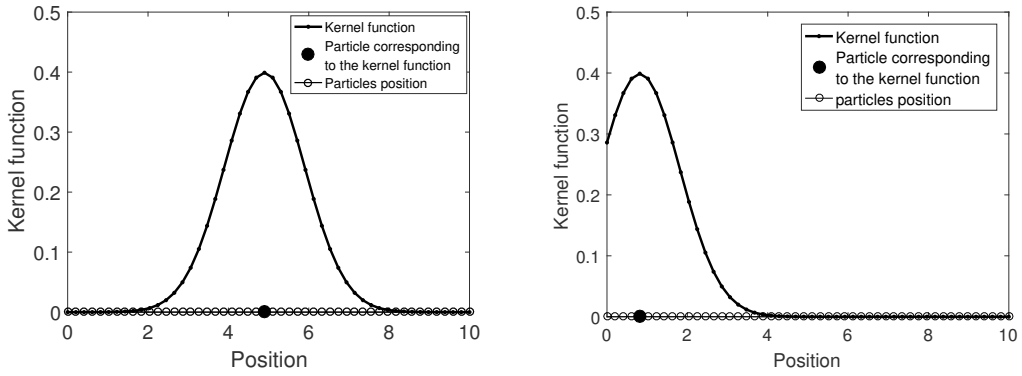

(a) (b)

Figure 3.4: KernelFunction associated with a particle located at (a)far from the boundary and (b)close to the boundary.

trend is observed for a nonlinear sine-function and it's gradient as well in figure 3.5(c) and 3.5(d) respectively.

3.3.3 Correction of SPH for finite domain using RKPM method

As described in the previous section, SPH shape function fails to reproduce the function and and it gradients for particles close to the domain boundary. This is due to the lack of compact support of kernel function near the domain boundary. To alleviate this discrepancy Reproducing Kernel Particle Method(RKPM) has been developed [53, 54, 55, 56]. The rational behind the Reproducing Kernel Particle Method(RKPM) is to augment the kernel approximation by pre-multiplying the kernel function with a suitable choice of correction function. Based on the RKPM, the modified form of

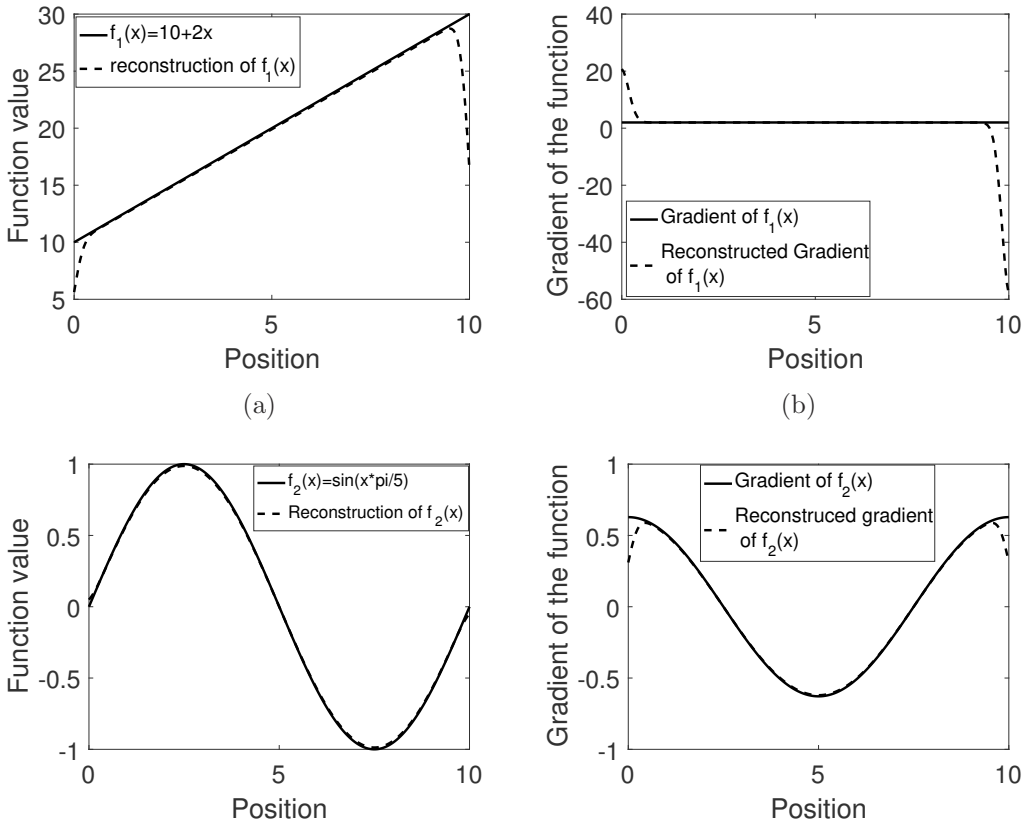

Figure 3.5: Reproducing capability of SPH shape function for (a) a linear function, (s) slope of the linear function, (c) sine function and (d) slope of the sine function.

interpolation of a function $f(x)$ (equation 3.9) becomes,

$$f(x) \simeq \int_{\Omega} f(x)\overline{W}(x-s,h)d\Omega \tag{3.19}$$

where, $\overline{W}(x-s,h)$ is the modified kernel function and is given as,

$$\overline{W}(x-s,h) = C(x,s)W(x-s,h) \tag{3.20}$$

where, $C(x,s)$ is the correction function. A polynomial function of suitable order is used as the correction function [55, 56]. The order of the polynomial is determined based on the highest order of derivative present in the Governing Differential Equation(GDE) that need to be reproduced. In this work, SPH is used to propagate the dislocation density in the continuum domain. The highest derivative corresponding to that GDE (3.4) is one. Hence, a linear polynomial is used as a correction function. i,e

$$C(x,s) = c_0(x) + c_1(x)(x-s) + \dots \tag{3.21}$$

The corrected form of SPH kernel function (3.9) or RKPM kernel function becomes,

$$\overline{W}(x-s,h) = (c_0(x) + c_1(x)(x-s))W(x-s,h) \tag{3.22}$$

And modified form of equation 3.9 after RKPM becomes,

$$f^a(x) =\simeq \int_\Omega f(s)\overline{W}(x-s,h)d\Omega \tag{3.23}$$

The coefficients, $c_0(x)$ and $c_1(x)$ in the correction function are unknown and dependent on the spatial co-ordinate. These coefficients are determined by satisfying the reproducing condition of the function. The spatial derivatives of these coefficients are also determined if the gradients of the function are also needed to be reproduced.

The process of determining these coefficients and their derivative is discussed next.

For the sake of simplicity, the present derivation is kept limited to one dimension only.

$$f(s) = f(x) + (s-x)f'(x) + \frac{(s-x)^2}{2!}f''(x) + ... \tag{3.24}$$

where, prime denotes the differentiation with respect to x. Substituting equation 3.24 into equation 3.22 gives,

$$\begin{aligned} f^a(x) = f(x)\int_\Omega \overline{W}(x-s,h)ds + f'(x)\int_\Omega \frac{(s-x)}{1!}\overline{W}(x-s,h)ds \\ + f''(x)\int_\Omega \frac{(s-x)^2}{2!}\overline{W}(x-s,h)ds + ... \end{aligned} \tag{3.25}$$

By denoting the moments of the modified kernel function as,

$$\overline{m}_k(x) = \int_\Omega (x-s)^k \overline{W}(x-s,h)ds \quad k = 0,1,2,... \tag{3.26}$$

equation 3.25 can be rewritten as,

$$f^a(x) = f(x)\overline{m}_0(x) - \frac{f'(x)}{1!}\overline{m}_1(x) + \frac{f''(x)}{2!}\overline{m}_2(x) + ... \tag{3.27}$$

With the objective to reproduce the function, the condition that needed to be en-

forced is $f^a(x) = f(x)$. Then, from equation 3.27 the reproducing condition becomes,

$$\begin{Bmatrix} \overline{m}_0(x) \\ \overline{m}_1(x) \\ \overline{m}_2(x) \\ . \\ . \end{Bmatrix} = \begin{Bmatrix} 1 \\ 0 \\ 0 \\ . \\ . \end{Bmatrix} \tag{3.28}$$

Equation 3.26 can be further expanded as,

$$\begin{aligned} \overline{m}_k(x) &= \int_\Omega (x-s)^k \overline{W}(x-s,h)ds \quad k = 0,1,2,... \\ &= \int_\Omega (x-s)^k \left[c_0(x) + (x-s)c_1(x) + \dots\right] W(x-s,h)ds \quad k = 0,1,2,... \\ &= c_0(x)m_k(x) + c_0(x)m_{k+1}(x) + c_0(x)m_{k+2}(x) + \dots \end{aligned} \tag{3.29}$$

where, $m_k(x)$ is the k'th moment of the SPH kernel function and is defined as,

$$m_k(x) = \int_\Omega (x-s)^k W(x-s)ds \tag{3.30}$$

After substituting equation 3.29 in equation 3.28, the reproducing condition becomes,

$$\begin{bmatrix} m_0(x) & m_1(x) & \cdots & m_N(x) \\ m_1(x) & m_2(x) & \cdots & m_{N+1}(x) \\ . & . & \cdots & . \\ m_N(x) & m_{N+1}(x) & \cdots & m_{2N}(x) \end{bmatrix} \begin{Bmatrix} c_0(x) \\ c_1(x) \\ . \\ c_N(x) \end{Bmatrix} = \begin{Bmatrix} 1 \\ 0 \\ . \\ 0 \end{Bmatrix} \tag{3.31}$$

In a symbolic form equation 3.31 can be rewritten as,

$$\mathbf{M}\boldsymbol{C} = \boldsymbol{b} \tag{3.32}$$

Then the vector of unknown correction coefficients $\boldsymbol{C}(\boldsymbol{x}) = \{c_0(x)\ c_1(x)\ c_2(x)\ \cdots\}'$ becomes,

$$\boldsymbol{C} = \mathbf{M}^{-1}\boldsymbol{b} \tag{3.33}$$

These unknown correction coefficients vector is solved for each particle.

3.3.3.1 Reproducing condition for first derivative

The modified form of the kernel approximated gradient of the function $f(x)$ i.e, equation 3.16 also need to be derived. Using the RKPM kernel approximation (equ. 3.22) into equation 3.16, the gradient becomes,

$$\nabla f(x) = -\int_\Omega f(s)\nabla\overline{W}(x-s,h)ds \tag{3.34}$$

$$= -\int_\Omega f(s)\nabla[C(x,s)W(x-s,h)]\,ds \tag{3.35}$$

$$= -\int_\Omega f(s)\left[\nabla C(x,s)W(x-s,h)ds + C(x,s)\nabla W(x-s,h)\right]ds \tag{3.36}$$

$$\tag{3.37}$$

Computation of the term $\nabla C(x,s)$ in equation 3.37 necessitates the determination of the spatial gradient of the correction coefficients, i.e, $c_0'(x), c_1'(x), c_2'(x), ...$ etc. The procedure to determine the spatial gradient of these coefficients is discussed next. For simplicity the derivation is kept limited withing one spatial dimension only.

We will start from equation 3.37 and use Taylor's expansion (eq. 3.24) to approximate the function $f(x)$. Then equation 3.37 becomes,

$$[f^a(x)]' = -\int_\Omega \left[f(x) + (s-x)f'(x) + \frac{(s-x)^2}{2!}f''(x) + \ldots\right]\nabla\overline{W}(x-s,h)ds \tag{3.38}$$

$$= -f(x)\int_\Omega \nabla\overline{W}(x-s,h)ds + f'(x)\int_\Omega \frac{(x-s)}{1!}\nabla\overline{W}(x-s,h)ds \tag{3.39}$$

$$- \quad f''(x)\int_\Omega \frac{(x-s)^2}{2!}\nabla\overline{W}(x-s,h)ds + \ldots \tag{3.40}$$

Now, define the moment of RKPM kernel function as,

$$\overline{m}'_k(x) = \int_\Omega (x-s)^k \nabla \overline{W}(x-s,h)ds \quad k = 0,1,2,\ldots \tag{3.41}$$

then equation 3.40 becomes,

$$[f^a(x)]' = -f(x)\overline{m}'_0 + \frac{f'(x)}{1!}\overline{m}'_1 - \frac{f''(x)}{2!}\overline{m}'_2 + \ldots \tag{3.42}$$

Then the reproducing condition for the gradient becomes,

$$\left\{ \begin{array}{c} \overline{m}'_0(x) \\ \overline{m}'_1(x) \\ \overline{m}'_2(x) \\ . \\ . \end{array} \right\} = \left\{ \begin{array}{c} 0 \\ 1 \\ 0 \\ . \\ . \end{array} \right\} \tag{3.43}$$

Equation 3.41 can further be expanded as,

$$
\begin{aligned}
\overline{m}'_k(x) &= \int_\Omega (x-s)^k \nabla \overline{W}(x-s,h) ds \quad k = 0,1,2,\ldots \\
&= \int_\Omega (x-s)^k \nabla \left[c_0(x) W(x-s,h) + c_1(x)(x-s) W(x-s,h) \right. \\
&+ \left. c_2(x)(x-s)^2 W(x-s,h) + \ldots \right] ds \quad k = 0,1,2,\ldots \\
&= \left[c'_0(x) m_k(x) + c'_1(x) m_{k+1}(x) + c'_2(x) m_{k+2}(x) + \ldots \right] \\
&\quad + \left[c_0(x) m'_k(x) + c_1(x) m'_{k+1}(x) + c_2(x) m'_{k+2}(x) + \ldots \right] \quad k = 0,1,2,\ldots
\end{aligned}
\tag{3.44}
$$

where $m_k(x)$ is the k'th moment of the SPH kernel function and already defined in equation 3.30 and $m'_k(x)$ is defined by,

$$
m'_k(x) = \int_\Omega \left[(x-s)^k W(x-s,h) \right]' ds \tag{3.45}
$$

After using equation 3.44 the expanded form of the reproducing condition for the gradient becomes,

$$\begin{bmatrix} m_0(x) & m_1(x) & \cdots & m_N(x) \\ m_1(x) & m_2(x) & \cdots & m_{N+1}(x) \\ . & . & \cdots & . \\ m_N(x) & m_{N+1}(x) & \cdots & m_{2N}(x) \end{bmatrix} \begin{Bmatrix} c_0'(x) \\ c_1'(x) \\ . \\ c_N'(x) \end{Bmatrix} + \begin{bmatrix} m_0'(x) & m_1'(x) & \cdots & m_N'(x) \\ m_1'(x) & m_2'(x) & \cdots & m_{N+1}'(x) \\ . & . & \cdots & . \\ m_N'(x) & m_{N+1}'(x) & \cdots & m_{2N}'(x) \end{bmatrix} \begin{Bmatrix} c_0(x) \\ c_1(x) \\ . \\ c_N(x) \end{Bmatrix} = \begin{Bmatrix} 0 \\ 1 \\ . \\ 0 \end{Bmatrix} \tag{3.46}$$

Equation 3.46 can be rewritten in symbolic form as,

$$\mathbf{M}\boldsymbol{C'} + \mathbf{M'}\boldsymbol{C} = \boldsymbol{b'} \tag{3.47}$$

Then the solution for the gradient of unknown correction coefficients i.e, $\boldsymbol{C'(x)} = \{c_0'(x)\ c_1'(x)\ c_2'(x)\ \dots\}$ becomes,

$$\boldsymbol{C'} = \mathbf{M}^{-1}\left[\boldsymbol{b'} - \mathbf{M'}\boldsymbol{C}\right] \tag{3.48}$$

To understand the improvement in the RKPM method in comparison to the SPH method, two different function is used to judge their reproducing capability. One linear $f_1(x) = 10{+}2{*}x$ and the other one nonlinear sinusoidal function $f_2(x) = sin\left(\frac{\pi x}{5}\right)$.

The domain is of length 10unit. The domain is discretized uniformly using 100 particles i.e, inter-particle distance is 0.1unit. A Gaussian function with smoothing length of 0.4unit is used as kernel function. The correction function(equ. 3.21) used for this example problem is a linear polynomial i,e $c(x) = c_0(x) + c_1(x)(x - s)$. This correction function has only two coefficients. This correction function can reproduce up-to the first derivative of the approximating function. Now, it is needed to solve equation 3.33 to get the value of the unknown correction coefficients i.e, $\mathbf{c}(x) = \{c_0(x)\ c_1(x)\}$ at each particle location. Similarly, equation 3.48 is also needed to solve to get the gradient of the correction coefficients i,e $\mathbf{c}'(x) = \{c_0'(x)\ c_1'(x)\}$ at each particle location. Figure 3.6 shows the solution for $\boldsymbol{C(x)}$ *and* $\boldsymbol{C'(x)}$ along the problem domain,

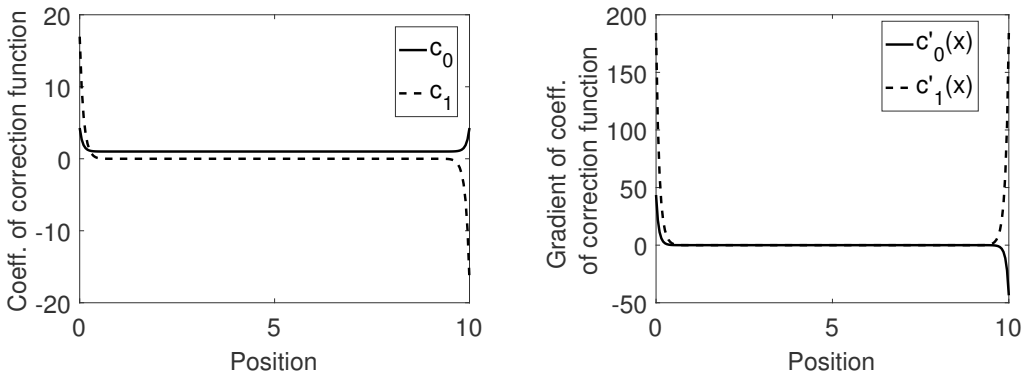

(a) (b)

Figure 3.6: The spatial variation of the RKPM coefficient (a)$\boldsymbol{C(x)}$ *and* (*b*)$\boldsymbol{C'(x)}$ for a 1-D problem.

It can be seen from figure 3.6 that the coefficients of the correction function and their gradient possess significant value near the domain boundary. In the interior of the domain, $c_0(x)$ becomes unity and all other coefficients are zero. i.e, those parts

of the domain which are far from the boundary, the RKPM corrected shape function is the same as SPH shape function. The two shape functions differ significantly only near the boundary. With the coefficients of the correction function already known, the RKPM shape function is used to approximate two simple functions. The reproducing capability of the RKPM shape function is shown in figure 3.7. It can be seen that the RKPM shape function is able to reproduce the function and it's gradient both at the interior as well as near the boundary of the domain. It's worthwhile to compare figure 3.7 with figure 3.5 to comprehend the improvement in the function and gradient approximation due to the incorporation of correction function into the kernel approximation.

As already mentioned in section 3.1 that the dynamic evolution of the dislocation density in the continuum domain is governed by the advection equation. The RKPM also self correct any error due to the wrong assignment of weight during nodal integration(see [56]).

3.4 Numerical Implementation of the Dislocation Propagation Scheme

As already discussed in section 3.2, the time evolution of the nucleated dislocations coming from the atomistic to the continuum region is modeled using the modified

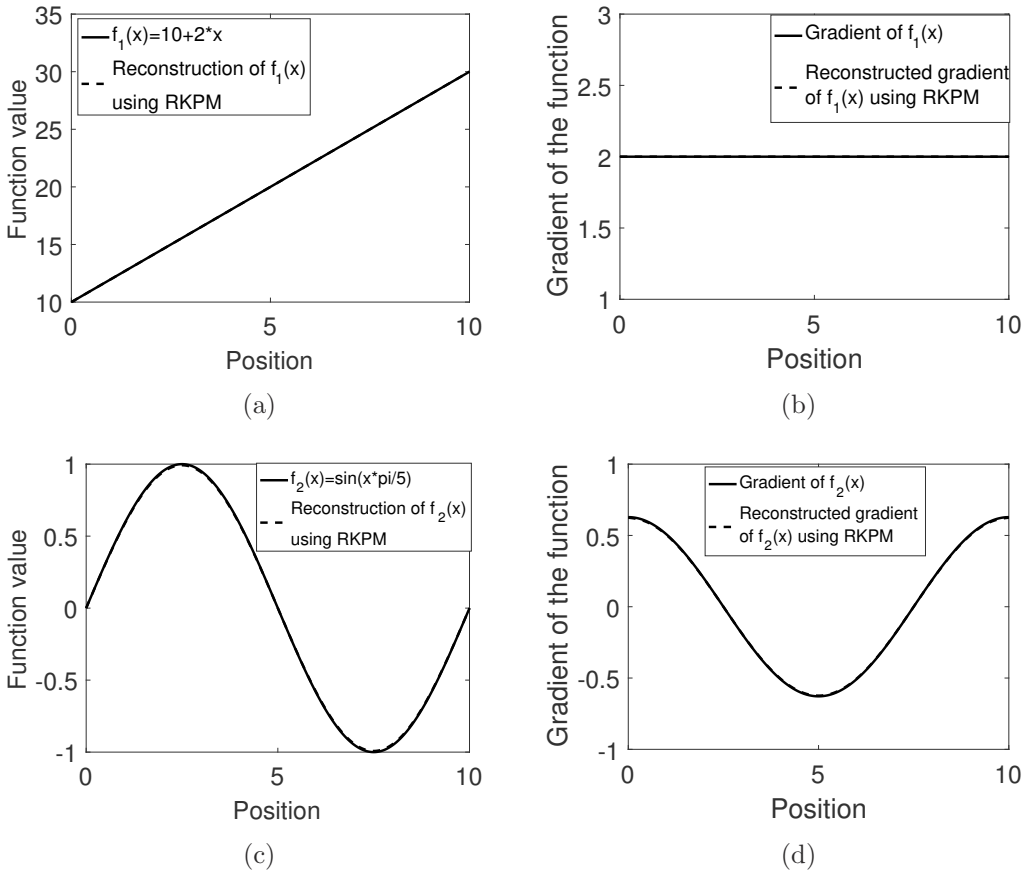

Figure 3.7: Reproducing capability of RKPM shape function for (a) a linear function, (s) slope of the linear function, (c) sine function and (d) slope of the sine function.

form of the advection equation given in equation 3.5. The localized nature of the dislocation density of individual dislocation necessitates a very fine discretization of the domain. Element based discretization will not be suitable for such problem because of the computational cost involved in generating a fine FE mesh. Due to this reason, element-based discretization will only be used for the solution of equation 2.7b i.e to obtain the solution of the displacement field only. For the solution of the equation 3.5, a mesh-free particle-based method is most appropriate. The Smooth

Particle Hydrodynamics(SPH) along with point collocation method is used for this purpose.

3.4.1 Point Collocation Method

In the point collocation method the discrete set of equations are obtained by satisfying the governing differential equation at each of the predetermined material points. The Smooth Particle Hydrodynamics(sec 3.3) is used as discretization method to solve the advection equation (eq. 3.5) over the domain. The discretized form of the differential equation at the $i'th$ particle and at time $t = n + 1$ becomes,

$$\left(\frac{\partial \psi}{\partial t}\right)_i^{n+1} + (\boldsymbol{v}.\boldsymbol{\nabla}\psi)_i^{n+1} = (\psi_s)_i^{n+1} \tag{3.49}$$

Equation 3.16 can be used to approximate the gradient $(\nabla\psi)$ using the kernel approximation. Then the above equation becomes,

$$\left(\frac{\partial \psi}{\partial t}\right)_i^{n+1} - (\boldsymbol{v})_i^{n+1}.\int_{\Omega_i} \psi^{n+1}\boldsymbol{\nabla}\overline{W}_i ds = (\psi_s)_i^{n+1} \tag{3.50}$$

where $\overline{W}_i$ is the RKPM kernel function corresponding to $i'th$ particle and the integration in the second term is over the support domain(Ω_i) of $\overline{W}_i$. Now imposing the particle approximation (sec. 3.3.2) on the integral term, the above equation becomes,

$$\left(\frac{\partial \psi}{\partial t}\right)_i^{n+1} - \boldsymbol{v}_i^{n+1}.\sum_{j=1}^{N_i} \psi_j^{n+1} \boldsymbol{\nabla} \overline{W}_i(\boldsymbol{x}_i - \boldsymbol{x}_j, h)\omega_j = (\psi_s)_i^{n+1} \tag{3.51}$$

To obtain the above equation from eq.3.50, the nodal integration is used in the second term of the left-hand side. The nodal integration technique is discussed in more detail in section 3.4.3. The time derivative in the first term can be approximated using the Finite Different Method, as;

$$\left(\frac{\psi_i^{n+1} - \psi_i^n}{\Delta t}\right) - \boldsymbol{v}_i^{n+1}.\sum_{j=1}^{N_i} \psi_j^{n+1} \boldsymbol{\nabla} \overline{W}_i(\boldsymbol{x}_i - \boldsymbol{x}_j, h)\omega_j = (\psi_s)_i^{n+1} \tag{3.52}$$

where, Δt is the increment in the time step. After rearrangement the equation 3.52 becomes,

$$\psi_i^{n+1} - \sum_{j=1}^{N_i} \boldsymbol{v}_i^{n+1}.\boldsymbol{\nabla} \overline{W}_i(\boldsymbol{x}_i - \boldsymbol{x}_j, h)\omega_j \Delta t \psi_j^{n+1} = \Delta t \, (\psi_s)_i^{n+1} + \psi_i^n \tag{3.53}$$

Equation 3.53 provides a set of linear algebraic equations with known right-hand side. Next, it's needed to impose the boundary condition

3.4.2 Imposing the Boundary Condition

Imposing Dirichlet bounday condition in mesh-less method is a key issue [57]. This is due to the fact that unlike in element based method, the interpolation function for particle based method does not satisfy the Kronecker delta property. i.e,

$$\overline{W}_i(x_i - x_j, h) \neq \delta_{ij} \neq \begin{cases} 1 \text{ if } x_i = x_j \\ \\ 0.0 \text{ if } x_i \neq x_j \end{cases} \tag{3.54}$$

Due to this reason, an algebraic equation is developed by satisfying the specified boundary condition for those particles at the boundary [56] and the equation developed by satisfying the governing differential equation at those particles are ignored.

3.4.3 Nodal Integration Scheme

The computational efficiency of the particle-based methods relies heavily on the integration technique that is used. Several methods have been developed over the years [54, 58, 59] to optimize the stability without sacrificing the computational efficiency of the particle-based method. Several of the proposed methods still require the background mesh for numerical integration which undermines the benefit of the particle-based discretization. The particle-based methods are truly mesh-less only when point collocation approach is used in conjunction with a nodal integration scheme [56]. In nodal integration scheme, the domain integral is approximated as,

$$\int_{\Omega} f(x) d\Omega \approxeq \sum_{i=1}^{N_i} f(x_i) \Delta\Omega_i \tag{3.55}$$

where $f(x)$ is any general function whose integration is sought over the domain Ω. It can be seen from the right-hand side of the above equation that the function is only

evaluated at nodal points (Also called particles). N_i is the number of particles used to discretize the domain(Ω). $\Delta\Omega_i$ is the weight associated with the i'th particle also called the nodal volume. For a non-uniform distribution of particles, the assignment of nodal volumes can be done using the continuity equation [58]. For uniformly distributed particles, a much simpler method like Voronoi tessellation can be used to assign the nodal volume to each particle. In the present study, particles are distributed uniformly, hence Voronoi tessellation based method is used to compute the weight associated with each particle. It has also been observed in [56] that the nodal volume is not needed to be assigned exactly as long as the same nodal volume is used to compute the moments of the kernel function (equ. 3.30, 3.45) while computing the coefficients of the correction function. Any error in the assignment of the nodal volume gets corrected during the computation of the coefficients of the correction function and reproducing conditions are satisfied exactly for both the function and it's derivatives.

3.4.4 Stabilizing the Smooth Particle Hydrodynamics method

The Smoothed Particle Hydrodynamics(SPH) is known to have instabilities [52, 60]. The instability also depends on the type of PDE that is being solved. Based on the 'von Neumann stability analysis' it has been proposed that [61], the instability

can be reduced significantly by appropriate choice of the smoothing length ('h' in equ. 3.20) for the kernel function. It has been suggested that for a stable solution the ratio between the smoothing length of the kernel function and the inter-particle distance should be in the range of 1.0 to 1.4. If the ratio is more than 1.4, then a large range of medium wavelengths(in Fourier space) have large dispersion[61]. A simple 1D example might be appropriate to understand the impact of the 'smoothing length(h) of the kernel function' on the stability of the SPH method.

Figure 3.8 shows the propagation of a Gaussian peak using Smooth Particle Hydrodynamics(SPH). The propagation is modeled using the 1D advection equation (1D version of equation 3.49 and without any source term) as,

$$\frac{\partial \psi}{\partial t} + v\frac{d\psi}{dx} = 0 \tag{3.56}$$

The domain size is 20 units which is uniformly discretized using 200 particles with inter particle distance(Δx) 0.01unit. The velocity of propagation is taken to be 1unit/sec. The initial density is assigned in the form of a Gaussian distribution function as,

$$\psi(x)_{t=0} = \frac{1}{\sqrt{2\pi}\sigma} e^{\frac{(x+5)^2}{2*\sigma^2}} \tag{3.57}$$

The distribution has it's peak value of 0.4unit at $x = -5$ and standard deviation(σ) of 2. The solution at each time step is obtained by numerically solving the equation 3.56 according to the procedure described in section 3.4.1. The time evolution of the

Gaussian density is obtained for two different values of the smoothing length of the kernel function('h' in equ. 3.20). One with $h/\Delta x = 2.3$ and another with $h/\Delta x = 1.3$.

Figure 3.8(a) and (b) show the time evolution of the Gaussian peak at time t=0 and at time t=10sec respectively with $h/\Delta x = 2.3$. It can clearly be seen the onset of instability at t=10 in figure 3.8(b). On the other hand with $h/\Delta x = 1.3$ the time evolution of the Gaussian peak does not show any instability as seen from figure 3.8(d). Hence in the present study, the ration between the smoothing length and the inter-particle distance is maintained to be 1.3.

3.4.5 Optimizing the computational cost by seeking for the solution at a localized regions

It has been seen in section 3.1 that the core of the dislocation is concentrated within a localized region with length scale in the order of $O(10|\boldsymbol{b}|)$, where $|\boldsymbol{b}|$ is the magnitude of the burger vector for the material. This necessitates a fine discretization of the domain. On the other-hand at any time-step, most of the domain remain free from the density of the nucleated dislocations. Figure 3.9(a) depicts a schematic representation of the above situation where the density of the nucleated dislocations are concentrated into some localized regions within the continuum domain. Hence it is computationally more suitable to localize the computational domain over which the evolution equation for the nucleated dislocations (equ. 3.5) is solved. To identify

these local sub-domains and achieve better computational efficiency the SPH particles are divided into several bins (figure 3.9(b)). The maximum dislocation density in each bin is tracked at each time step. All those bins with 'maximum dislocation density' more than a threshold density are considered to be containing the dislocation core, Ω_{DC}. The dislocation core region Ω_{DC} along with the immediate neighboring binsΩ_{DP} constitutes the local solution domain $\Omega_D = \Omega_{DC} \cup \Omega_{DP}$ over which the evolution equation for the nucleated dislocations (equ. 3.5) is solved.

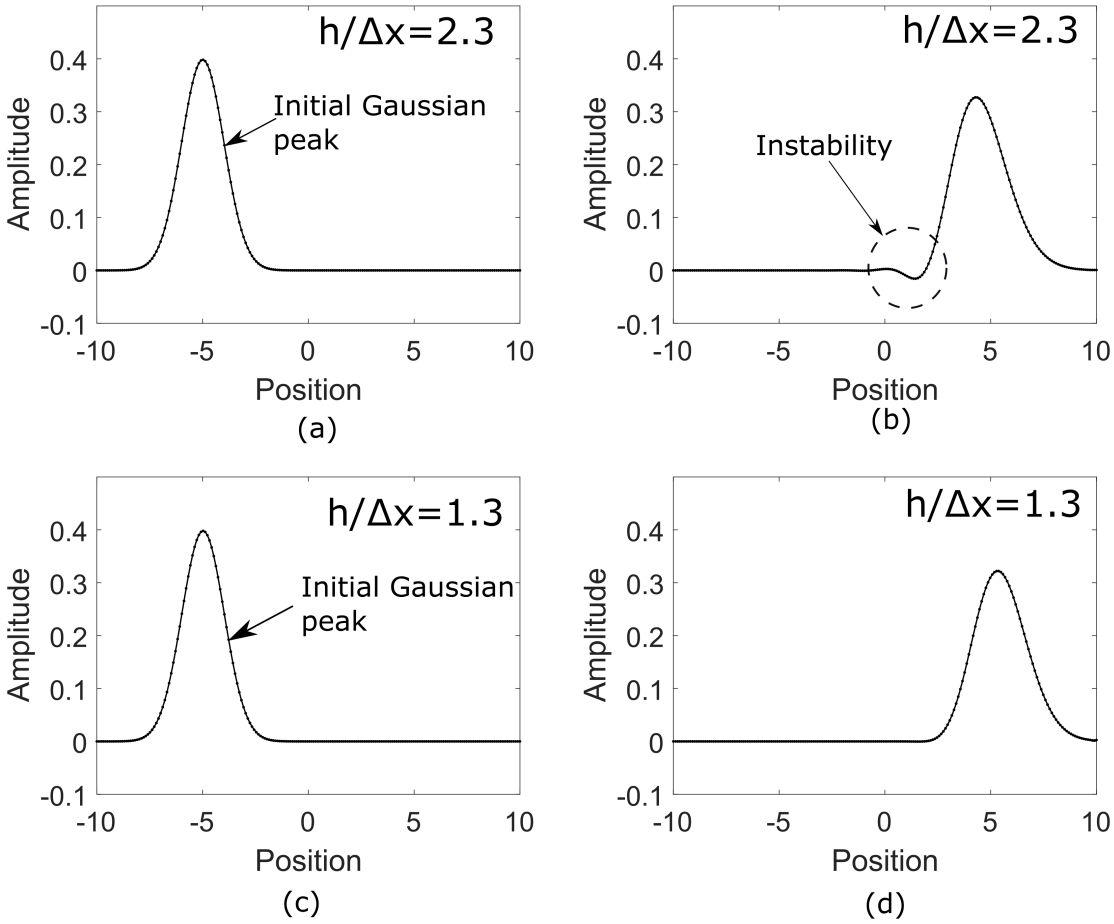

Figure 3.8: Instability associated with particle based method while solving the advection equation for the propagation of localized density. (a)The initial Gaussian peak of a scalar density gets (b)distorted due to the instability during the propagation. (c)The same Gaussian peak (d)remains preserved during propagation afer stabilization of the method.

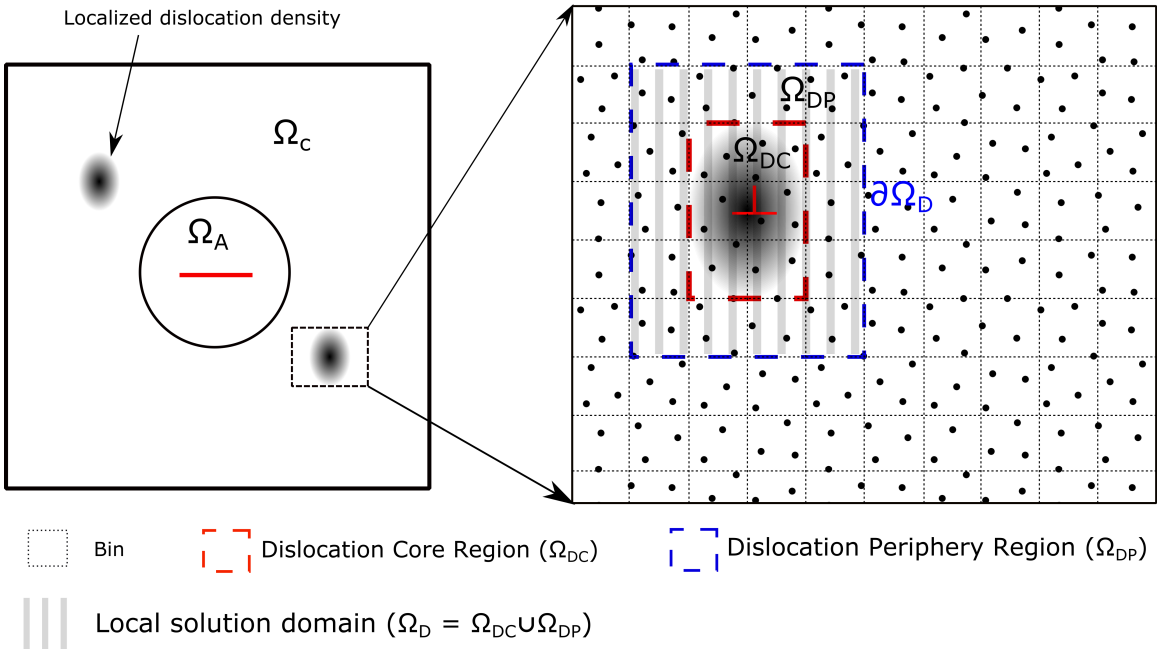

Figure 3.9: Schematic representation of the local solution domain for the propagation of the dislocation density in the continuum region.

Chapter 4

Time Acceleration of Molecular Dynamics using Strain Boost Hyperdynamics

MD simulations used to study fatigue and failure are often faced with serious limitations in realizing experimental strain-rates. The typically achieved MD time-scales are in the *nano- (ns)* to *micro-seconds (μs)* range, corresponding to atomic vibrations with time-period in the order of *pico-seconds (ps)*. Temporal resolutions required in the solution of the dynamical systems using incremental time-integration algorithms, limit the time-steps to be of the order of *femto-seconds (fs)*. Even with today's powerful computing platforms, this limits the maximum physical time to the *micro-second (μs)* range. Correspondingly, in the study of deformation mechanisms in a deformable

body, one is compelled to use very high strain-rates of $\sim 10^7$ or even higher to achieve strains of any physical significance. Thermal activation of stress-driven processes like nucleation of dislocations and micro-twins make the mechanical behavior of materials temperature and strain-rate dependent. Very high strain-rates in conventional MD simulations can result in very different activation regimes compared to those in laboratory experiments. This leads to the activation of different temperature and strain-rate dependent deformation mechanisms like surface-mediated dislocation nucleation [62]. High strain rate based MD simulations of fcc single crystal containing a crack in a certain orientation predicts a twin dominated deformation under mode-I loading, whereas room temperature experiments under similar loading do not show any twinning. This anomaly between experimental and simulation results has been attributed to the strain-rate effects in [36] where it has been shown that there is a transition from crack-tip twining at short times to full dislocation formation at long times.

In this chapter, the hyperdynamics-based accelerated MD method is discussed [47]. A brief description of different time-scale acceleration methods are given in section 4.1. In section 4.2 different aspects of the hyperdynamics method are discussed with a special focus on strain-boost hyperdynamics. Particular emphasis is on the construction of a boost potential with evolving parameters, as well as their implementation and validation. Finally in section 4.4.2, a comparative study of the strain-rate effect is presented using high strain-rate conventional MD and low strain-

rate hyperdynamics-based accelerated MD simulations.

4.1 Methods of Time-scale Accelerated Molecular Dynamics Simulations

Several methods have been developed for accelerating the temporal evolution of molecular systems, e.g. the parallel replica dynamics [63, 64], temperature accelerated dynamics [65], hyperdynamics [66], metadynamics [67], thermodynamics integration [68], umbrella sampling [69, 70], multi-canonical ensemble method [71] etc. Most of these methods are originally developed for non-driven systems i.e, the atomic system is not deformed by any externally applied force. Recently, a variant of metadynamics called Autonomous Basin Climbing [72], is extended to accelerate the time-scale for a driven system in [73]. This method needs to construct the potential energy surface (PES) after each load increment. This renders the method computationally expensive and makes the system size to be limited to a few thousands of atoms. Contrary to this, hyperdynamics is very effective for accelerating atomic-scale temporal evolution in crystalline systems. This method has been used in [24] to accelerate time-scales in the quasi-continuum method developed in [17]. Thermally activated substrate adaton diffusion [66], as well as stress-driven and thermally activated dislocation nucleation at sharp corners in metallic nano-pillars [37] have been studied using this

method. The *bond-boost* hyperdynamics is a variant of this method that has been implemented in [74] for concurrent multiscale coupling of atomistic with discrete dislocation dynamics models near a crack tip in aluminum. Alternatively, a powerful *strain-boost* hyperdynamics method has been developed in [37] to construct the boost potential. A few of the important methods suitable for the time acceleration of driven solid-state systems are briefly discussed in this section.

4.1.1 The Parallel Replica Dynamics (PRD)

The parallel replica dynamics or PRD method [63] is a simple yet accurate method that is based on the fact that most atomic processes are statistical in nature. It is based on the assumption that ensemble averaging over more micro-states is equivalent to exploring the system for longer time durations. This is achieved by temporal parallelization of the simulations over multiple processors, where individual processors run a replica of the sample independent of each other. This is in contrast with conventional parallelization, where the computational model is spatially distributed among multiple processors. The total number of micro-states explored in the PRD simulation process is the sum from all the processors. Hence the accumulated simulation time (t_{phy}) is related to MD time of the individual $i-th$ replica (t^i_{MD}) as:

$$t_{phy} = \sum_{i=1}^{i=S} t^i_{MD} \approx S t_{MD} \tag{4.1}$$

where S is the total number of replicas and t_{MD} is the average time. It is obvious that the level of acceleration that can be achieved is approximately proportional to the number of processors (or replicas) used.

4.1.2 The Temperature Accelerated Dynamics (TAD)

The temperature accelerated dynamics (TAD) [65] is a method of accelerating the time evolution of an atomic system, based on the observation that at finite temperatures an atomic system spends a substantial amount of time in the local potential well. Individual atoms vibrate with respect to their equilibrium position until an atom or a cluster of atoms acquire sufficient energy to overcome the local energy barrier and move to an adjacent potential well. The process continues until the system finds the global potential well. Material behavior is controlled by processes that are mainly stress-driven and/or thermally activated. Thermally activated processes, which correspond to the transition of a system from one local potential well to another, are inherently temperature-dependent. Thus, the rate of this transition increases with temperature as the thermal energy available to overcome the energy barrier increases. To accelerate these transitions, simulations are performed at elevated temperatures but also by eliminating any spurious transition that does not occur at the original temperature. The speed-up or boost SU_{TAD} that is achieved by this method is ex-

pressed as:

$$SU_{TAD} = exp\left[E_{min}\left(\frac{1}{K_b T_{low}} - \frac{1}{K_b T_{high}}\right)\right] \tag{4.2}$$

where E_{min} is the minimum energy barrier for state to state transition, T_{low} is the temperature at which the original MD simulation is intended, T_{high} is the elevated temperature at which the MD simulation is actually performed, and K_b is Boltzmann constant. A major challenge with this method is to come up with an appropriate criterion for filtering out the spurious transition, and extrapolating the state to state transition rate from an elevated temperature T_{high} to a lower one T_{low}.

4.1.3 Hyperdynamics (HD)

A very efficient way of accelerating the transition from one potential well to another for an atomic system had been proposed with the hyperdynamics or (HD) method in [49]. This method is based on lifting the basin of the potential-well or biasing the local potential landscape as shown in fig. 4.1). A boost potential is added to the original system potential shown with the solid line to lift the potential well. The biased potential shown with the dashed line makes state to state transition more frequent i.e, at an accelerated pace. Time evolution of the biased system and the unbiased system can be related using the *Transition State Theory (TST)* [75, 76, 77]. From the TST and equilibrium statistical mechanics based ensemble-averaging, it can be shown that time evolution of the atomic system under biased potential is related

to the MD time step as:

$$\Delta t_{phy} = \Delta t_{MD} exp \frac{\Delta V_b}{K_b T} \tag{4.3}$$

where Δt_{phy} is the actual time evolved for an incremental MD time of Δt_{MD}, ΔV_b is the boost potential applied to bias the system, T is simulation temperature and K_b is Boltzmann constant. A comprehensive mathematical construction of this method may be found in [49, 78].

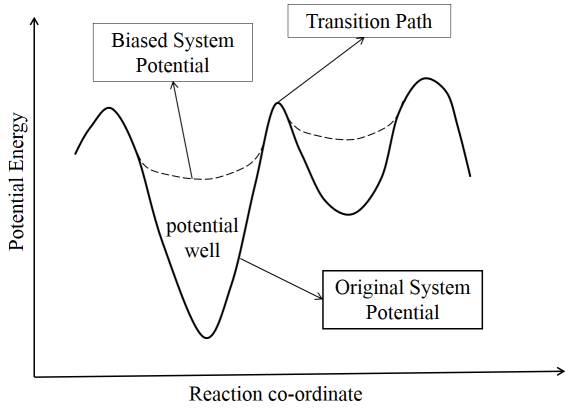

Figure 4.1: Schematic illustration of the hyperdynamics method. The solid line corresponds to the original system potential, while the biased potential is shown with the dashed line.

The most challenging task in this method is to construct the boost potential that will provide sufficient time acceleration, consistent with the TST. A general form of the boost potential is given as:

$$\Delta V(\mathbf{r}) = \frac{F}{N_b} \sum \delta V_i \tag{4.4}$$

where δV_i is the boost potential applied to the $i-th$ atom and N_b is the total number of atoms to be boosted. F is a stopping function that will drive the boost potential to zero as the system approaches the dividing surface, such that the assumption of hyperdynamics will not be violated. A number of methods have been proposed to construct appropriate boost potentials that will provide sufficient boost with minimal computational cost, e.g. in [79, 37, 80]. A *strain-boost* hyperdynamics formulation, proposed in [37], is adopted in the present study. In this model, the second invariant of the deviatoric local atomic strain (addressed as the Von-Mises shear strain invariant) is used to construct the boost potential. A major advantage of this approach is that the local atomic strain is a bond angle sensitive local geometric variable, which better reflects the condition of the nearest-neighbor atomic shell than the bond length alone [37]. This method is discussed in sec. 4.2.

Other sophisticated methods have also been developed for more complicated systems. Among these, the most widely used are metadynamics [67], thermodynamics integration [68], umbrella sampling [69, 70], multicanonical ensemble [71]etc. These methods are most suitable to study more complicated systems, e.g, reaction mechanism of different molecular systems in the liquid phase, conformational changes of long molecular chains in solution, protein folding, protein-protein interaction, phase transition, etc. In metadynamics, the system is adaptively biased by iterative injection of a small Gaussian potential, which is a function of carefully chosen collective

state variables. A major advantage of this method is that history-dependent bias prevents the system from visiting those parts of the phase-space, which it has already explored. By injecting a smaller Gaussian potential successively, the free energy of the system can be estimated with high accuracy. In thermodynamics integration [68] the transition is accelerated by constraining the reaction coordinates at different values in multiple windows and forcing the system to sample along a line perpendicular to the reaction coordinate. Special care has to be taken to constrain the reaction coordinate in an energy-conserving manner. Contrary to thermodynamics integration, in umbrella sampling [69] the reaction coordinate is not constrained in multiple windows, but rather pulled to a target value by using appropriate bias potential [70].

These methods will be most suitable if the free energy of the system is not known a priori. Such cases arise when the system of interest is complicated and transition of interest is preceded by many non-interesting events manifested by local potential wells. In contrast, the problem investigated here includes plastic deformation of crystalline material, where the event of interest is very precise i.e, nucleation of dislocations. The energy barrier corresponding to that transition can be estimated by some trial MD simulation with a much smaller system size. This is discussed in section 4.2.2.

4.2 Strain Boost Hyperdynamics

The boost potential used in the present study is a function of the second invariant of the least-square atomic strain, as given in [81]. With this augmentation, equation (4.4) takes the form:

$$\Delta V(\mathbf{r}) = \frac{F(\eta_{max}^{Mises})}{N_b} \sum \delta V_i(\eta_i^{Mises}) \qquad \text{where} \tag{4.5a}$$

$$\delta V_i(\eta_i^{Mises}) = V_{max}\left[1 - \left(\frac{\eta_i^{Mises}}{q_c^{max}}\right)^2\right] \tag{4.5b}$$

Here η_i^{Mises} is second invariant of the local atomic strain η_i of the $i-th$ atom and η_{max}^{Mises}=max $\{\ \eta_i^{Mises}, i = 1, 2, ..., N_b\}$, where N_b is the number of boost atoms. δV_i is boost potential, which is a function of $\eta_i^{Mises}(\mathbf{r})$. $F(\eta_{max}^{Mises})$ is the stopping function that enforces the hyperdynamics assumptions on the boost potential at transition. The following form of stopping function is used in this study.

$$F(\eta_{max}^{Mises}) = \begin{cases} 1 - \left(\frac{\eta_{max}^{Mises}}{q_c^{max}}\right)^2, & \forall\ \eta_{max}^{Mises} < q_c^{max} \\ 0 & \forall\ \eta_{max}^{Mises} \geq q_c^{max} \end{cases} \tag{4.6}$$

The cardinal ingredient in constructing both the boost potential and stopping function is the atomic strain. The procedure to compute local atomic strains from

given atomic configurations is discussed next. Consider two configuration of an atomic system, one at time $t = 0$ denoted as the reference configuration $\mathbf{x_i^0}$ and other at time t designated as the current configuration $\mathbf{x_i}$. The separation vector of an atom i with it's neighbor j in the reference configuration and current configuration are respectively written as:

$$\mathbf{d}_{ji}^0 = (\mathbf{x}_j^0 - \mathbf{x}_i^0) \quad \text{and} \quad \mathbf{d}_{ji} = (\mathbf{x}_j - \mathbf{x}_i) \tag{4.7}$$

For this discrete system, the objective is to realize a function $\mathbf{J}_i$ that maps the vector from the reference to current configuration, i.e.

$$\mathbf{d}_{ji}^0 \xrightarrow{\mathbf{J}_i} \mathbf{d}_{ji} \quad \forall \quad j \in N_i \tag{4.8}$$

where N_i is the set of all neighbors of $i-th$ atom. In [81] the function $\mathbf{J}_i$ is determined in a least-square sense by minimizing the total mapping error $(\sum_{j=1}^{N_i}(\mathbf{d}_{ji}^0\mathbf{J}_i - \mathbf{d}_{ji})^2)$. This minimization leads to a functional form of tbe deformation gradient for a discrete system as:

$$\mathbf{J}_i = \mathbf{V}_i^{-1}\mathbf{W}_i \tag{4.9}$$

where

$$\mathbf{V}_i = \sum_{j=1}^{N_i} \mathbf{d}_{ji}^{0T}\mathbf{d}_{ji}^0 \quad \text{and} \quad \mathbf{W}_i = \sum_{j=1}^{N_i} \mathbf{d}_{ji}^{0T}\mathbf{d}_{ji} \tag{4.10}$$

Upon evaluation of the deformation gradient $\mathbf{J}_i$ matrix, the Lagrangian strain $\boldsymbol{\eta}_i$ for

a discrete system may be constructed as:

$$\boldsymbol{\eta}_i \equiv (\mathbf{J}_i \mathbf{J}_i^T - \mathbf{I}) \tag{4.11}$$

where $\mathbf{I}$ is the identity matrix. For a frame-invariant boost potential that is independent of reference frame, its construction uses the second invariant of the deviatoric part of $\boldsymbol{\eta}_i$, given as:

$$\boldsymbol{\eta}_i^{Mises} \equiv \sqrt{\frac{1}{2} Tr(\boldsymbol{\eta}_i - \eta_i^{hydro}\mathbf{I})^2} \tag{4.12}$$

where Tr is the trace and η_i^{hydro} is the hydrostatic part of the $\boldsymbol{\eta}_i$. The atomic strain-based boost potential construction requires two parameters V_{max} and q_c^{max} in equations (4.5) and (4.6). Details on how to calculate these parameters for a specific material are discussed in sections 4.2.2 and 4.2.3.

An important prerequisite of hyperdynamics is to make the boost potential δV_i go to zero on all dividing surfaces, as the system approaches a saddle point for the transition from one local potential well to another as shown in figure 4.1. A method of finding these saddle points of the potential surface is by calculating the gradient vector $g_i(= \partial V/\partial x_i)$ and the Hessian matrix $H_{ij}(= \partial^2 V/\delta x_i \partial x_j)$. Here $\mathbf{x}$ is 3N dimensional vector where N is the number of atoms in the system [49]. Solving for g_i=0 will give all the extremums of the energy surface. Of these points, the one for which the Hessian matrix has one negative eigenvalue belongs to the saddle point.

However, a problem with this approach is that the energy surface is not known *a-priori*. Additionally, finding all solutions of $g_i = 0$ for a $3N$ dimensional potential energy function, and the eigenvalues of the corresponding Hessian matrix H_{ij} is a computationally expensive process and almost intractable for large systems.

A consideration used to overcome this problem is that, whenever a system passes through the saddle point for a transition from one local potential well to another, it undergoes some major configurational change in the atomic system involving at least one atom and it's nearest neighbors. Consequently, any state variable that reflects this configurational change can be used as an indicator of the transition. The critical value of this indicator can be used as a threshold beyond which the boost potential will be forced to zero. In the present study, the stopping function $F(\eta_{max}^{Mises})$ in equation (4.6) serves this purpose, where q_c^{max} is the critical value of η_{max}^{Mises}. Figure 4.2 shows the evolution of potential energy and η^{Mises} at T=2K for a typical atom in the ensemble during the nucleation of a leading partial dislocation at approximately 252 *ps* into the simulation.

Substantial changes in the magnitude of η^{Mises} at the onset of nucleation makes it a perfect indicator of the transition. An alternate indicator, proposed for bond-boost hyperdynamics in [79], is the critical bond length. Whenever a tagged bond crosses some critical length, the system is considered to be on the verge of a transition from

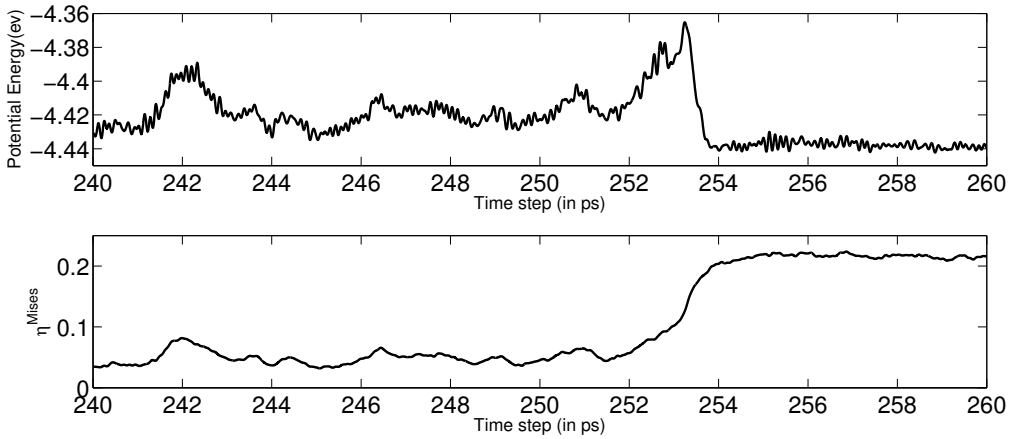

Figure 4.2: Time evolution of potential energy and η^{Mises} of a typical atom in the ensemble at $T = 2K$.

the current potential well to an adjacent one. In the present analysis, the aim is to investigate dislocation dominated crack tip plasticity. For this problem, the strain-boost model is chosen over the bond-boost method since dislocation nucleation is a collective behavior of an atomic cluster. The local atomic strain is a better collective variable, which involves at least one atom and it's nearest neighbors in comparison with the maximum bond length between an atom and it's neighbor. Noteworthy in this discussion is the fact that twin nucleation and twin-boundary propagation involves sequential nucleation of leading partials on parallel slip planes.

4.2.1 Hyperdynamics for driven systems

The original development of hyperdynamics in [66] was for non-driven systems, where the potential energy of the system and energy barrier between states remain

unchanged. This renders the TST rate to remain constant throughout the simulation for both the biased and the original systems. The ratio of these two rate constants is interpreted as the acceleration in time-scale due to the applied bias and is quantified in the form of a boost factor. For a driven system examined in present study, the TST rate at two different strain states are different. However for a carefully chosen boost potential, the ratio of the TST rate for the biased system and the original system can remain unchanged throughout the simulation. This means that the applied macroscopic strain influences the TST rate of both the biased and original systems in same manner. This implies that for two consecutive time steps t_1 and t_2 with macroscopic strains ϵ_1 and ϵ_2, even though

$$K^{TST}_{A\to B}\Big|_{\epsilon_1} \neq K^{TST}_{A\to B}\Big|_{\epsilon_2} \quad \text{and} \quad K^{TST}_{A_b\to B}\Big|_{\epsilon_1} \neq K^{TST}_{A_b\to B}\Big|_{\epsilon_2} \tag{4.13}$$

the following relation still holds:

$$\frac{K^{TST}_{A_b\to B}}{K^{TST}_{A\to B}}\Big|_{\epsilon_1} \approx \frac{K^{TST}_{A_b\to B}}{K^{TST}_{A\to B}}\Big|_{\epsilon_2} \tag{4.14}$$

The notations used have the same meaning as in [66]. Consequently, the criterion to be satisfied is,

$$\frac{K^{TST}_{A_b\to B}}{K^{TST}_{A\to B}}\Big|_{\epsilon_1} = \frac{K^{TST}_{A_b\to B}}{K^{TST}_{A\to B}}\Big|_{\epsilon_2} \tag{4.15}$$

From the relations in [66],

$$K^{TST}_{A\to B} = \frac{\left\langle |v_A|\delta_A(\mathbf{r})\right\rangle_{A_b}}{\left\langle e^{\beta\Delta V_b(\mathbf{r})}\right\rangle_{A_b}} \tag{4.16}$$

The numerator in the right hand side is the TST rate constant under a biased potential. This renders equation (4.16) to be

$$K^{TST}_{A\to B} = \frac{K^{TST}_{A_b\to B}}{\left\langle e^{\beta\Delta V_b(\mathbf{r})}\right\rangle_{A_b}}, \quad \Longrightarrow \quad \frac{K^{TST}_{A_b\to B}}{K^{TST}_{A\to B}} = \left\langle e^{\beta\Delta V_b(\mathbf{r})}\right\rangle_{A_b} \tag{4.17}$$

Substituting equation (4.17) in equation (4.15) yields:

$$\left\langle e^{\beta\Delta V_b(\mathbf{r})}\right\rangle_{A_b}\Big|_{\epsilon_1} = \left\langle e^{\beta\Delta V_b(\mathbf{r})}\right\rangle_{A_b}\Big|_{\epsilon_2} \tag{4.18}$$

For constant temperature, the parameter $\beta(=\frac{1}{K_B T})$ remains unchanged throughout the simulation. So, for equation (4.18) and consequently equation (4.15) to hold, the applied boost potential has to be independent of macroscopic strain ϵ, i.e.

$$\Delta V_b(\mathbf{r})|_{\epsilon_1} = \Delta V_b(\mathbf{r})|_{\epsilon_2} \tag{4.19}$$

In the present study, it is observed that the effect of the macroscopic strain is more prominent on η^{Mises}_{max} than on η^{Mises}_{i}. For the strain boost hyperdynamics, the effect of η^{Mises}_{max} on the boost potential comes through the construction of a stopping

function given in equations (4.5) and (4.6). To mitigate this effect of macroscopic strain, the parameter V_{max} is monitored using the value of stopping function to keep the strength of the bias close to the activation free energy of nucleation. This procedure is discussed in details in section 4.2.2.

It is also noteworthy that classical statistical mechanics-based ensemble averaging, which is used to relate the MD-time (Δt_{MD}) with physical time (Δt_{phy}), (see equation (4.3)), can only be applied for thermally equilibrated systems. However, many problems of interest in the mechanics of materials are not only thermally activated but stress-driven as well. One prime example is the nucleation of dislocations or gliding of existing dislocations when a critical resolved shear stress is exceeded. One approach to keep the system near thermal equilibrium is to use a stepped loading in lieu of a continuous ramped loading [82] and apply hyperdynamics using the instantaneous near-equilibrium system potential corresponding to the non-driven segment of the loading. In the present study, the system is far from equilibrium only when dislocation nucleates and continues until it reaches a stable configuration, or when dislocations in a stable configuration start gliding again due to the buildup of resolved shear stress to a critical value. During these far from equilibrium system-states, hyperdynamics is not activated, to comply with the methods basic assumptions. Other than these two non-equilibrium scenarios, the system mostly deforms elastically under quasi-equilibrium conditions. Furthermore, the system is forced to near-equilibrium

states by imposing the macroscopic strain using affine transformation.

4.2.2 Determination of V_{max}

The parameter V_{max} in equation (4.5b) is an important determinant of the maximum achievable boost and in turn temporal acceleration of the MD simulations. It should be high enough to give sufficient boost, while not creating any extra local potential well of significant depth. Rearranging equations (4.5a), (4.5b) and (4.6) yields,

$$\begin{aligned} \Delta V(\mathbf{r}) &= \frac{S}{N_b} \sum \left[1 - \left(\frac{\eta_i^{Mises}}{q_c^{max}} \right)^2 \right] \qquad \forall\ \eta_{max}^{Mises} < q_c^{max} \\ &= 0 \qquad\qquad\qquad\qquad\qquad\qquad \forall\ \eta_{max}^{Mises} \geq q_c^{max} \end{aligned} \tag{4.20}$$

where,

$$S = V_{max} \left[1 - \left(\frac{\eta_{max}^{Mises}}{q_c^{max}} \right)^2 \right] \tag{4.21}$$

S is termed as *strength of the bias*. In general, at the onset of transition, S should be of the order of the potential barrier height that an atom has to overcome to initiate any nucleation. This will also guarantee that there will be no extra potential well created inside the original one near the dividing surface. A qualitative assessment of this barrier height (0.2ev for the present study at 300K) can be obtained by monitoring the time evolution of potential energy of a typical atom as it participates in

the nucleation process, as shown in figure 4.3. It can be seen that after repeated failed attempts for which η^{Mises} touches the $\eta^{Mises}_{max} = 0.9q_c^{max}$ line, the atom acquires sufficient thermal energy at $\approx 324ps$ to overcome the potential barrier and nucleate a leading partial dislocation. Every material has its own characteristic potential barrier height corresponding to the event of interest. Once the barrier height is obtained, V_{max} can be calculated using equation (4.21) as:

$$V_{max} = \frac{S}{[1 - (\frac{\eta^{Mises}_{max}}{q_c^{max}})^2]} \tag{4.22}$$

with known η^{Mises}_{max}. In the present implementation, V_{max} is adjusted during the simulation based on the average value of η^{Mises}_{max}. The running time average of η^{Mises}_{max} is calculated based on the last 5000 MD-steps. For example, if the average η^{Mises}_{max} is $0.5q_c^{max}$, for the strength of bias (S) to be same as the potential barrier height i.e, 0.2 ev, V_{max} is set to be 0.2667. This process of continuous monitoring of V_{max} guarantees that the instantaneous boost potential will never exceed the activation free energy of nucleation. It is noteworthy that η^{Mises}_{max} is the maximum value of η^{Mises} among all atoms that are boosted. Of these atoms, the identity of the most critical atom keeps changing with the progress of the simulation. Figure 4.3 shows the time evolution of potential energy and η^{Mises} of one such atom. For the system studied, it is observed that at the onset of transition, the critical atoms frequently visit the state corresponding to $\eta^{Mises} \sim 0.9q_c^{max}$. The instantaneous boost potential for that

particular atom, corresponding to this state, is 0.0380ev (from equation (4.20) with S=0.2ev).

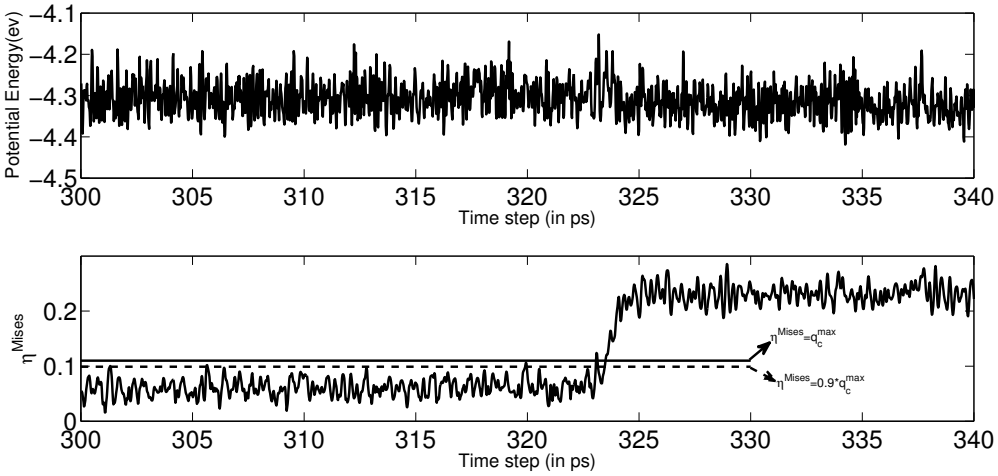

Figure 4.3: Time evolution of potential energy and η^{Mises} of a typical atom in the ensemble at $T = 300K$.

Determination of the optimal V_{max} is crucial. Higher V_{max} will lead to a wrong conversion of the MD time (Δt_{MD}) to the physical time (Δt_{phy}). In general, the strength of bias S should be similar to the activation free energy of nucleation. The present implementation enforces this condition by adjusting V_{max} during the simulation. Another way to make this adaptive adjustment is by monitoring the frequency at which the identity of the most critical atom changes. This makes the requirement of prior knowledge of the energy barrier redundant. A more detailed description of the procedure with an application on bond-boost hyperdynamics (also called Self-learning Bond Boost method) can be found in [83, 84].

Determination of S and hence V_{max}, sometimes can be challenging if the free energy corresponding to the event of interest is not known a priori. This situation arises when hyperdynamics itself is needed for the occurrence of those infrequent events in atomistic simulations such as in atomic diffusion in solids. A better approach for such situations is to use metadynamics [67] or a more sophisticated adaptive-boost MD [85] to get an approximate idea of the potential barrier height with a little additional computational cost.

4.2.3 Determination of q_c

To find the optimal value of the threshold parameter q_c^{max}, MD simulations are performed for a small atomistic ensemble with an embedded crack (created by removing few layers of atoms) to facilitate inhomogeneous nucleation of crack-tip dislocations. The parameter q_c^{max} indicates that the system is approaching a transition point, even without any additional thermal vibration. Hyperdynamics must stop beyond that point, i.e. the boost potential should go to zero to comply with it's assumption. q_c^{max} is inherently dependent on temperature due to the contribution from thermal vibration of the atomic system. An iterative technique is used in this study to find the optimal value of q_c^{max} at a particular temperature.

The potential energy of the system is first obtained for two different temperatures,

one being very low (2K for the present study) and the other corresponding to the temperature at which q_c^{max} is expected. The boost potential is then applied and the simulations culminating in system quenching are run corresponding to different assumed trial parameter values q_c^{trial}. If q_c^{trial} is equal to the critical threshold value q_c then the system will make a transition without any additional thermal fluctuation. The equilibrated potential energy determines whether the quenched system has made this transition, as elucidated in figure 4.4. For $q_c^{trial} = 0.1$ the system does not make the transition and falls back to the potential energy corresponding to the lower temperature pathway 2K. However transition takes place for $q_c^{trial} = 0.12$ and $q_c^{trial} = 0.13$. To obtain the minimum value of q_c^{trial} for which transition takes place, the quench-simulation process is repeated with different initial atomic configurations by dephasing. The critical q_c is assessed from this exercise. In this study, the parameter q_c^{trial} is gradually incremented from 0.8 to 0.15 with a step size of 0.001, and the critical value is found to be $q_c = 0.12$ at 300K. Any value of q_c^{max} less than this critical q_c is safe. A conservative value of q_c^{max}=0.11 is used for all subsequent studies. A value of $q_c = 0.095$ at 200K has been used in [37] for the study of dislocation nucleation in copper nanopillars under compressive loading.

4.2.4 Determination of N_b

The number of atoms N_b that needs to be boosted in equation (4.5a) is another important parameter to be determined. The calculation of boost potential and cor-

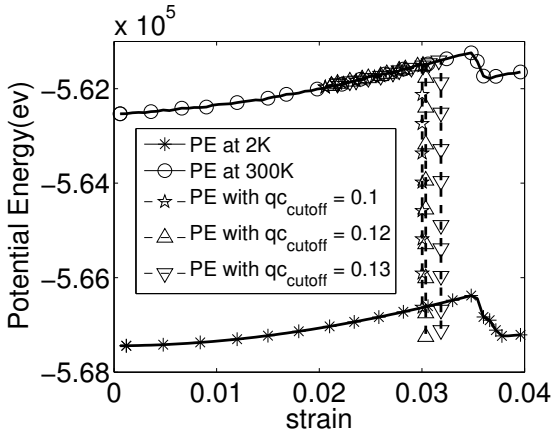

Figure 4.4: Plot of the potential energy as a function of applied strain corresponding to different temperatures in the quenching bath for determining q_c.

responding forces involve some computational costs per atom. Hence, computational efficiency requires an optimally low number of atoms to be boosted while making sure to include the cluster of atoms that is most critical for the nucleation process. Since this work focuses on the investigation of plastic deformation of a nickel single crystal in the presence of an atomistic crack, the crack tip region is the most critical part for nucleation. Consequently, at the start of simulations, only a small through-thickness cylindrical domain with its center at the crack tip is boosted. This is demonstrated in figure 4.5. Based on potential energy, additional atoms are tagged as *to-be-boosted*, as the material deforms plastically. It should be noted that since the least-squares based deformation gradient is not a good measure of the local atomic strain for atoms with a low near-neighbor count, atoms with less than 12 first nearest neighbors for fcc crystals are not boosted in this work.

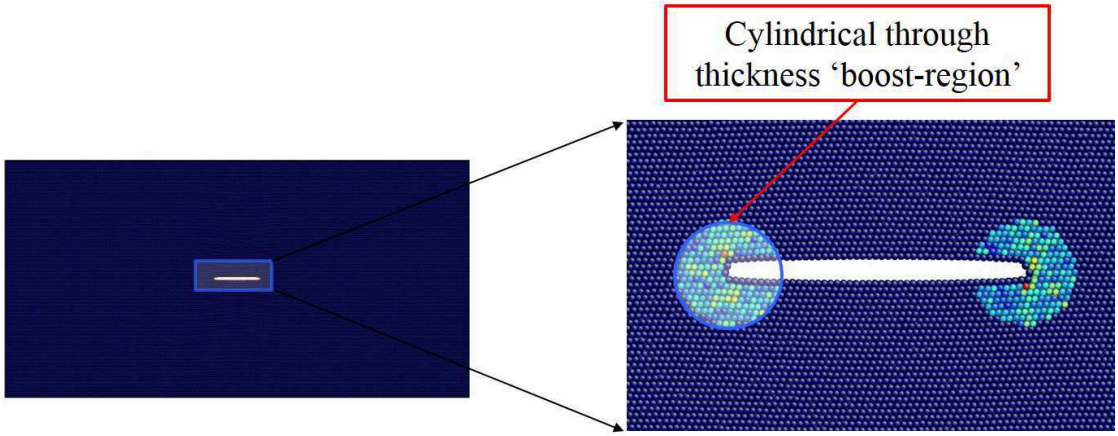

Figure 4.5: (a) A 3D atomic domain of single crystal nickel with an embedded crack for MD simulations, and (b) zoomed in view of the boost region for HD based accelerated MD simulations. The color of atoms is based on the second invariant of atomic strain (η_i^{Mises}) corresponding to 1% macroscopic strain.

4.3 Implementation of the Strain-Boost Hyperdynamics in LAMMPS and Accelerated MD Simulations

The strain boost- based hyperdynamics method is implemented in a parallel version of the popular MD simulation code *Large-scale Atomic/Molecular Massively Parallel Simulator or LAMMPS* [38]. To keep the main structure of the LAMMPS unchanged, an additional "compute" module is incorporated. For a given reference and current configuration, this module calculates (i) the local least-squares based atomic-strain per atom, (ii) the boost potential per atom, and (iii) the additional force due to the boost potential per atom. For preliminary verification of this implementation, an

MD model specimen is created in LAMMPS and subsequently deformed by using the "fix-deform" option without performing any time integration, thus eliminating any noise due to thermal vibration. The least-squares based deformation gradient is computed using equation (4.9) for three different load cases viz. pure translation, pure rotation and pure stretch. The computed values are in agreement with the known deformation gradients for these deformation modes.

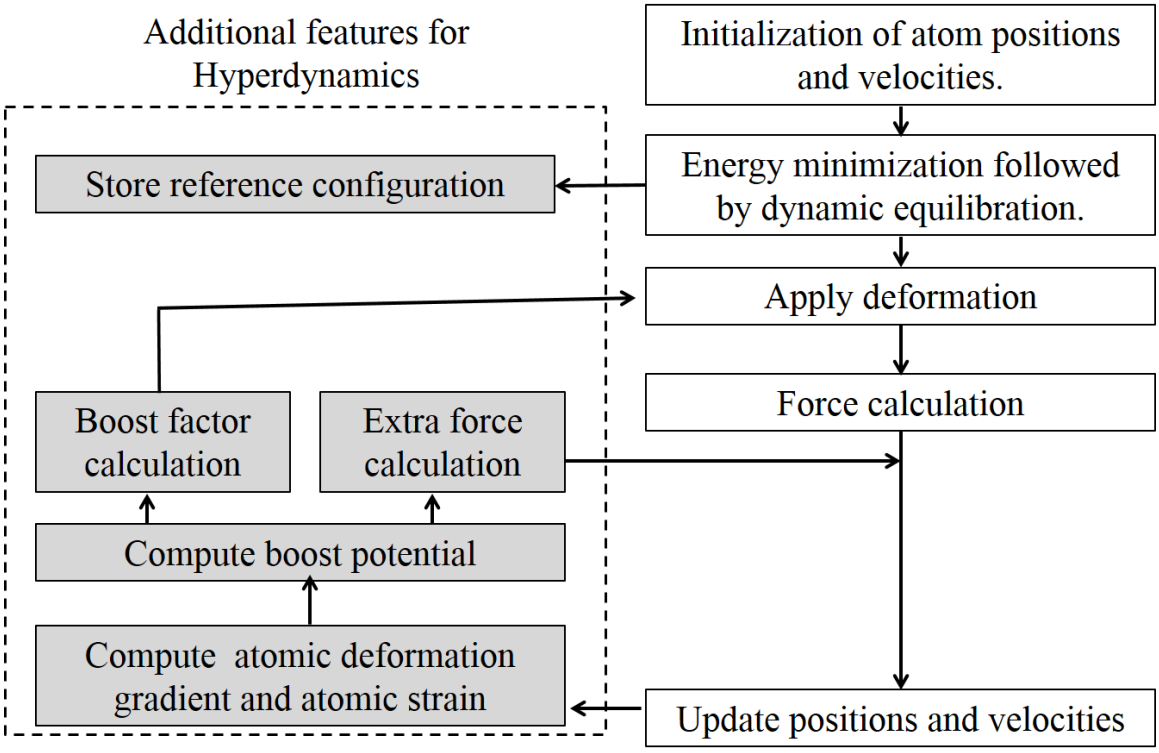

Figure 4.6: A flowchart showing the strain-boost hyperdynamics implementation in LAMMPS. Tasks inside the dashed box are added for the hyperdynamics acceleration in conjunction with the conventional MD operations.

The process of strain-boost hyperdynamics implementation in LAMMPS is briefly

discussed in this section with a schematic depiction in figure 4.6. The atomistic simulation specimen is created by filling the sample geometry with atoms conforming to the crystallographic lattice structure of the material in consideration. For investigating crack tip plasticity, an atomic crack is placed symmetrically at the center of the specimen by removing a few layers of atoms as shown in figure 4.5. This is followed by static minimization of the total potential energy for the equilibrium configuration of the system. Next, the initial velocity of atoms is specified, based on the Maxwell-Boltzmann distribution for the simulation temperature taken to be 300K in this study. Dynamic equilibration using the Nose-Hoover thermostat [86, 87] is carried out to achieve traction free outer surfaces while maintaining the system temperature. The equilibrated atomic positions are stored as the reference configuration. This is needed for computing the deformation gradients and atomic strains in subsequent simulations. This reference configuration will be updated once nucleated dislocations glide to their stable configuration.

Following equilibration, the system is deformed by displacing individual atoms conforming to the affine transformation, thereby achieving an incremental ensemble strain of $\Delta\epsilon$, given as:

$$\Delta\epsilon = \Delta t_{phy}\dot{\epsilon} \tag{4.23}$$

Δt_{phy} is the physical time at which the atomic system evolves under the boost potential ΔV. Following equation (4.3), it is related to the MD time step Δt_{MD} as

$\Delta t_{phy} = \Delta t_{MD} exp(\Delta V / K_b T)$. The displacement step is followed by the calculation of conventional forces due to the inter-atomic interaction and additional forces due to boost potential. The system is accordingly moved forward in time by integrating the equations of motion using a velocity-Verlet time integration scheme [88]. Once the positions and velocities are updated, the new atomic strain, total per atom force (inter-atomic interaction force + boost force) and boost factor ($exp(\Delta V / K_b T)$) per atom are respectively calculated. Subsequently, the system is deformed by an incremental strain of $\Delta\epsilon$ according to equation (4.23) and the process continues.

4.3.1 Validation of the Strain-Boost Hyperdynamics Model with Conventional MD Results

Prior to the use of strain-boost hyperdynamics based MD simulation for low strain-rate deformation analysis, it is important to validate the model with results from conventional MD simulations. To accomplish this, hyperdynamics-based accelerated MD and conventional MD simulations are conducted for an atomistic model of single-crystal nickel specimen. The atomic simulation specimen has physical dimensions of $100nm \times 50nm \times 25nm$, which consists of $\sim$ 10 million atoms. The orientation of the crystal is $x \rightarrow [\bar{1}10]$, $y \rightarrow [111]$, $z \rightarrow [11\bar{2}]$. A through-thickness uniform crack of width $10nm$ is embedded in the specimen. Two different strain-rates, viz. $10^7\ s^{-1}$ and $10^8\ s^{-1}$, are applied to the simulations for comparison. The resulting macro-

scopic stress-strain response and evolution of dislocation density are shown in figure 4.7. The critical nucleation stress and the evolution of different dislocation densities e.g. mobile and immobile dislocations by the two methods are in good agreement. It is noteworthy that hyperdynamics is most effective when the events of interest are very infrequent, which makes the achievable boost to be dependent on temperature. At higher temperatures, the occurrence of infrequent events is aided by the higher kinetic energy of individual atoms that in turn reduces the achievable boost.

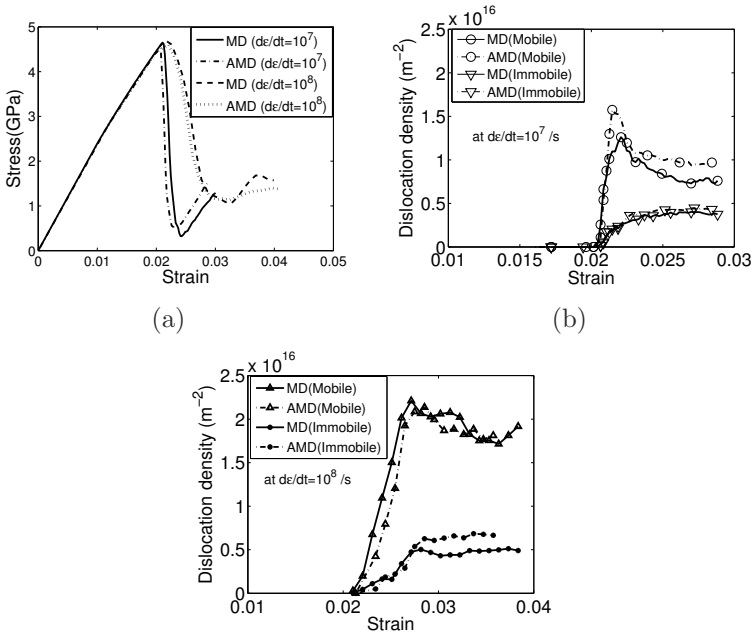

Figure 4.7: Validation of the strain-boost hyperdynamics-based MD model with conventional MD results: Comparisons of (a) volume averaged stress and (b,c)dislocation densities, as a function of the macroscopic strain.

To investigate the temperature and strain-rate dependence on the achievable boost, similar computational experiments are performed for different strain-rates viz.

10^9, 10^8 and 10^7 and temperatures viz. 100K and 300K. The achieved average strain-boost is calculated by monitoring the CPU time taken by the two methods. To extend the achievable boost prediction for lower strain-rates of $\sim 10^4$, hyperdynamics-based MD simulations are performed to get the first nucleation event. These rates are beyond the reach of conventional MD with most current computational platforms. With knowledge of the critical strain for nucleation for a particular strain-rate and temperature, the total number of MD steps that would have been needed for conventional MD can be approximately calculated. The ratio of time steps with conventional MD to that with hyperdynamics, multiplied by an adjustment factor to take care of the additional computation in hyperdynamics gives an idea of the achievable boost. Figure 4.8 shows an exponential increase of this achievable boost with decreasing strain-rates. This is the desired benefit of accelerated MD simulations.

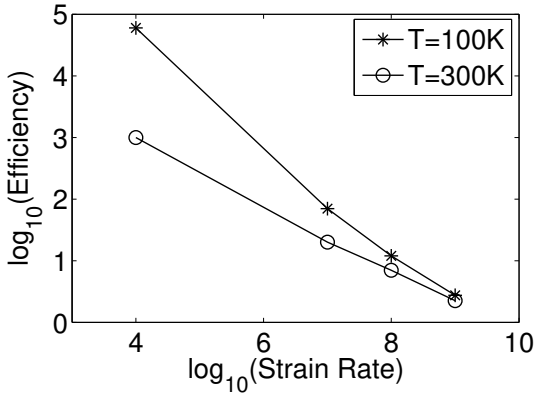

Figure 4.8: Efficiency of the hyperdynamics-based MD model for different strain-rates and temperatures.

4.4 Numerical Simulation of a Crystalline Material with an Embedded Crack

The examples in this section revisit the characterization and quantification of atomic-level deformation mechanisms obtained by conventional MD simulations of a crystalline material with an embedded crack in [16]. The strain-boost hyperdynamics based accelerated MD simulations are used to compare the deformation mechanisms at the high strain-rates similar to those in [16]. On the other hand, simulations at lower strain-rates are examined for the effectiveness of predictions based on high strain rate MD simulations.

4.4.1 MD model of a Single Crystal Nickel with an Embedded Crack

The geometric features and loading characteristics of a single crystal nickel specimen with an embedded crack are shown in figure 4.9. A similar model has been used in [16], where it was established that a simulation box size of $80nm \times 44nm \times 25nm$ is sufficient for the boundary effects to be insignificant on crack-tip dislocation nucleation. In the present simulations, a box of size $100nm \times 50nm \times 25nm$ is used. It consists of about 10 million atoms, the lattice constant of nickel being 3.52 A^o.

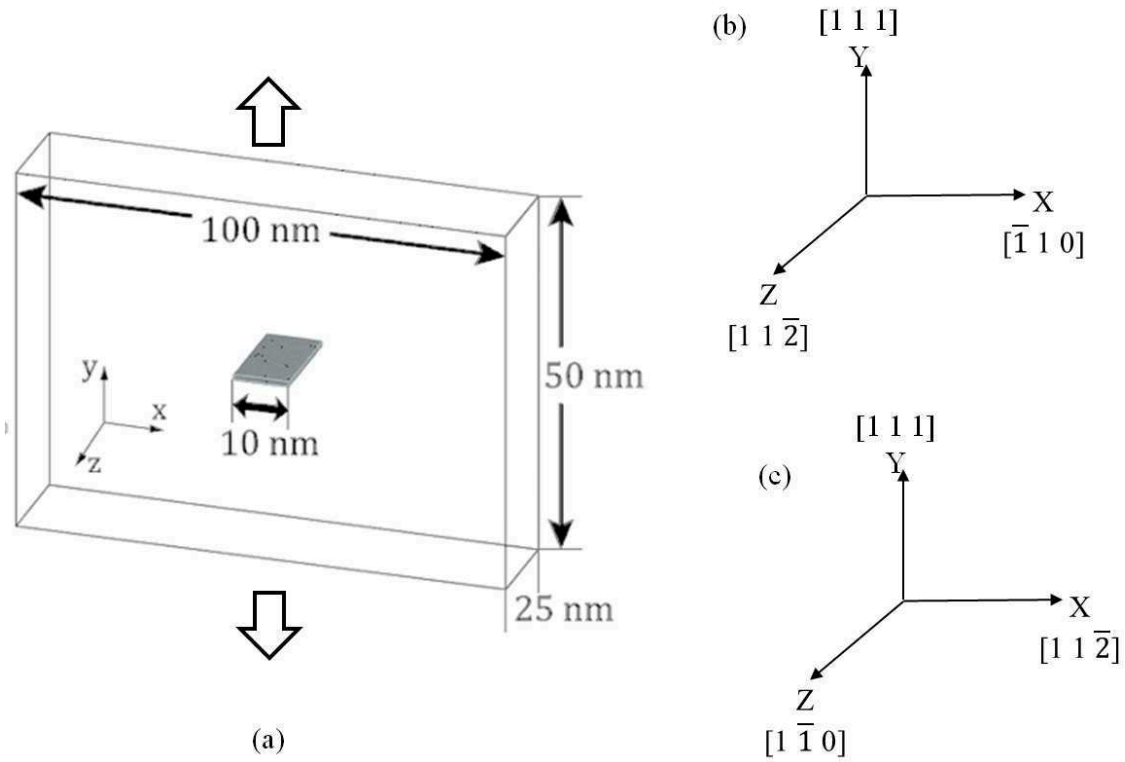

Figure 4.9: Geometric details of the MD model with boundary conditions: (a) physical representation of the specimen with an embedded crack; crystal orientations with respect to specimen coordinate axes for: (b) orientation-1, and (c) orientation-2.

The interaction between nickel atoms in the MD simulations is computed by a many-body potential function, described by the embedded-atom method or EAM developed in [89]. This potential is appropriate for most transition metal systems. The functional form of the EAM potential energy of the $i-th$ atom is given as:

$$E_i = \mathcal{F}_\alpha \left(\sum_{i \neq j} \rho_\beta(r_{ij}) \right) + \frac{1}{2} \sum_{j=1, j \neq i}^{N} \phi_{ij}(r_{ij}) \tag{4.24}$$

The first term is an embedding function that represents the energy required to place an atom i of type α into the electron cloud. The electron cloud density is a summa-

tion over many atoms, usually limited by a cutoff radius. In the embedding energy function $\mathcal{F}_\alpha$, ρ_β is the contribution to the electron charge density from atom j of type β at the location of atom i. It is a function of the distance r_{ij} between atoms i and j within a cutoff distance. The second term is a short-range electrostatic pair-wise potential as a function of the distance r_{ij} between atoms i and j. For a single element system, three scalar functions must be specified, viz. the embedding function, a pair-wise interaction function, and the electron cloud contribution function.

Periodic boundary conditions are applied to eliminate free surface effects. Translational symmetry extends the crack infinitely in the $z-$ direction. The simulation box is subjected to an applied $y-$direction displacement that governs a controlled incremental strain of $\Delta\epsilon$ in equation (4.23). The incremental strain is realized by displacing atoms via affine transformation prior to time integration of the governing equations.

Simulations with the accelerated MD model are used to understand deformation mechanisms at the crack tip and to quantify state variables that govern the plastic deformation, viz. evolution of mobile and immobile dislocation densities, twin volume fraction etc., at strain-rates that are much lower compared to what are achievable in conventional MD. Various methods have been suggested in [16] to extract deformation mechanisms from simulated atomic configurations. The DXA method of extracting

the topological structure of dislocations [50] and the atomic-scale deformation gradient measurement [81] for identifying twinned regions are utilized in this work.

4.4.2 Results of Hyperdynamics MD Simulations

MD simulations are conducted for two different lattice orientations, corresponding to the following directions for the $x-y-z$ axes in figure 4.9(a). They are:

1. Lattice Orientation 1: $x \rightarrow [\bar{1}10]$, $y \rightarrow [111]$, $z \rightarrow [11\bar{2}]$

2. Lattice Orientation 2: $x \rightarrow [11\bar{2}]$, $y \rightarrow [111]$, $z \rightarrow [1\bar{1}0]$

The significance of these two orientations is that the three slip planes $(\bar{1}11)$, $(1\bar{1}1)$ and $(11\bar{1})$ have the same in-plane stresses when the sample is loaded in the $y-$direction, which is the crystallographic [111] direction. In contrast, the (111) plane, being perpendicular to the $y-$-axis, has zero in-plane stresses. Different orientations of the embedded crack with respect to the crystallographic axis leads to the activation of slip in different directions. This in turn leads to the generation of different kinds of dislocations governing plastic behavior.

The two orientations have also been used in [16] with conventional MD, at an applied strain-rate of $2 * 10^7/sec$, to investigate orientation dependence of crack tip plasticity. However, at this high strain-rate, the atomic system does not have enough time for activation of thermal activation-dependent mechanisms. Therefore, the sim-

ulation temperature in [16] was kept to 2K and only stress-driven phenomenon was studied. With the hyperdynamics based accelerated MD in the present study, a strain-rate of $10^4/sec$ is achieved. Hence, both the stress-driven and thermally activated processes can be accurately represented, for which the system temperature is kept at 300K.

4.4.2.1 Results for lattice orientation-1

As mentioned earlier, for lattice orientation-1, three slip planes have the same in-plane stress and the crack tip extends in crystallographic $[11\bar{2}]$ direction. Figure 4.10(a) shows the evolution of macroscopic volume-averaged stress σ_{yy} as a function of the $y-$ direction engineering strain ϵ_{yy}. In the tensile stress-strain curve, the peak stress corresponds to the critical resolved shear stress required for nucleating the dislocation. The stress subsequently decreases due to the motion of dislocation, which releases the elastic strain in the system. The results are for two strain-rates, viz. $2 * 10^7/sec$ with conventional MD and $10^4/sec$ with hyperdynamics. The critical stress, which corresponds to nucleation of first leading partial from the crack tip, are respectively $\sim 4.65GPa$ and $\sim 4.38GPa$ for the strain-rates $2 * 10^7/sec$ and $10^4/sec$. The drop in critical stress is due to the fact that at finite temperatures and lower strain-rate, thermal activation plays a major role in the nucleation process. The evolution of dislocations is also investigated to understand the effect of strain-rate in more detail. Figure 4.10(b) shows the evolution of total, mobile (Shockley partial)

and immobile (stair-rod) dislocation density as the specimen deforms plastically. The dislocation density is approximated as the total dislocation length per unit volume. At a strain-rate of $10^4/sec$, the stabilized mobile dislocation density is almost 50 % higher than that at $2 * 10^7/sec$. Higher mobile dislocation density implies more ductility in the plastic regime. This difference in dislocation density for different strain-rates is due to the fact that at lower strain-rates, the system nucleates a lesser number of dislocations as shown in figure 4.10. This enhances the free path for dislocations to glide before interacting with other dislocations from intersecting slip planes. Contrary to mobile dislocation density, which is much higher at low strain-rate compared to higher rates, the immobile dislocation density is less at lower strain-rates. The difference in immobile dislocation density for the two strain-rates is not so significant. The presence of immobile dislocations hardens the material by making it difficult for mobile dislocations to glide freely. At lower strain-rates, the combined effect of higher mobile dislocation density and lower immobile dislocation density makes the material hardens slowly. This is evident from the reduced flow stress of the material.

4.4.2.2 Results for lattice orientation-2

For the crystal lattice orientation-2, the crack tip extends in crystallographic $[1\bar{1}0]$ direction, which makes the $(11\bar{1})$ plane parallel to the crack tip. In this particular orientation, the $[11\bar{2}]$ direction corresponds to the maximum in-plane stress, which

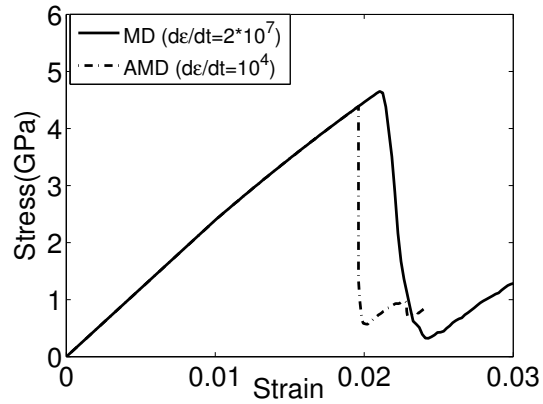

(a)

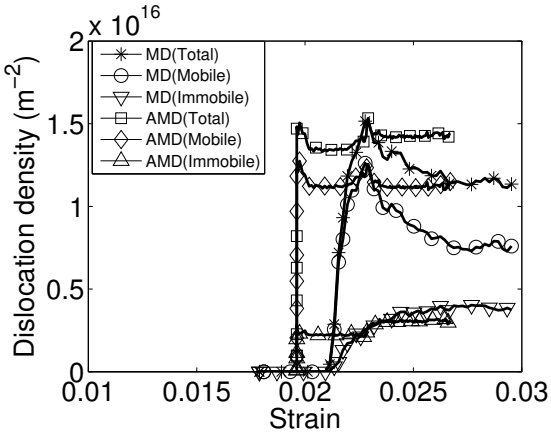

(b)

Evolution of variables for the crystal lattice orientation-1 by conventional MD and accelerated

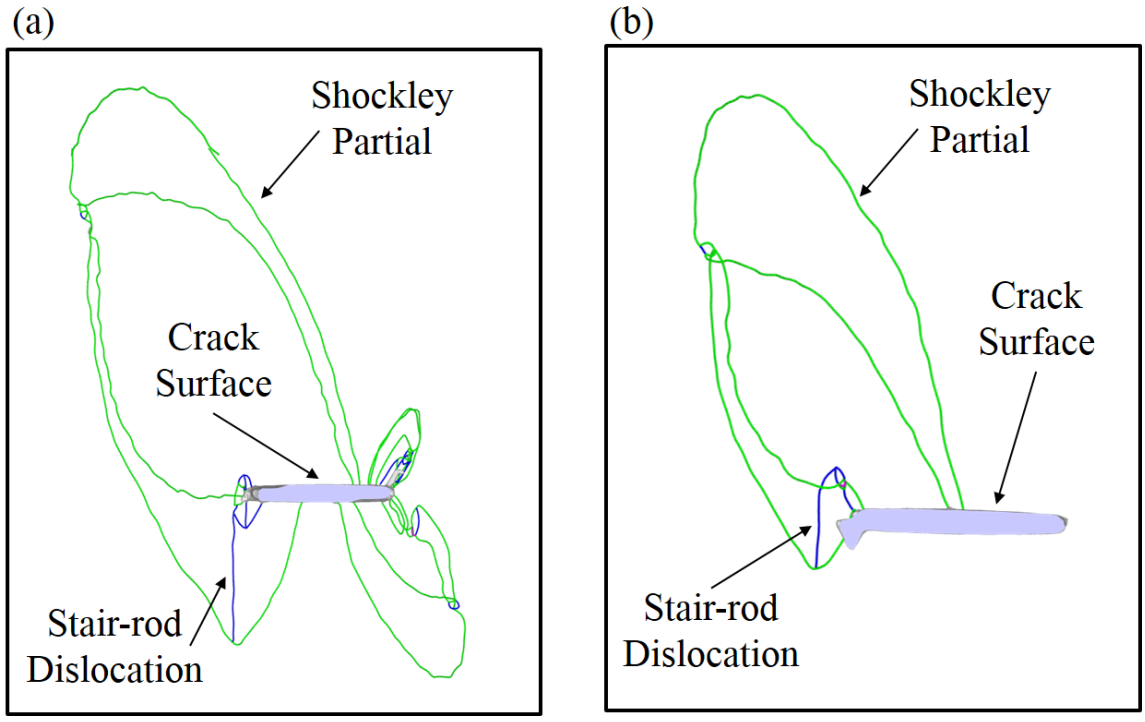

Figure 4.10: Initial crack-tip dislocation segments for orientation-1 at strain-rates of (a) $2 * 10^7/sec$ by conventional MD, and (b) $10^4/sec$ by accelerated MD.

favors nucleation of leading partial dislocations. A leading partial with Burgers vector $b = \frac{1}{6}\ [11\overline{2}]$ is emitted irrespective of the strain-rate as shown in figure 4.12(a). This dislocation is purely edge in character. At the high strain-rate of $2 * 10^7/sec$, this leading partial is followed by another leading partial in an adjacent parallel slip plane as shown in figure 4.12(b). This combination forms a micro-twin band. The twinned region increases by the migration of twin boundaries due to subsequent nucleation of leading partials in parallel slip planes. However for the lower strain-rate of $10^4/sec$, the leading partial is followed by a trailing partial. Together they form a full dislocation as seen in figure 4.12(c). This significant difference in deformation mechanisms is clearly a strain rate-effect. It also has a profound effect on the macroscopic stress-strain response of the material as depicted in figure 4.11. A full dislocation i.e a leading partial followed by a trailing partial in the same slip plane, does not leave behind any stacking fault and once a full dislocation nucleates it carries plastic strain by gliding along the slip plane. On the other hand, for twin, plastic strain is carried by the migration of twin boundary which is accomplished by nucleation of successive leading partial in parallel slip planes. Since the gliding stress is much smaller than the nucleation stress, it makes full dislocation a more superior carrier of the plastic strain away from the crack tip in comparison to the twin, which is also evident from macroscopic stress-strain plot. The present finding is in agreement with [36] where a transition from twin (under short time and high load) to full dislocation (under a long time and smaller load) has also been observed under a fixed applied

stress intensity (K_I). At this point, it is worthy to mention that for present crack orientation and with mode-I loading, nucleation of twin or full dislocation could also depend on the atomic configuration of the crack tip. For some particular crack-tip atomic configuration plastic deformation is dislocation dominated at both low and high applied strain rate. This suggests that to develop an accurate analytic model predicting the critical strain rate corresponding to twin to dislocation transition may need to take local crack tip atomic configuration into consideration.

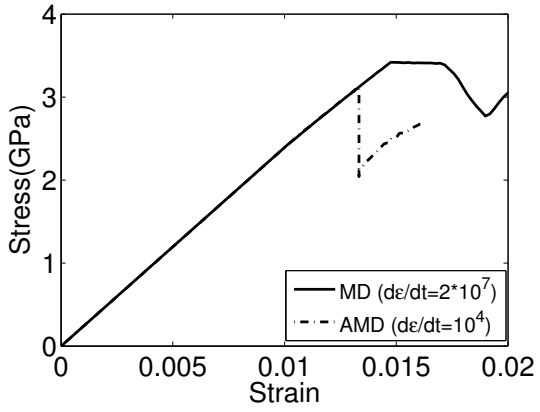

Figure 4.11: Evolution of macroscopic stress as a function of engineering strain for orientation-2 by conventional MD and accelerated MD (AMD).

4.5 Concluding Remarks

In this chapter a strain-boost hyperdynamics based accelerated molecular dynamics framework has been developed for modeling deformation in crystalline materials with an embedded crack. MD simulations are capable of depicting evolving deformation mechanisms in materials at the atomic scale. The method has been used for

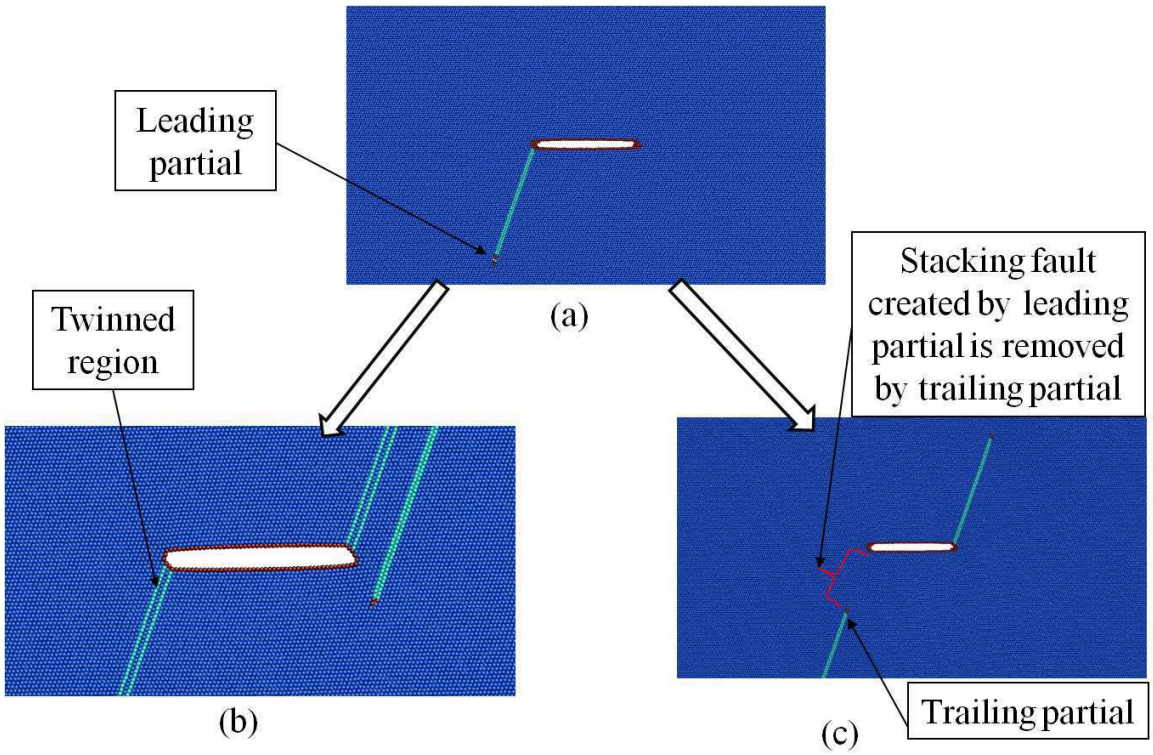

Figure 4.12: Snapshots of plastically deformed atomic configuration in orientation-2, ploted using AtomEye [6] with color based on common neighbor analysis (CNA [7]), showing deformation mechanisms at different strain-rates: (a) leading partial nucleation at the onset of plasticity irrespective of strain rate; (b) leading partial followed by another leading partial in the parallel slip plane (twining partial) at high strain-rates, and (c) leading partial is followed by a trailing partial at lower strain-rates.

continuum-scale material property assessment by hierarchical and concurrent coupling with continuum models. A major limitation of such coupling with conventional MD simulations is that very small MD time-scales restrict the achievable strain-rates to be much higher than experimentally observed rates, needed for continuum scale modeling, e.g. using crystal plasticity finite element methods. An approach that has been used to extract low strain-rates by simple extrapolation of the higher strain-rate results. While this approach may be reasonable when the deformation mecha-

nisms remain unchanged over long temporal domains, their predictive capabilities are severely compromised in the presence of multiple competing mechanisms, whose activation depends on the deformation rate itself. Furthermore, in a concurrent coupling of MD with continuum models, stability requirements of the integration algorithm can adversely affect time increments in the continuum model. The hyperdynamics accelerated MD tool that is adopted and developed here is demonstrated to overcome these limitations and achieve experimentally observed strain rates. This method is incorporated in the LAMMPS code and validated for an atomistic model of a single crystal nickel specimen. Excellent agreement is achieved with high strain-boost over conventional MD. High effectiveness is achieved for the low frequency of events of interest that makes the achievable boost to be dependent on the temperature. Strain rates of the order of 10^4 are simulated with this method with an exponential increase in the achievable boost with decreasing strain-rates.

Numerical studies are subsequently conducted for a single crystal nickel material with an embedded crack. In contrast to observations at high strain-rates of the order of $\sim 10^7$ in [16], this study is intended to characterize evolving mechanisms at lower strain rates, e.g. $\sim 10^4$. MD simulations are conducted for two different lattice orientations or Schmid factors. Different orientations of the embedded crack with respect to the crystallographic axis lead to slip activation in different directions causing nucleation of different kinds of dislocations. For the first orientation, the mobile dislocation

density remains nearly constant with a periodic burst of dislocations. This is a typical feature of plastic deformation in single crystals, as has been observed for aluminum single crystals in [90]. For the second orientation, the plastic deformation mechanism is dislocation dominated for the lower strain-rate, as opposed to twin dominated prediction at high strain-rate with conventional MD. This observation is also consistent with the experimental observation that Nickel shows deformation twinning only under shock loading at low temperatures [91, 92]. In summary, the present study shows that the strain-boost hyperdynamics is an effective method to overcome the time scale limitation of conventional MD for continuum modeling of elastic-plastic phenomena. Such methods are important for lower strain-rate, coupled continuum-atomistic simulation methods that exhibit multiple time-scales in the disparate domains. In the next chapter 5 the strain-boost hyperdynamics is used to develop a time matching framework to match the time scale in the Atomistic-Continuum concurrent coupled model.

Chapter 5

Bridging the Time Scale Between the Atomistic and the Continuum Model

For atomistic-continuum coupled models, the time scale mismatch between the atomistic and the continuum domain renders the two domains to experience a different rate of deformation. This is due to the requirement of a small incremental time step in the molecular dynamics ($\Delta t_{MD} = 1 femto - sec$)for the stability of the velocity-verlet time integration scheme. For this reason the rate of applied loading has to significantly high ($\dot{\epsilon} = 1.0e^{8}$) [93, 15, 14]. To circumvent this time-scale mismatch, strain-boost hyperdynamics [37, 47] based time acceleration is incorporated within the concurrent framework of the atomistic-continuum coupled model [25]. In this chapter, a novel

time marching algorithm is discussed. The same time marching scheme will be used to match the time scale between the atomistic and the continuum domain. The

5.1 Coupled Accelerated Time Marching Algorithm

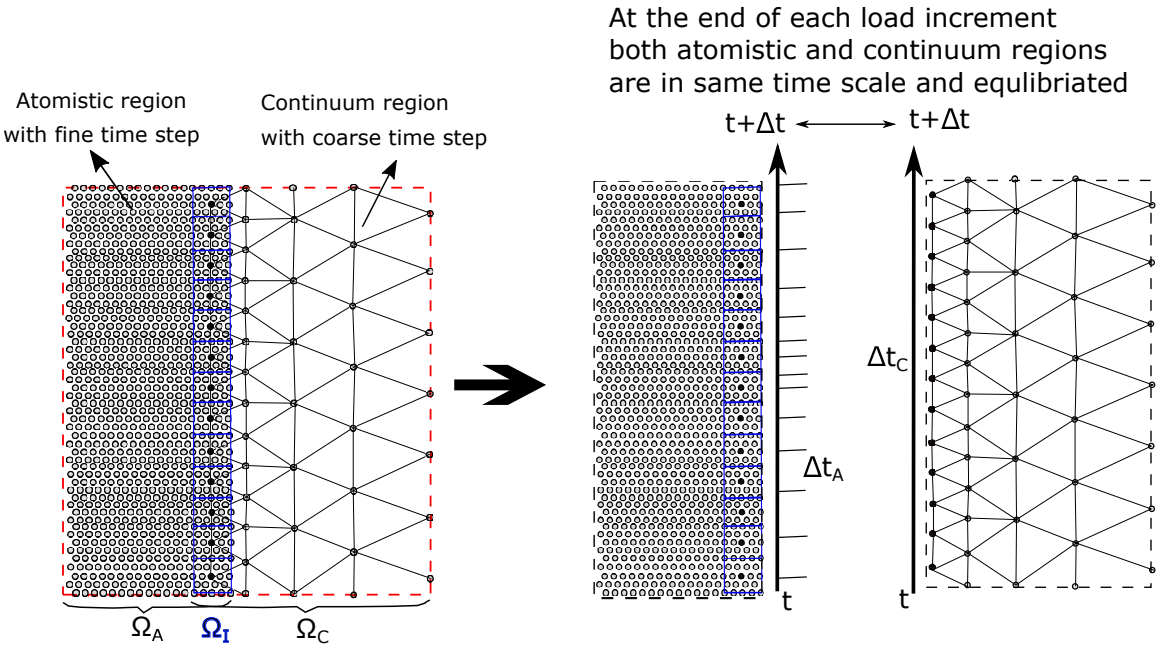

Figure 5.1: Time marching scheme for the concurrent coupled model, where the time of atomistic simulation is determined by the strain-boost hyperdynamics. A slower time evolution indicates that the system is very close to an infrequent event to occur.

The strain-boost hyperdynamics-based time marching scheme is applied to the coupled concurrent model to make both the continuum and atomistic domains evolve at similar time-scales with comparable strain-rates. The method has been successfully implemented in the LAMMPS code [38] as described in [47] to accelerate the occur-

rence of infrequent events in the atomistic domain and achieve a time-scale match between the discrepant domains of the concurrent model. A schematic representation of the proposed time marching scheme is shown in figure 5.1. Let Δt_C^i be the time increment in the continuum domain Ω_C corresponding to an incremental load $\{\Delta \boldsymbol{f}_{\text{ext}}^C\}$ of equation (2.11) in the $i-$th load step. For each load increment, the equilibrated continuum and atomistic configurations are obtained by solving equations (2.13) and (2.30) respectively using a staggered iterative approach. In each iteration, the equilibrium equations (2.13) is solved for Ω_C first. This is followed by dynamic relaxation of the atomistic domain using equation (2.30) for a predetermined number of MD steps. At the end of each coupled iteration loop, the solution is checked for convergence using equation (5.8). The time-scale match between the continuum and atomistic domains is also verified against the criterion, expressed as:

$$\sum_{N_{MD}} \Delta t_A^j = \Delta t_C^i \tag{5.1}$$

where N_{MD} is the total number of MD steps for each coupled iteration step. Δt_A^j is the physical time elapsed for the atomic system in the j^{th} MD step. This is given by equation (4.3) as:

$$\Delta t_A^j = \Delta t_{MD} exp \frac{\left[\Delta V_b\right]_j}{K_b T} \tag{5.2}$$

where Δt_{MD} is the incremental time-step in MD used for atomic position update by integrating equation (2.30) using the velocity-Verlet algorithm [88]. A time step of

$\Delta t_{MD} = 0.002ps$ is used for the present study. The boost factor obtained for the $j-$th MD step due to the applied boost potential of ΔV_b is $\exp\left(\frac{\left[\Delta V_b\right]_j}{K_b T}\right)$. Successive iteration continues until convergence in the displacement solution of interface nodes and the time matching criterion are satisfied. It is noteworthy that equation (5.1) guarantees that at the end of each successful load increment, the total time evolution in both the continuum and atomistic domains are the same. This in turn makes both domains evolve at the same strain-rate.

5.2 Solution Steps in the Coupled Concurrent Problem

A staggered-iterative approach is used to solve the governing equations of the coupled atomistic-continuum system. Problems in Ω_C and Ω_A are solved in each iteration, subject to displacement and force constraints in the interface handshake domain Ω_I. Ghost forces at the free surface of the atomistic domain are mitigated by using a dead load correction method proposed in [23]. The strain-boost hyperdynamics method has been implemented in LAMMPS code [38] for MD simulations as an additional module as detailed in [47]. Finite element analysis of the continuum domain is conducted with a finite deformation crystal elasticity code. Nonlinearity in the constitutive relation is expected due to the non-harmonic nature of the interatomic interaction.

For the present study, the most critical region is in the vicinity of the crack-tip is boosted. As shown in figure 5.2, only a cylindrical region of radius $15A^o$ surrounding the crack tip is boosted at the start of the analysis. Additional atoms are adaptively added to this group as the crack evolves, depending on the current crack-tip location. Common Neighbor Analysis(CNA) is used to identify the new location of the crack tip and the atoms around it. CNA is a good indicator to assess the local crystal structure of an atomic system. In LAMMPS, it is possible to identify five kinds of CNA patterns viz. fcc=1, hcp=2, bcc=3, icosahedral=4, unknown=5. The atoms forming the crack surface and crack tip are characterized by CNA=5. Hence CNA value of all atoms is evaluated periodically and any new atoms that have a CNA value of 5 are identified. Those particular atoms along with their first and second nearest neighbors are tagged as 'to be boosted'. Since a deficient near-neighbor count invalidates the least-square minimization-based local atomic strain, atoms with less than 12 first-nearest-neighbors for FCC crystals are not boosted in the present study.

5.2.1 Anisotropic Elastic Constitutive Model for the Continuum Domain Ω_c

A nonlinear anisotropic elasticity model has been developed in [1, 2] for the bulk crystalline material without any cracks, by homogenizing the atomistic response. The

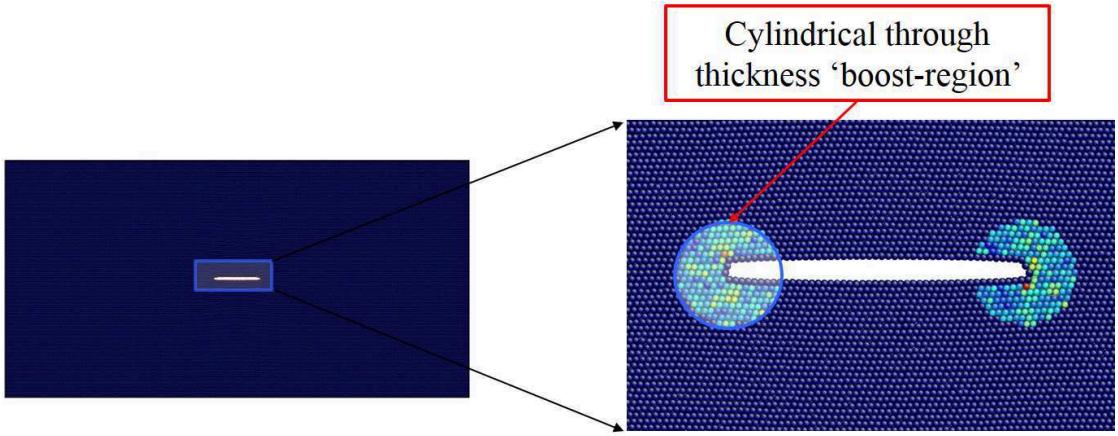

Figure 5.2: (a) The 3D computational domain for the concurrent simulation with a crack embedded in it, and (b) expanded view of the crack-tip boost region. Atom color represents the value of the second invariant of the atomic strain (η_i^{Mises}) at 1% macroscopic strain. AtomEye [6] is used for visualization of the atomistic domain.

stress-strain relation $\sigma_{ij} = \frac{\partial \omega(\boldsymbol{\epsilon})}{\partial e_{ij}}$ is derived from a third-order strain dependent strain energy density function, expressed as:

$$\omega(\boldsymbol{\epsilon}) = \frac{1}{2!} c_{ijkl} \epsilon_{ij} \epsilon_{kl} + \frac{1}{3!} c_{ijklmn} \epsilon_{ij} \epsilon_{kl} \epsilon_{mn} \tag{5.3}$$

The first term in equation (5.3) is related to the harmonic part of the EAM potential, while the second term comes from its non-harmonic part. Accounting for the crystal symmetry groups for cubic single crystals (pure nickel is studied here), the coefficients in equation (5.3) are reduced to only 3 independent coefficients for the first-order terms and 6 independent coefficients for the second order terms. Using contracted notations i.e. subscripts $11 \mapsto 1$, $22 \mapsto 2$, $33 \mapsto 3$, $23 \mapsto 4$, $31 \mapsto 5$ and $12 \mapsto 6$, the independent stiffness coefficients are reduced to c_{11}, c_{12}, c_{44}, c_{111}, c_{112}, c_{123}, c_{144}, c_{166}

and c_{456}. The strain energy density function in equation (5.3) thus reduces to:

$$\begin{aligned}\omega(\boldsymbol{\epsilon}) =& \frac{1}{2}c_{11}(\epsilon_1^2+\epsilon_2^2+\epsilon_3^2) + c_{12}(\epsilon_1\epsilon_2+\epsilon_2\epsilon_3+\epsilon_3\epsilon_1) \\ &+ \frac{1}{2}c_{44}(\epsilon_4^2+\epsilon_5^2+\epsilon_6^2) + \frac{1}{6}c_{111}(\epsilon_1^3+\epsilon_2^3+\epsilon_3^3) \\ &+ \frac{1}{2}c_{112}\big(\epsilon_1^2(\epsilon_2+\epsilon_3)+\epsilon_2^2(\epsilon_3+\epsilon_1)+\epsilon_3^2(\epsilon_1+\epsilon_2)\big) \\ &+ c_{123}\epsilon_1\epsilon_2\epsilon_3 + \frac{1}{2}c_{144}(\epsilon_1\epsilon_4^2+\epsilon_2\epsilon_5^2+\epsilon_3\epsilon_6^2) \\ &+ \frac{1}{2}c_{166}\big(\epsilon_1(\epsilon_5^2+\epsilon_6^2)+\epsilon_2(\epsilon_6^2+\epsilon_4^2)+\epsilon_3(\epsilon_4^2+\epsilon_5^2)\big) + c_{456}\epsilon_4\epsilon_5\epsilon_6\end{aligned} \tag{5.4}$$

The 9 elastic coefficients are calibrated from MD simulations of an uncracked nickel specimen under bi-axial tension loading in [1], as given in table 5.1. This elastic

Coefficient	c_{11}	c_{12}	c_{44}	c_{111}	c_{112}	c_{123}	c_{144}	c_{166}	c_{456}
Calibrated Values	244.6	150.8	125.1	-1660	-1220	-250	-130	-510	-65

Table 5.1: Three first order and six second order elastic stiffness coefficients (unit:GPa) of nickel single crystal calibrated in [1, 2].

model is used for the continuum domain in the concurrent model.

5.2.2 Setting up the Initial Configuration of the Atomistic Domain (Ω_A)

Prior to setting up the concurrent model, the entire simulation domain i.e. $\Omega_T = \Omega_C \bigcup \Omega_A \backslash \Omega_I$ is set up as an atomistic domain, with the atomic configurations conforming to the crystallographic lattice structure of the material being interrogated.

Energy minimization is subsequently carried out under conditions of molecular statics to obtain the initial equilibrated configuration. Next, atoms in the continuum domain $\Omega_C \backslash \Omega_I$ are removed and a finite element model and mesh is created in Ω_C. Removal of atoms from Ω_C creates a free surface at the boundary of Ω_A that can result in force imbalance. A ghost force correction process is executed to mitigate this free surface effect at the interface. The correction forces are computed from those on surface atoms before and after replacing atoms with the continuum mesh in the relaxed initial configuration as:

$$\boldsymbol{f}_{\boldsymbol{p}}^{\boldsymbol{G}} = \tilde{\boldsymbol{f}}_{\boldsymbol{p}} - \boldsymbol{f}_{\boldsymbol{p}} \tag{5.5}$$

where $\boldsymbol{f_p}$ is the force on atom p with full atomic representation and $\tilde{\boldsymbol{f}}_{\boldsymbol{p}}$ is the force after replacing certain atoms with the continuum mesh. A correction force $\boldsymbol{f}_{\boldsymbol{p}}^{\boldsymbol{G}}$ is imposed on atom p as an additional external force to annul the ghost force.

In the interface region Ω_I, where both the MD and FE models overlap, the atom-node connection is built using 3D Voronoi tessellation discussed in [39]. Finally, a sharp crack is introduced in the MD domain by identifying atoms on two sides of the crack-plane and turning off the interaction between them.

5.2.3 Steps in Each Load Increment

For each load increment, an iterative solution process is conducted to find the MD-FE solution fields. Evaluation of variables at the $(k+1)-th$ iteration step proceeds with known displacement fields $\Delta \boldsymbol{U}^C(t)$ and $\Delta \boldsymbol{U}^A(t)$ at the iteration step $k \geq 1$ using the following steps.

I. Displacement increments in Ω_C: In this step, FE analysis in Ω_C is conducted with known boundary conditions on the external boundary $\partial\Omega_C^{ext}$. The incremental load or displacement on the external boundary $\partial\Omega_C^{ext}$ is held fixed for the time increment Δt, while the concurrent problem is iteratively solved. In each iteration step from $k \rightarrow k+1$, applied displacements on a FE node β in the handshake domain Ω_{C_I} is updated from the aggregated atomic displacement vector $\Delta \boldsymbol{U}^{A_I}$ in Ω_{A_I}. From equation (2.6), the latter is specified in terms of atomic displacements in the previous iteration k, as:

$$\{\Delta \boldsymbol{U}^{C_I}\}^{k+1} = \{\Delta \boldsymbol{U}^{A_I}\}^{k} = \sum_{p \in G_\beta} w_p \cdot \Delta\{\boldsymbol{U}_p^A\}^k \tag{5.6}$$

Subsequently, the FE problem is solved in Ω_C for the updated nodal displacements $\{\Delta \boldsymbol{U}^C\}^{k+1}$.

II. Constraint forces on Ω_{A_I} *from* Ω_{C_I}: Upon evaluation of the vector of Lagrangian multipliers $\{\boldsymbol{\lambda}\}^{k+1} = \{\boldsymbol{\lambda}\}^k + \{\boldsymbol{\Delta\lambda}\}^{k+1}$ for all interface nodes, the constraint forces

on atoms in Ω_{A_I} are evaluated using equation (2.8) as:

$$\{\boldsymbol{f}_p^{\text{constraint}}\}^{k+1} = \begin{cases} w_p\{\boldsymbol{\lambda}_\beta\}^{k+1} & \forall p \in G_\beta \in \Omega_{A_I} \\ 0 & \forall p \in \Omega_A \backslash \Omega_{A_I} \end{cases} \tag{5.7}$$

III. MD simulations in Ω_A with constraint forces at the interface: The constraint forces evaluated in step II are applied to the interface atoms Ω_{A_I}. Hyperdynamics accelerated MD simulations are conducted over a predetermined time period using the velocity Verlet time integration algorithm [88].

IV. Transfer of displacements from Ω_A to Ω_C: With the updated atomic displacements from step III, $\{\Delta \boldsymbol{U}^{A_I}\}^{k+1}$ is calculated using the right-hand part of equation (5.6). These displacements are used as boundary conditions of the interface FE nodes in the next iteration.

At the end of step IV, the displacement error for all nodes in the handshake region Ω_I is evaluated for convergence. For the $k-th$ iteration, the displacement error is evaluated against a tolerance ϵ_u as:

$$\left|\boldsymbol{\Delta} U^{C_I} - \boldsymbol{\Delta} U^{A_I}\right|_{max} \leq \epsilon_u \quad \in \ \Omega_I \tag{5.8}$$

where $|.|_{max}$ is the maximum value of the Euclidean norm. The tolerance ϵ_u is taken to be 0.1 Å in this work. For each interface node β, the atomic displacement vector is aggregated as $\{\boldsymbol{\Delta} U_\beta^{A_I}\} = \sum_{i=1}^{N_\beta} \frac{1}{N_\beta}.\Delta\{\boldsymbol{U}_p^A\}$, where N_β is the number of atoms in the Voronoi cell G_β associated with a FE node β and $\boldsymbol{U}_p^A$ is the displacement of an atom p in $G_\beta \in \Omega_A$. For each load increment on $\partial\Omega_C$, these four steps are iteratively executed till the displacement solution converges in equation (5.8) and a time-match is achieved between the domains according to equation (5.1). The time-match criterion is a dominant factor in determining the number of iteration steps.

5.3 Validation of the Hyperdynamics Accelerated Concurrent Model

Prior to its use in the investigation of crack propagation, the strain-boost hyperdynamics accelerated coupled atomistic-continuum model is validated with a regular model where conventional MD simulations are performed without any time acceleration. The concurrent computational domain, its geometry and loading conditions for the simulation problem are shown in figure 5.3. The material modeled is crystalline pure nickel with overall specimen dimensions of 200 nm × 200 nm × 4.22 nm. A through thickness crack in the xz-plane of initial length $2a_0 = 20$ nm is embedded in the specimen, as shown in figure 5.3(a). The atomistic domain Ω_A is a cylindrical region of radius $R_A = 32$ nm and the interface region Ω_I is an annular ring with

inner and outer radii of 28 nm and 32 nm respectively. The atomistic domain contains about 1.3 million nickel atoms with FCC lattice structure. The lattice constant of nickel is 3.52Å. The lattice orientation with respect to global axis is $x \rightarrow [100]$, $y \rightarrow [010]$ and $z \rightarrow [001]$. This specific crystal orientation is chosen to facilitate crack propagation due to bond cleavage. The center crack is manifested by turning off the interaction between the atoms on both side of the crack plane. The rest of the domain is considered as continuum and discretized into a finite element mesh containing approximately $5,000$ nodes and $20,000$ 4-noded constant strain tetrahedral elements as shown in figure 5.3(b).

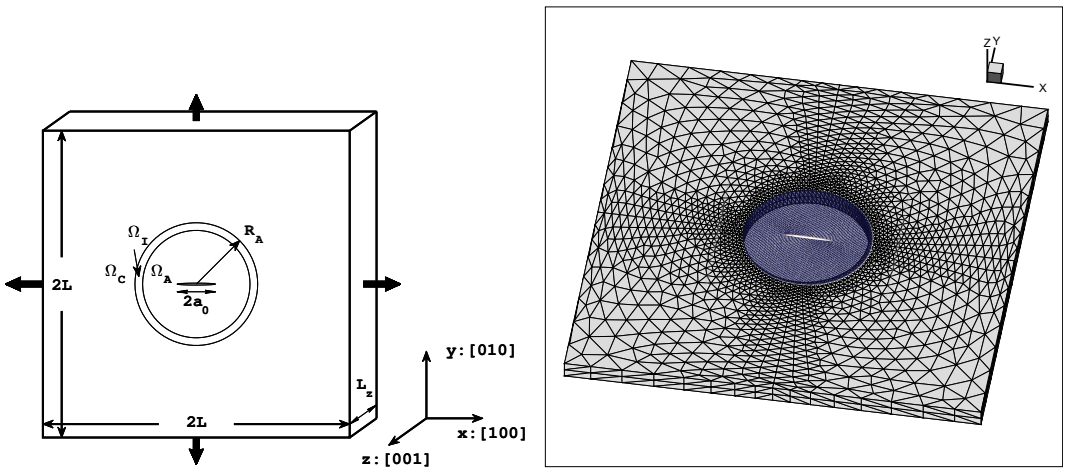

(a) (b)

Figure 5.3: Computational specimen modeled by the concurrent atomistic-continuum model for crack propagation, (a) geometry and dimensions of the specimen with loading, and (b) discretization of the continuum and atomistic domains.

The simulations begin with initial energy minimization and relaxation of the atomic configuration. Subsequently, a controlled bi-axial displacement loading is

applied on the specimen in the x and y directions at a constant strain-rate of $\dot{\epsilon} = 1.0 \times 10^7 \text{s}^{-1}$. The z-faces are stress free, i.e. $\sigma_{33} = 0$. The NVE ensemble is used for MD simulations, where a Langevin thermostat is used to maintain the atomistic domain temperature at $300K$. The kinetics and energetics of crack propagation in the form of crack propagation rate and strain energy release are compared for the hyperdynamics-accelerated and conventional models.

The mode-I stress intensity factor (SIF) K_I for a square plate with a central crack is approximated as [94, 95],

$$K_I = \sigma\sqrt{\pi a}.\eta \tag{5.9}$$

where σ is a far field stress on the external boundary of the continuum domain. It is computed as $\sigma_{yy} = \frac{F_y}{A_{xz}}$, where F_y is the y-component of total reaction of all nodes, on which displacement controlled loading is applied. The geometric factor η compensates for the finite specimen dimensions in this study, as opposed to the infinite dimensions considered in its derivation. A polynomial form of η has been given as [96, 95]:

$$\eta = sec\left(\frac{\pi a}{2L}\right)^{1/2}\left[1 - 0.025\left(\frac{a}{L}\right)^2 + 0.06\left(\frac{a}{L}\right)^4\right] \tag{5.10}$$

where a is the crack length and L is the characteristic dimension of the specimen as shown in figure 5.3(a). The crack propagation rates ($v = \frac{da}{dt}$) by the hyperdynamics-accelerated and conventional MD simulations in the concurrent model are plotted as

a function of the applied stress intensity factor K_I in figure 5.4(a). The propagation rates generally agree very well, with very small deviation at the later stages of crack propagation. For a quantitative correlation, the data is fitted with a crack propagation rate formula proposed in [2]:

$$v = \dot{a} = \begin{cases} c \cdot (K_I - K_{IC})^{1/2}, & \text{if } K_I > K_{IC} \\ 0, & \text{otherwise} \end{cases} \tag{5.11}$$

where K_{IC} is the critical stress intensity factor (with the unit $\text{MPa} \cdot \sqrt{\text{m}}$) and c is a coefficient (with the unit $\text{Pa}^{-0.5}\text{m}^{3/4}\text{s}^{-1}$) that is a measure how fast or slow the propagation-rate changes with crack propagation. The (K_{IC})s for the crack to propagate in the hyperdynamics-accelerated and conventional MD-based concurrent models are calculated to be respectively 0.81 and 0.815.

To compare the energetics of crack propagation, the strain energy release rates in the hyperdynamics-accelerated and conventional MD-based concurrent models are plotted as a function of the crack length in figure 5.4(b). Here the strain energy release rate is computed as $\frac{dU}{da}$, where dU is the change in the total strain energy of the system and da is the increment of the crack length. dU includes the change in elastic strain energy of the continuum domain and the change in the total system potential of the atomistic domain. Results by the two models show excellent agreement. The

initially high strain energy release rates decay with increasing crack length. This agreement justifies the use of the strain-boost hyperdynamics-based MD simulations in the concurrent model for studying material response at lower strain rates.

The computational efficiency of the strain-boost hyperdynamics (HD) accelerated atomistic-continuum concurrent model is compared with the sub-stepping (SS) enabled concurrent model of [1, 2] in table 5.2. Both the FE and LAMMPS codes are parallelized using the message passing interface (MPI) for multi-processor computing. The distribution of the processors between the continuum and atomistic domains is chosen for optimal efficiency. The comparison is made for two different overall strain-rates, viz. $\dot{\epsilon} = 10^7\ s^{-1}$ and $\dot{\epsilon} = 10^4\ s^{-1}$. The computational cost is estimated in terms of CPU-hours on a Bluecrab cluster at Maryland Advanced Research Computing Center (MARCC) using 100 CPU's. The efficiency factor is defined as the ratio of the CPU-hours for the sub-stepping (SS) enabled simulations to the CPU-hours for the hyperdynamics (HD) accelerated simulations, i.e. $\frac{\text{CPU-hr}_{SS}}{\text{CPU-hr}_{HD}} \times 100\%$. Since it is extremely computing intensive to attain a strain-rate of 10^4 using the sub-stepping enabled concurrent model, extrapolation is used to estimate of the computational cost that would have been needed to reaching this rate. The values in table 5.2 imply significant efficiency gain with the hyperdynamics acceleration, especially as the strain-rate reduces.

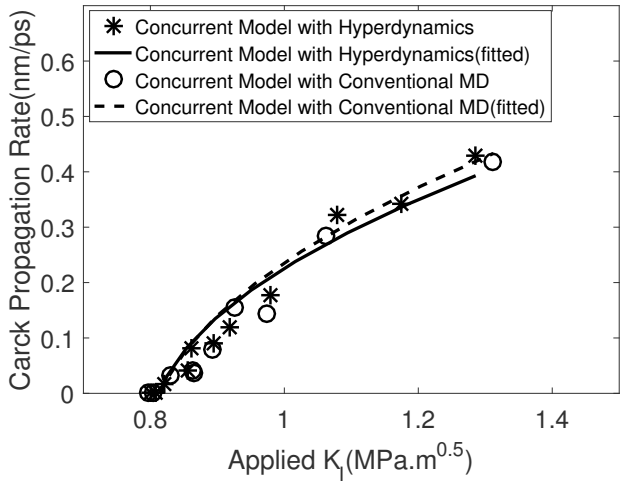

(a)

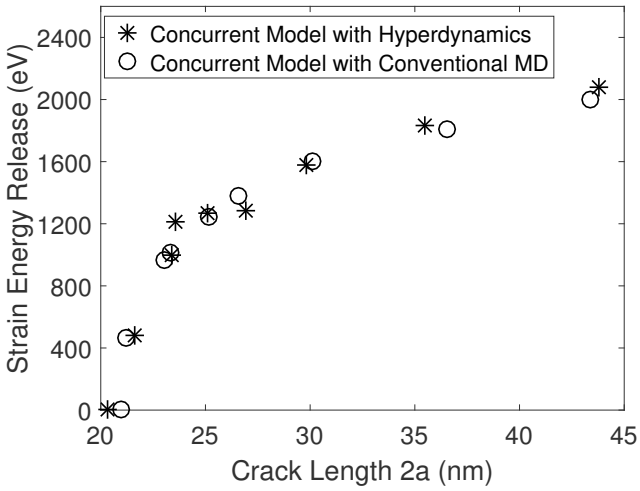

(b)

Figure 5.4: Comparison of results by the concurrent model with and without hyperdynamics-accelerated MD for an applied strain-rate $\dot{\epsilon} = 10^{07}$: (a) rate of crack propagation as a function of SIF, and (b) strain energy release rate as a function of crack length.

5.4 Conclusions

This chapter has successfully developed a coupled concurrent atomistic-continuum multiscale model with an effective temporal acceleration method for bridging the

Strain Rate	CPU Hours for Modeling with		Efficiency Factor
	Sub-stepping	Hyperdynamics	
$\dot{\epsilon} = 10^7\ s^{-1}$	500	65	7.69
$\dot{\epsilon} = 10^4\ s^{-1}$	75000*	350	214.2

Table 5.2: A comparative study of the computational cost (expressed in CPU-hours) by hyperdynamics and sub-stepping accelerated MD models at different strain-rates ($\dot{\epsilon}$). (* computed by extrapolation)

atomistic and the continuum time-scales. The concurrent model incorporates a domain of atomistic simulation that is conducted by molecular dynamics (MD) using the LAMMPS code, a continuum domain of nonlinear anisotropic elasticity for finite element analysis of crystalline materials, and an interfacial handshake region. The strain-boost hyperdynamics model is incorporated in a parallel version of the LAMMPS code to accelerate the time-scale of MD simulation by accelerating the occurrence of infrequent events in the atomistic domain. In a concurrent setting, this allows the MD model to attain the lower strain-rates of the continuum model. The interfacial handshake region of the concurrent model enforces geometric compatibility and force equilibrium between the atomistic and continuum models. The resulting multiscale model can perform atomistic-continuum simulations at length scale that are much larger and time-scales that are much longer than what can be achieved in pure atomistic simulations alone. On account of the time acceleration, thermally activated deformation mechanisms can be captured accurately. This is important for depicting the continuum behavior of the material.

No spurious effects, such as oscillations are observed in the hyperdynamics accelerated concurrent multiscale model. This is validated by comparing the energetics and kinetics of crack propagation with other time-averaging methods in MD, such as the sub-stepping induced MD methods, at a strain-rate of $10^7\ s^{-1}$. The comparison at this strain-rate shows satisfactory agreement and accuracy of the hyperdynamics accelerated concurrent multiscale model. This strain-rate of $10^7\ s^{-1}$ is approximately a lower limit for conventional MD simulation of large atomic systems. However, while the lowest strain-rate studied with the hyperdynamics accelerated concurrent multiscale model is $10^4\ s^{-1}$ in this work, the lower limit can be pushed further to lower strain-rates.

Chapter 6

Extracting the Crack Propagation Law Using the Concurrent Model during Brittle Fracture

The time accelerated concurrent model developed in the previous several chapters can be used to extract some crucial continuum scale evolution laws. These atomically informed evolution laws can be used in full continuum scale simulation for better representation of the material behavior. This chapter discusses one such application of the concurrent model to extract the crack propagation law during brittle fracture.

6.1 Crack Propagation Simulations at Lower Strain-Rates

The hyperdynamics-based concurrent atomistic-continuum model is used to study crack propagation at strain-rates that are lower than what can be typically achieved by conventional MD without time-acceleration. Two studies are considered in this section. The first investigates the effects of strain-rate on parameters in the finite temperature crack propagation-rate of equation (5.11). The second study is intended to establish phase-field models of crack propagation from the concurrent model.

The material specification, specimen geometry and the crystal lattice orientation with respect to specimen geometry ($x \rightarrow [100]$, $y \rightarrow [010]$ and $z \rightarrow [001]$) are given in section 5.3. This crack-crystal orientation combination enables preferential crack propagation over crack-tip dislocation emission for bi-axial loading. This allows the crack orientation to remain unchanged with respect to the crystal axis. Periodicity boundary condition is imposed in the z-direction for the atomistic domain. The NVE ensemble with Langevin thermostat maintains the desired temperature in the atomistic region.

The FE model for the continuum domain uses a mesh of 20273, 4-noded constant strain tetrahedral elements containing 5254 nodes. The nonlinear crystal elastic-

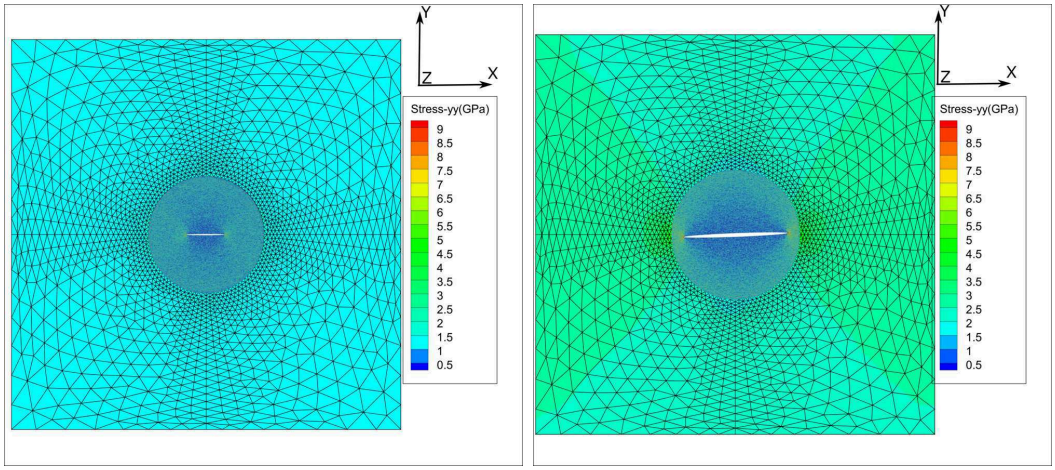

(a) (b)

Figure 6.1: Contour plot of σ_{yy} showing crack advance for volume-averaged strains: (a) $\epsilon_{11} = \epsilon_{22} \approx 1.0\%$, (b) $\epsilon_{11} = \epsilon_{22} \approx 3.3\%$. Stress in the atomistic region corresponds to the per-atom virial stress.

ity constitutive model described in section 5.2 is used for the constitutive response. While a strain gradient-based non-local constitutive relation has been developed for a cracked domain in [2], this contribution is found to be insignificant for studies in this work, as evidenced from the very small calibrated length-scale parameter of ($l^2 \approx 0.25$Å).

Figure 6.1 shows snapshots of the crack before and after growth for volume-averaged strains $\epsilon_{11} = \epsilon_{22} \approx 1.0\%$ and $\epsilon_{11} = \epsilon_{22} \approx 3.3\%$. The crack starts to propagate symmetrically with respect to the y-axis along the original crack surface, once a critical SIF ($K_{IC} = 0.81$ MPa $\cdot \sqrt{\text{m}}$) is exceeded. The crack orientation and thin sample geometry favor crack propagation over dislocation nucleation from the crack tip. Since plasticity is not considered in study, the simulation is terminated

once dislocations nucleate at later stages of crack evolution.

6.1.1 Effect of Strain-Rate and Temperature on the Crack Propagation-Rate

In [47] the authors have shown that deformation mechanisms can differ significantly with strain-rate for certain crack orientations. This results in considerable difference in the overall kinetic and energetic response of the material. To study the effect of strain-rate, simulations are conducted for three strain-rates, viz. $\dot{\epsilon} = 10^7\ s^{-1}$, $10^6\ s^{-1}$, and $10^4\ s^{-1}$ by the hyperdynamics-accelerated concurrent model. Figures 6.2(a), 6.2(b) and 6.2(c) depict the crack propagation-rate as a function of the stress intensity factor (SIF) for the three strain-rates. The parameters K_{IC} and c in equation (5.11) are calibrated from these responses and compared for the three strain-rates in table 6.1.

Strain Rate $\dot{\epsilon}$ (s^{-1})	K_{IC} $(MPa.\sqrt{m})$	c $(MPa^{-0.5}.m^{\frac{3}{4}}.s^{-1})$
10^7	0.823	0.655
10^6	0.813	0.634
10^4	0.805	0.577

Table 6.1: Calibrated values of the crack propagation parameters in equation (5.11) from simulations with the concurrent model at different strain-rates.

The corresponding functional forms in equation (5.11) with the calibrated parameters are plotted in figures 6.2. Crack propagation is observed for all three strain-rates, implying that deformation in the atomistic region is driven by bond cleavage. The

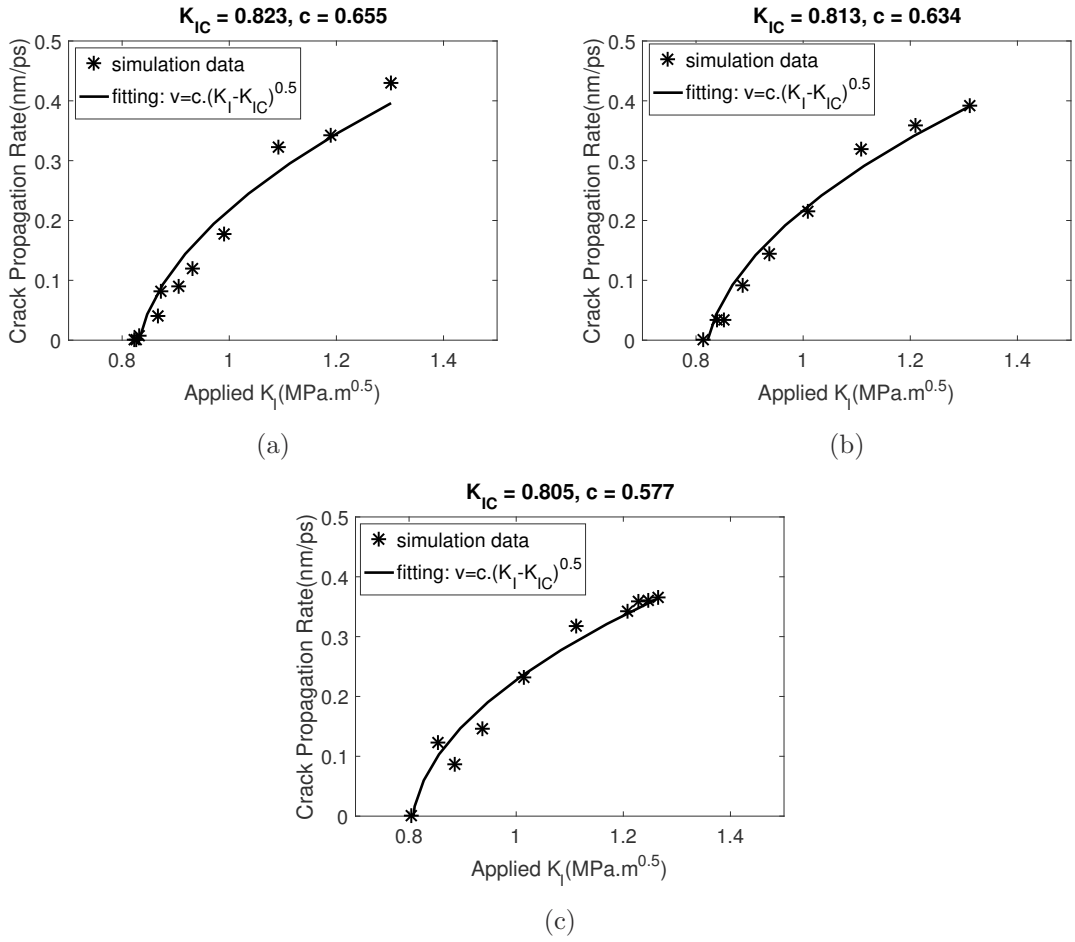

Figure 6.2: Crack propagation rates as a function of the applied stress intensity factor for different strain-rates: (a) $\dot{\epsilon} = 10^7$ ($K_{IC} = 0.805$ and $c = 0.655$), (b) $\dot{\epsilon} = 10^6$ ($K_{IC} = 0.813$ and $c = 0.634$), (c) $\dot{\epsilon} = 10^4$ ($K_{IC} = 0.823$ and $c = 0.577$).

propagation-rate shows a quadratic dependence on the SIF. The critical K_{IC} decreases with decreasing strain-rate. A similar trend is also seen in the strain-rate dependence of parameter c. The effect of temperature is studied for two different temperatures, viz. $T = 300K$ and $T = 200K$. Figures 6.3 show the strain-rate and temperature dependence of K_{IC} and c. The figures show that the effect of temperature on K_{IC} and c is more prominent compared to that of the strain-rate.

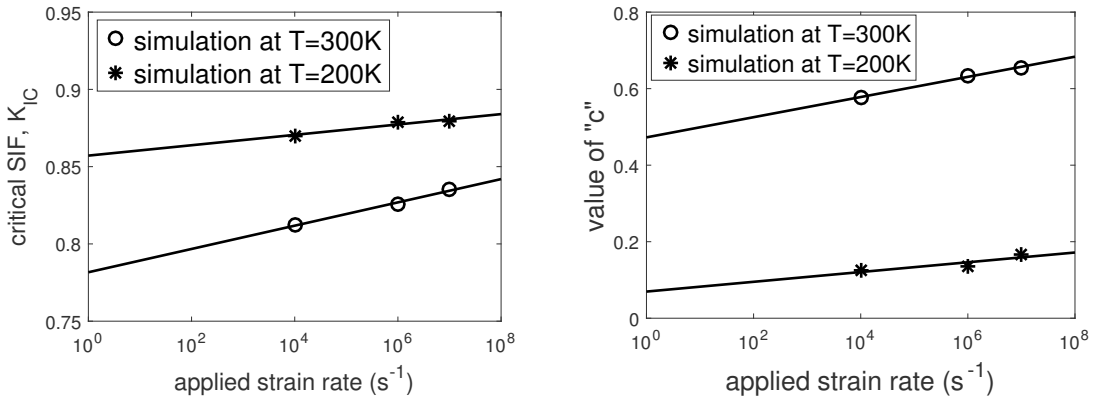

(a) (b)

Figure 6.3: Strain-rate and temperature dependence of: (a) critical stress intensity factor (K_{IC}) and (b) value of c in equation (5.11).

6.1.2 Developing a Phase-Field Model from Multiscale Simulations for Brittle Fracture

Phase-field modeling manifests a regularized discontinuous crack surface in a continuous medium by introducing an auxiliary scalar field variable to represent the crack topology [97, 98]. The sharp crack discontinuity is approximated by a smooth transition between the continuous and discontinuous material phases. Phase-field models are based on the partitioning of the free energy density into components due to recoverable elastic, defect and inelastic dissipation, and fracture. In this work, the elastic and fracture energy densities in this partitioning are extracted from the concurrent model and compared with conventionally accepted forms in phase-field models.

An energy partitioning technique, proposed in [16] to study the energy contribu-

tion of deformation mechanisms for an atomic system is adopted with the concurrent atomistic-continuum model. In [16], the incremental energy due to the externally applied load and the contribution from different deformation mechanisms has been partitioned as:

$$dW = dQ + dU_{el} + dU_{inel} + 2\gamma_s dA = dQ + dU \tag{6.1}$$

where dW is the incremental work potential due to externally applied loads, dQ is the generated heat from dissipative processes like dislocation glide, twin propagation etc., dU_{el} is the incremental recoverable elastic strain energy, dU_{inel} is the increment of energy due to defects like dislocations, twins and voids, and $2\gamma_s dA$ corresponds to the incremental energy due to the increment of crack surface area dA with surface energy density γ_s. In the present concurrent model, dU is the total energy comprising the strain energy of the continuum domain and the total potential energy of the atomistic domain. dW and dU are written as:

$$dW = \int_{\partial\Omega_C} \boldsymbol{t} \cdot \Delta\boldsymbol{u}^C dA \tag{6.2a}$$

$$dU = \int_{\Omega_C \setminus \Omega_{C_I}} \boldsymbol{\sigma} : \Delta\boldsymbol{\epsilon} dV + \sum_{p \in \Omega_A \setminus \Omega_{A_I}} \Delta\Phi_p(\bar{\boldsymbol{r}}) + \frac{1}{2}\left[\int_{\Omega_{C_I}} \boldsymbol{\sigma} : \Delta\boldsymbol{\epsilon} dV + \sum_{p \in \Omega_{A_I}} \Delta\Phi_p(\bar{\boldsymbol{r}})\right] \tag{6.2b}$$

The first term in equation (6.2b) is the elastic strain energy of the continuum domain, the second term is the total potential energy of the atomistic domain and the third

is the averaged contribution from both domains in the handshake region. The heat generated in the system dQ is computed as $dQ = dW - dU$. The heat generated dQ and the inelastic energy dU_{inel} during brittle crack propagation are found to be negligible since plastic deformation mechanisms are essentially absent. Hence, $dU = dW = dU_{el} + 2\gamma_s dA$. dU_{el} is computed by unloading the system and evaluating the energy recovered during the unloading process. The fracture energy $2\gamma_s dA$ during crack propagation is then computed as $2\gamma_s dA = dU - dU_{el}$. Figure 6.4 shows the evolution of fracture energy and crack length as a function of the applied strain. The surface energy γ_s of the material can be calculated from the fracture energy as $\gamma_s = \frac{dU - dU_{el}}{2dA}$. The computed values of γ_s on the (100) plane in the fcc crystal from the concurrent model simulations are compared with reported values in the literature in table 6.2.

Parameter	Concurrent model	ab initio [99]	ab initio [5]
γ_s (mJ/m^2)	2017	2280	1878

Table 6.2: Comparison of computed values of γ_s on the (100) plane from the concurrent model simulations with reported values in the literature.

For comparing with the continuum phase field model and extracting parameters in the free energy expressions, the elastic model in [97, 98] is adopted. For a purely elastic deformation, $\mathbf{F} = \mathbf{F^e}$, where $\mathbf{F}$ is the deformation gradient and $\mathbf{F}^e$ is its elastic part. The free energy density functional can be obtained from the proposed form in [98] as:

$$\rho_0 \psi = \frac{1}{2}\tilde{\mathbf{E}} : \mathbf{C^e} : \tilde{\mathbf{E}} + \frac{g_c}{2l_c}(s^2 + l_c^2 \left(\nabla_X s . \nabla_X s\right)) \tag{6.3}$$

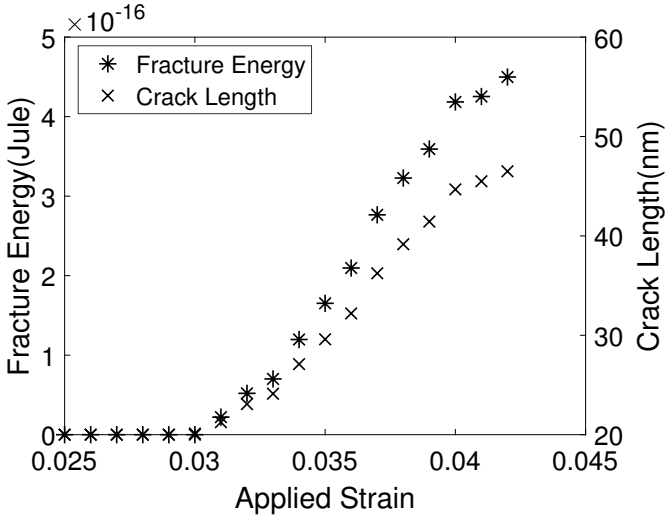

Figure 6.4: Evolution of fracture energy and crack length as a function of the applied strain

where ρ_0 is the density, $\tilde{\mathbf{E}}$ is a modified Green-Lagrange strain tensor accounting for tension compression-asymmetry in the presence of a crack, and $\mathbf{C^e}$ is the fourth order elasticity tensor. The second term is the phase field fracture energy expressed in terms of an order parameter s. g_c is a material constant related to the fracture toughness and l_c is a length scale parameter that controls the regularized crack thickness. For elastic deformation, the modified Green-Lagrange strain tensor is defined as:

$$\tilde{\mathbf{E}} = \frac{1}{2}(J^{\frac{2}{3}} - 1)(g_1(s) - g_2(s))\mathbf{I} + \frac{1}{2}g_2(s)(\mathbf{F^T F} - \mathbf{I}) \tag{6.4}$$

where $\mathbf{F}$ is the elastic deformation gradient, $J = det\mathbf{F}$ is its determinant and $\mathbf{I}$ is identity tensor. $g_1(s)$ and $g_2(s)$ are functions of the phase field order parameter s, defined as:

$$g_1(s) = \begin{cases} 1 & \text{for } J < 1 \\ 1 - s & \text{otherwise} \end{cases} \tag{6.5}$$

$$g_2(s) = 1 - s \tag{6.6}$$

The value of g_c in the continuum phase field equation (6.3) is evaluated from simulations of the hyperdynamics-accelerated concurrent model. Several simulations are conducted using the computational specimen described in section 5.3. The specimen dimensions for the continuum phase field simulations are the same as the concurrent model i.e. 200 nm × 200 nm × 4.22 nm, with a through thickness crack of length 20 nm placed symmetrically at its center. Biaxial displacement controlled loading is applied in the x and y directions. The linear elastic constitutive parameters used for this study are given in table 6.3. The length scale parameter is chosen to be $l_c = 1$ nm in this study.

Parameter	c_{11} (GPa)	c_{12} (GPa)	c_{44} (GPa)	l_c (nm)
Value used	244.6	150.8	125.1	1

Table 6.3: Elastic stiffness coefficients for the phase field simulations.

From a number of phase field simulations, the value of g_c for which the evolution of fracture energy and crack length match those of the concurrent model is found to be $g_c = 4.6$ J/m^2. Figure 6.5(a) shows the comparison of fracture energy (second

term in equation (6.3)) as a function of applied strain for the concurrent model and the elastic phase-field model with $g_c = 4.6\ J/m^2$. Though there is a difference at the beginning of crack propagation, the fracture energies from both the models match quite well but with increasing crack propagation. A similar trend is also seen for the crack length evolution in figure 6.5(b), which indicates the potential of developing phase field models from multiscale simulations.

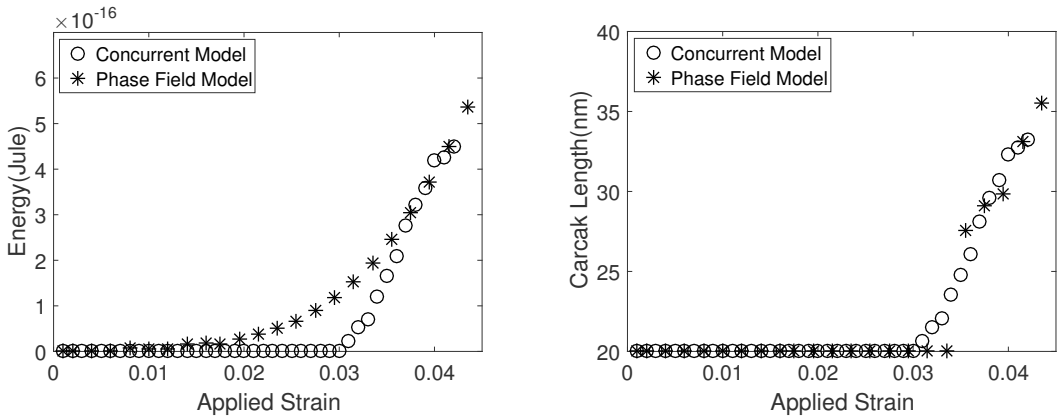

(a) (b)

Figure 6.5: Comparison of (a) fracture energy and (b) crack length as a function of applied macroscopic strain, by the concurrent and the phase field models with $g_c = 4.6\ J/m^2$.

6.2 Conclusions

In this chapter, the concurrent model is used to study strain-rate and temperature effects on crack propagation in a nickel single crystal. The crack orientation is chosen to favor propagation over dislocation nucleation. For quantitative understanding, the crack propagation rate is represented by a parametric continuum model using

two parameters. Both the parameters show a stronger temperature dependence in comparison with strain-rate for this problem. Finally, the concurrent model is used to evaluate the free energy density function for phase-field modeling of crack propagation in a continuum medium. Partitioning of the free energy enables isolating contributions from different mechanisms and then equating them for the concurrent and continuum phase-field models. Parameters in the phase field energy functions can be calibrated from the partitioned energy functions in the concurrent model. The phase-field parameter g_c is calibrated by this process and validation studies show very good agreement. This elucidates the potential of the concurrent model as a modeling tool for large scale continuum fracture models. In the next chapter, the same concurrent model will be used to study the crack propagation and plasticity evolution process during ductile fracture.

Chapter 7

Extracting the Evolution laws for Crack Propagation and Plasticity Evolution for Ductile Fracture

In this chapter, the concurrent coupled Atomistic-Continuum model is used to investigate the crack propagation and evolution of plasticity during ductile fracture. The model is used to extract some crucial evolution laws related to the crack propagation and evolution of dislocation density.

7.1 Details of the Computational Domain

A nickel single crystal with a crack embedded in it is used for the computational study. A through thickness crack in the xz-plane of initial length $2a_o = 20nm$ is embedded in the specimen. The atomistic domain $Omega_A$ is a cylindrical region. The lattice orientation of the specimen with respect to the global axis is $x \rightarrow [11\bar{2}]$, $y \rightarrow [111]$ and $z \rightarrow [1\bar{1}0]$. This specific crystal orientation is known to nucleate straight dislocations parallel to the crack tip[47].

7.1.0.1 Determining the Size of the Computational Domain and the Dislocation Free Zone

As already discussed in section 2.3 that it has experimentally been observed [44, 100] that the presence of a microcrack creates a localized region of dislocation free zone in front of the crack tip. That dislocation free zone can be considered as a perfect crystal devoid of defects of any form. To determine the overall size of the computational domain, it is needed to estimate the approximate size of the dislocation free zone. The size of the dislocation free zone can be determined by analyzing the stress field due to the presence of the crack together with an approximate estimation of the critical resolved shear stress of the material due to the preexisting dislocations. The density of the preexisting dislocations in nickel can be $O(10^{15})$[101]. With this dislocation density the approximate passing stress τ^{α}_{pass} (equation 2.23) can be com-

puted to be $\approx 90MPa$. The computed passing stress τ^{α}_{pass} can be considered as the critical resolved shear stress(CRSS). Due to the presence of the crack, the resolved shear stress(RSS) in the vicinity of the crack will be much higher than the CRSS. This high RSS will cause the dislocations to move away from the vicinity of the crack and form a localized dislocation free zone.

From the previous study in [47], this particular configuration has been observed to nucleate dislocation at volume averaged macroscopic stress of 3GPa. The size of the dislocation free zone can be determined by analyzing the stress field due to the presence of a crack with externally applied bi-axial loading $\sigma_0 = 3GPa$ using Linear Elastic Fracture Mechanics(LEFM). Presence of a center crack in an infinite plate under uniform bi-axial loading can be modeled using 'Westergaard Function Method'[102]. The stress field around the crack due to the externally applied far field bi-axial stress σ_0 can be given as (section 3.4.1 in chapter-3 of [102]),

$$\begin{aligned}
\sigma_{xx} &= \frac{\sigma_0 r}{\sqrt{r_1 r_2}}\left[\cos(\theta - \frac{1}{2}\theta_1 - \frac{1}{2}\theta_2) - \frac{\sigma_0 a_0^2}{(r_1 r_2)} r\sin\theta \sin\frac{3}{2}(\theta_1+\theta_2)\right] \\
\sigma_{yy} &= \frac{\sigma_0 r}{\sqrt{r_1 r_2}}\left[\cos(\theta - \frac{1}{2}\theta_1 - \frac{1}{2}\theta_2) + \frac{\sigma_0 a_0^2}{(r_1 r_2)} r\sin\theta \sin\frac{3}{2}(\theta_1+\theta_2)\right] \\
\sigma_{xy} &= \frac{\sigma_0 r}{\sqrt{r_1 r_2}}\left[\frac{a_0^2}{(r_1 r_2)} r\sin\theta \cos\frac{3}{2}(\theta_1+\theta_2)\right]
\end{aligned} \tag{7.1}$$

Where $2a_0$ is the crack length. The other symbols used in equation 7.1 bears usual meaning and also depicted in the inset of figure 7.1. The crack size was predetermined with $2a_o = 20nm$. In the present study, the orientation of the crystal with respect to the global axis is $x \rightarrow [11\bar{2}]$, $y \rightarrow [111]$ and $z \rightarrow [1\bar{1}0]$ and the embedded crack

has it's tip located along the z-axis. In this particular orientation, the slip plane with maximum resolved shear stress(RSS), i.e, the most critical slip plane, is inclined at an angle of 70^o relative to the crack plane. Hence to obtain the field of maximum RSS, the stress state obtained from equation 7.1 is rotated at angle of 70.5^o according to the rotation of a second order tensor. Figure 7.1 shows the contour plot of the RSS on the most critical slip plane for externally applied loading of $\sigma_0 = 3GPa$. It can be seen that beyond the cylindrical region with radius of 70nm, the RSS value drops below 0.09GPa or 90MPa. Hence, a cylindrical region(Ω_C^{NDD} in figure 2.3) of radius 70nm is considered as free from initial dislocations. The dislocation free region is followed by an annular region where initial dislocation density is graded from 0 to $10^{15}m^{-2}$, the rest of continuum region consists an uniform initial dislocation density of $10^{15}m^{-2}$. It should be noted that the initial dislocation free region does receive dislocations as dislocations starts to nucleate from the crack tip.

7.1.0.2 Determining the Size of the Atomistic Domain

The dimension of the atomistic domain is determined based on the extent of the stacking fault. In FCC crystal, a full dislocation always gets split into two partials, a leading partial and a trailing partial. The leading partial nucleates first which is followed by the trailing partial. After the nucleation, as the leading partial propagates through the crystal, it leaves behind a stacking fault which is a localized HCP stacking in otherwise FCC crystal. As the trailing partial gets nucleated and propagates

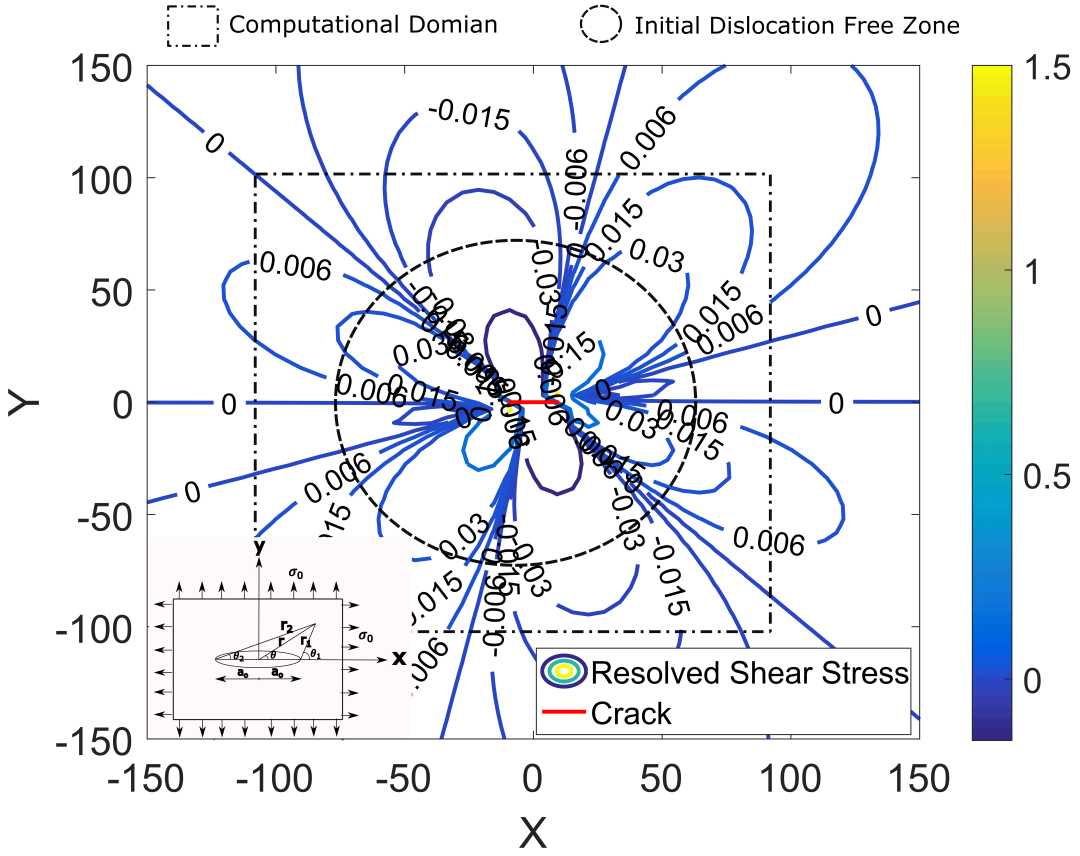

Figure 7.1: Resolved shear stress based on LEFM. Spatial distances are in nm and the stress is in GPa.

through the crystal, it removes the stacking fault restoring the perfect crystal structure of the FCC. In the present study, the material model used for the continuum region is the dislocation density-based crystal plasticity model. In this continuum model, only full dislocations are considered. Due to this reason, while transferring the nucleated dislocations at the interface Ω_I it is necessary that both the leading and the trailing partial get's nucleated, so that the algorithm used to extract the dislocations from atomic configuration (sec. 3.1) i.e, Dislocation Extraction Algorithm [50] can identify the pair of partials as part of a full dislocation. Hence, it is

necessary to make the radius of the atomistic region Ω_A to be more than the maximum stretch of the stacking fault. It has experimentally been observed that the stretch of the stacking fault for nickel can be anywhere between 15Å to 50Å [103]. It should also be noted that for the atomistic-continuum coupled model, owing to a large number of degrees of freedom ($O(10^6)$), the atomistic region is computationally the most expensive. Hence, an optimal size of the atomistic region is computationally desirable.

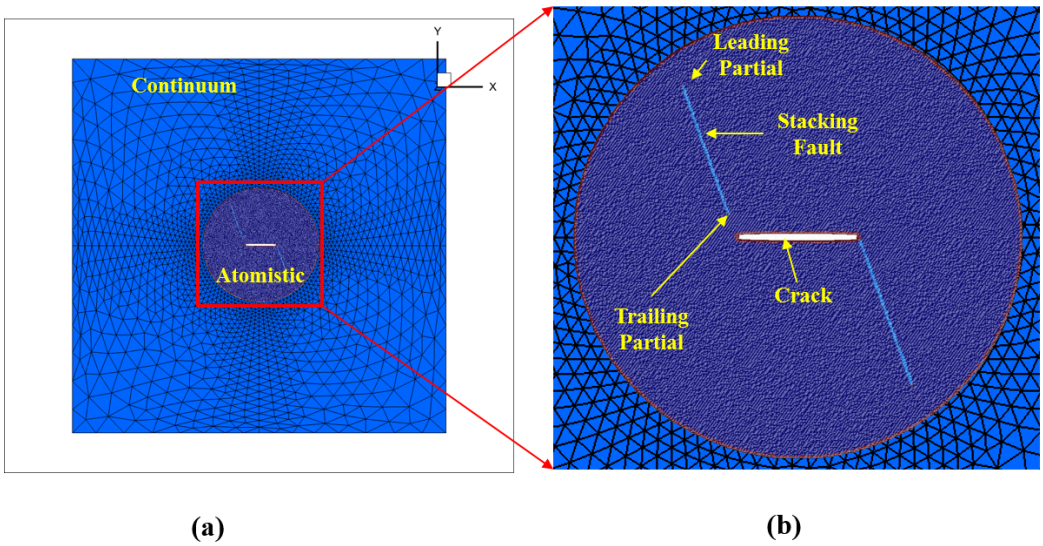

Figure 7.2: Determining the size of the atomistic domain Ω_A by studying the stretch of the stacking fault: (a)the coupled model, (b) zoomed in view of the atomistic region.

To identify the optimal size of the atomistic region, a coupled simulation is conducted with a large size of the atomistic region, $R_A = 50nm$. The overall size of the domain kept fixed to $200nm \times 200mm \times 4.22nm$. The stretch of the stacking fault for the first few dislocations are noted. It has been observed that the stretch of the

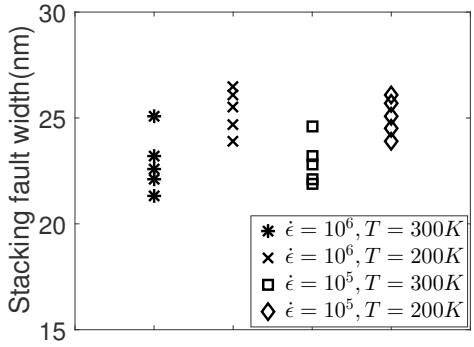

Figure 7.3: The variability of the maximum stretch of stacking fault for different strain rates of $\dot{\epsilon} = 1.0e^6$ *and* $1.0e^5$ and two different temperatures of $T = 300K$ *and* $200K$.

stacking fault reaches maximum length at the onset of the nucleation of the trailing partial, as shown in figure 7.2. The maximum stretch is observed as high as 27nm. The stretch of the stacking fault is reduced drastically as the trailing partial nucleates and the full dislocation moves away from the crack tip.

The above-mentioned investigation of the maximum stretch of stacking fault is repeated for two different strain rates viz $\dot{\epsilon} = 10^6$ *and* 10^5 and for two different temperatures viz. $T = 300K$ *and* $200K$. Figure 7.3 shows the distribution of the stacking fault width as observed during the nucleation of the first five dislocations under different strain rates and temperatures. It has been found that the width of the stacking fault increases with strain rate and decreases with temperature. The maximum width of 27nm is observed for $\dot{\epsilon} = 10^6$ *and* $T = 200K$. The width of the stacking fault, in general, is much larger than the equilibrium stacking fault width [103]. The large stretch of the stacking fault can be attributed to the high gradient of the near crack tip stress field and also during the nucleation of dislocations, the

process is highly non-equilibrium in nature.

With the known approximate estimation of the stacking fault width to be 27nm, the size of the atomistic region is chosen to be $R_A = 40nm$. A conservative size of the atomistic region(Ω_A) will make sure that both the leading as well as trailing partials are nucleated before it moves in the interface region(Ω_I). The size of the atomistic region is kept fixed for all subsequent simulations.

7.2 Validation and Assessment of the Concurrent Model in comparison with a full MD model

Prior to its use in the quantification of the nucleated dislocation density from a preexisting micro-crack, the ductile atomistic-continuum concurrent model is validated with a fully atomistic model where Molecular Dynamics is used.

A nickel single crystal with a crack embedded in it is used for the validation purpose. A full atomistic model of dimension $200nm \times 200nm \times 4.22nm$ would contain 15million atoms, which is computationally prohibitive. Hence, the x-dimension of the domain is reduced to 100nm than the one prescribed in section 7.1.0.1. The physical dimension of the domain is taken to be $100nm \times 200mm \times 4.22nm$. The computational domain size, the orientation and the boundary condition are shown in

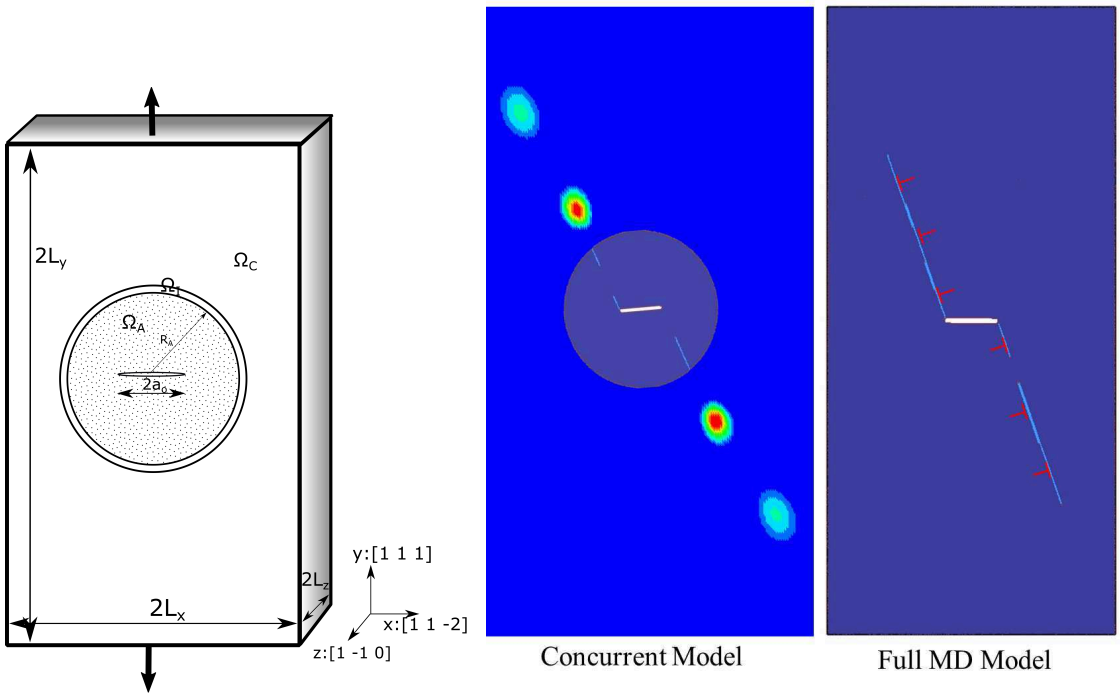

(a) (b)

Figure 7.4: Comparison of the performance of the concurrent model with respect to the full MD model: (a)specimen details for the simulation, (b)evolution of dislocation in concurrent and MD model.

figure 7.4(a). A through thickness crack in the xz-plane of initial length $2a_o = 20nm$ is embedded in the specimen. The atomistic domain Ω_A is a cylindrical region of radius $R_A = 30nm$ and the interface region Ω_I is an annular region with an inner radius of 25nm and outer radius of 35nm respectively. The atomistic region contains about 1.5 million nickel atoms with an FCC lattice structure. The lattice constant of nickel is $a_o = 3.52$Å. A through-thickness crack is introduced at the center of the specimen by removing two layers of atoms on both sides of the crack plane. The lattice orientation of the specimen with respect to the global axis is $x \rightarrow [11\bar{2}]$, $y \rightarrow [111]$ and $z \rightarrow [1\bar{1}0]$. This specific crystal orientation is known to nucleate straight dislocations

parallel to the crack tip[47]. The continuum region of the domain is discretized using finite element mesh containing approximately 4000 nodes and 15000 4-noded constant strain tetrahedral elements. The stiffness coefficients for pure Nickel used in the present study are given in table 5.1. These stiffness coefficients have previously been calibrated to match with the EAM potential of the atomistic model in [2, 1]. The crystal plasticity parameters are given in table 7.1.

Parameter	Values	Parameter	Values	Parameter	Values
c_1	0.1	c_2	0.8	c_3	1.0×10^{-3}
c_4	1.0×10^{-4}	c_5	10.0	c_6	10.0
c_7	0.3	τ_c	110MPa	ρ_c	1.0×10^{11}
b	2.49Å	Q	6.5×10^{-19}		

Table 7.1: CPFE material parameters [3].

The full MD model is discretized with nickel atoms of FCC structure with the lattice constant of $a_o = 3.52$Å. The full MD model consists of about 7.5 million atoms. Both the concurrent and the full MD model is free from any initial dislocation density.

For the concurrent model, the simulation begins by static minimization of the energy of the atomistic region which is followed by a dynamics equilibration of the atomistic region. This is followed by the establishment of the atom-node connectivity between the nodes and atoms in the interface region. Ghost force correction is introduced for the surface atoms Ω_A^s to mitigate the free surface effect at the interface. Subsequently, a bi-axial displacement controlled loading is applied in x and y direction at a constant strain rate of $\dot{\epsilon} = 1.0 \times 10^6 s^{-1}$. NVE ensemble is used for the MD

simulation. The temperature of the atomic system is maintained at $300K$ by using Langevin thermostat [48] and the z-direction pressure is controlled to zero by using Berendsen barostat [104].

For the full MD model, the simulation starts by static minimization of the whole system which is followed by the dynamics equilibration to achieve a stress-free state and temperature of 300K. NPT ensemble is used for the dynamics equilibration. This is followed by the displacement controlled simulation by applying a bi-axial displacement controlled loading in x and y direction at a constant strain rate of $\dot{\epsilon} = 1.0 \times 10^6 s^{-1}$. NVE ensemble along with Langevin thermostat [48] and Berendsen barostat [104] is used to control the temperature of the system at 300K and stress-free z-faces i.e $\sigma_{zz} = 0.00$.

7.2.1 Comparison of Critical Stress Intensity Factor for Dislocation Nucleation

The critical state for the onset of the dislocation nucleation from the crack tip is measured by the mode-I stress intensity factor(SIF) K_I. The SIF for mode-I fracture can be computed as,

$$K_I = \sigma\sqrt{\pi a}.\eta \tag{7.2}$$

where σ is a far field stress on the external boundary of the continuum domain.

It is computed as $\sigma_{yy} = \frac{F_y}{A_{xz}}$, where F_y is the y-component of total reaction of all nodes, on which displacement controlled loading is applied. The geometric factor η compensates for the finite specimen dimensions in this study, as opposed to the infinite dimensions considered in its derivation. A polynomial form of η has been given as [95]:

$$\eta = sec\left(\frac{\pi a}{2L_x}\right)^{1/2}\left[1 - 0.025\left(\frac{a}{L_x}\right)^2 + 0.06\left(\frac{a}{L_x}\right)^4\right] \tag{7.3}$$

where a is the crack length and L_x is the x-dimension of the specimen as shown in figure 7.4(a).

The critical SIF K_{IC} value for the nucleation of the first dislocation from the crack tip is found to be $0.705MPa.\sqrt{m}$ and $0.71MPa.\sqrt{m}$ for the full MD model and the concurrent model respectively. The critical SIF values from the concurrent model is in good agreement with the full MD model.

The critical SIF for the nucleation of dislocation can be compared with the analytical solution obtained by 'Rice's continuum formulation' [105]. According to the analysis, the critical stress intensity factor for mode-I loading is given as:

$$K_I = \sqrt{2\mu\gamma_{us}\frac{Y}{1-\nu}} \tag{7.4}$$

where μ and ν are the shear modulus and the Poisson's ration of the material respectively. γ_{us} is the unstable stacking fault energy of the material. Y is the

geometric factor to account for the angle of inclination between the crack plane and the slip plane and is given as:

$$Y = \frac{8}{(1+\cos\theta)\sin^2\theta} \tag{7.5}$$

The nucleation criterion given by Rice (equ. 7.4) is known to underestimate the critical SIF for mode-I loading. This anomaly was attributed to the fact that the large surface stress on the crack surface should be incorporated [106]. The modified form of the nucleation criterion is given as:

$$K_I = \sqrt{2\mu\left(\gamma_{us} + f_{eff}\epsilon\right)\frac{Y}{1-\nu}} \tag{7.6}$$

where $f_{eff}\epsilon$ is the surface correction term. The higher order effect due to the large frack tip strain is incorporated by expanding f about $\epsilon = 0$, $f_{eff} = f_0 + \frac{1}{2}(\delta f/\delta\epsilon)\epsilon$. μ, ν, γ_{us}, f_0, $\delta f/\delta\epsilon$ are all material parameters. The value of these material parameters for nickel is given in table 7.2. Then the critical SIF for nucleation of dislocation becomes $\approx 0.661 MPa.\sqrt{m}$. Table 7.3 shows the comparative values of the critical SIF for dislocation nucleation by three different methods viz, analytical, full MD and concurrent model.

Parameters	$\mu(GPa)$	ν	$\gamma_{us}(Jm^{-2})$	$f_0(Jm^{-2})$	$\delta f/\delta\epsilon(Jm^{-2})$
Values	125	0.285	0.143	0.816	2.223

Table 7.2: Material parameters assosciated with nucleation of crack from a crack tip of nickel single crystal, obtained from [4, 5].

Models	Analytical	MD	Concurrent
K_{IC}	0.661	0.705	0.71

Table 7.3: Comparison of critical SIF(in $MPa.\sqrt{m}$).

7.2.2 Comparison of Nucleated Dislocation Density

It is worthwhile to compare the perforation of the concurrent model with the full MD model beyond the nucleation of the first dislocation. For this, the evolution of the density of the nucleated dislocations are compared. The dislocation density for the full MD model is computed by,

$$\rho_{MD} = l_{MD}/V \tag{7.7}$$

where l_{MD} is the total dislocation length within the entire computational domain and V is the volume of the computational domain. To obtain the total length(l_{MD}) of all the dislocations, DXA[50] is used for extracting the dislocations from the atomic configuration data. Once the dislocation are identified in the form of dislocation bids and length segments, the total length of the dislocations are computed as $l_{MD} = \sum_{i=1}^{N_l} |d\boldsymbol{l}_i|$, where $|d\boldsymbol{l}_i|$ is the length of the $i'th$ dislocation segment and N_l is the total number of dislocation segments present inside the domain.

The dislocation density for the concurrent model is computed as:

$$\rho_{concurrent} = \frac{1}{V}\left[\sum_{i \in \Omega_A \bigcup \Omega_I} |d\boldsymbol{l}_i| + \int_{\Omega_C} \rho_{nucl} d\Omega\right] \tag{7.8}$$

In equation 7.8 the first term corresponds to the total length of the dislocation segments within the atomistic(Ω_A) and the interface(Ω_I) region. The second term computes the volume integral of the nucleated dislocations density within the continuum. In the integral in the second term is evaluated over the SPH particles as,

$$\int_{\Omega_C} \rho_{nucl} d\Omega = \sum_{p \in \Omega_C} \left[\sum_{q=1}^{N_p} \rho^q_{nucl} \overline{W}(\boldsymbol{x}_p - \boldsymbol{x}_q, h) d\omega_q\right] d\omega_p \tag{7.9}$$

where the first summation is over the SPH particles within the continuum domain Ω_C. N_p is the number of SPH particles within the support domain of the kernel function of $p'th$ particle. $\overline{W}(\boldsymbol{x}_p - \boldsymbol{x}_q, h)$ is the RKPM kernel function of the $p'th$ particle evaluated at the location of the $q'th$ particle. $d\omega_p$ and $d\omega_q$ is the weight associated to $p'th$ *and* $q'th$ particle respectively. ρ^q_{nucl} is the SPH solution for nucleated dislocation density at $q'th$ particle.

Figure 7.5 shows the evolution of the nucleated dislocation density from the full MD model and the concurrent model. The evolution of the nucleated dislocation density in the concurrent model agrees very well with the MD-based model. The quasi-periodic jump in the dislocation density signifies the nucleation of a new dislocation at the crack tip. The particular orientation of the crystal with respect to the crack tip and thin z-dimension makes the nucleated dislocations to be straight in

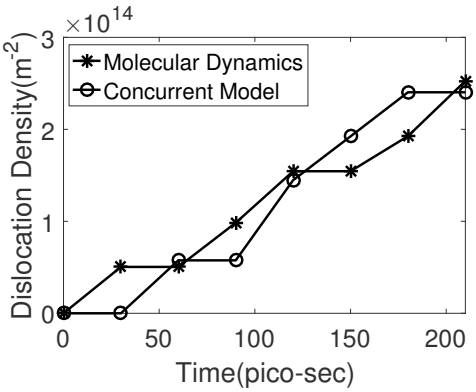

Figure 7.5: Evolution of dislocation density in the concurrent model and the MD model.

nature, extending throughout the thickness.

7.2.3 Comparison of Computational Cost

The computational efficiency of the concurrent model is accessed by comparing it with the MD model where the whole computational domain is discretized at an atomistic resolution. Both the code for the FE model(in house code) and the MD (LAMMPS code) is parallelized using a message passing interface (MPI) to take advantage of multi-processor computation. For the concurrent model, the distribution of processors between the atomistic model and the FE model is chosen for optimal efficiency. Due to the large degrees of freedom of the atomistic domain, almost 95% of the processors are assigned for the atomistic model and the rest is assigned for the continuum model(both FE and SPH). The computational efficiency of the concurrent model is compared with the MD model in table 7.4. The computational cost is

estimated in terms of CPU-hours on the Bluecrab cluster at Maryland Advanced Research Computing Center (MARCC) using 4 nodes with 24 processors in each node. The efficiency factor is defined as the ratio of CPU-hours between the MD model and the concurrent model.

Model	Concurrent	MD(with time acceleration)	Efficiency Factor
CPU hour	150	2000	13.3

Table 7.4: Comparison of computational cost between full MD simulation and the concurrent model.

7.3 Developing the Evolution Law for the Nucleated Dislocations from the Crack-tip

The concurrent model is used to derive the evolution law of the nucleated dislocations density from a preexisting crack. For the computational study, a single crystal nickel specimen of physical dimension $200nm \times 200nm \times 4.22nm$ is used. Figure 7.6(a) shows the physical dimension, the boundary condition and the crystal orientation of the specimen. A through-thickness crack of length $2a_0 = 20nm$ is embedded at the center of the specimen. The atomistic domain Ω_A is a cylindrical region of radius $R_A = 40nm$ (as derived in sec 7.1.0.2) and the interface region Ω_I is an annular region with an inner radius of 35nm and outer radius of 45nm respectively. The atomistic

region contains about 2.5million nickel atoms with an FCC lattice structure. The lattice constant of nickel is $a_o = 3.52$Å. The lattice orientation of the specimen with respect to the global axis is $x \rightarrow [11\bar{2}]$, $y \rightarrow [111]$ and $z \rightarrow [1\bar{1}0]$. The atomistic region also contains voids, that are randomly distributed throughout the atomistic region Ω_A. The voids are created by randomly removing 0.1% of the total atoms from the perfect crystal. The continuum region of the domain is discretized using finite element mesh containing approximately 5000nodes and 20000 4-noded constant strain tetrahedral elements as shown in figure 7.6(b). A cylindrical region of radius $70nm$ from the center of the crack is considered as free form any initial dislocation density. The rest of the continuum region contains a constant distribution of the initial dislocation density of $10^{15}m^{-2}$. The boost potential due to the Hyperdynamics is applied to a group of atoms located at the crack-tip in a through-thickness cylindrical region of radius 15Å. The material parameter used for the computation study is given in table 5.1 and 7.1.

Figure 7.7 shows the snapshots of the Dislocation structure at two applied macroscopic strains $\epsilon_{11} = \epsilon_{22} = 3.1\%$ and $\epsilon_{11} = \epsilon_{22} = 3.3\%$. The dislocation nucleation and crack propagation do not start together at the same macroscopic strain. Rather it has been observed that first dislocation nucleates at a critical applied strain of $\epsilon_{11} = \epsilon_{22} = 2.9\%$ but first crack propagation has been observed at $\epsilon_{11} = \epsilon_{22} = 3.1\%$.

Figure 7.8(a) shows the evolution of the dislocation density at strain rates of $\dot{\epsilon} = 1.0e6$. At the onset of nucleation, it has been observed to nucleate several

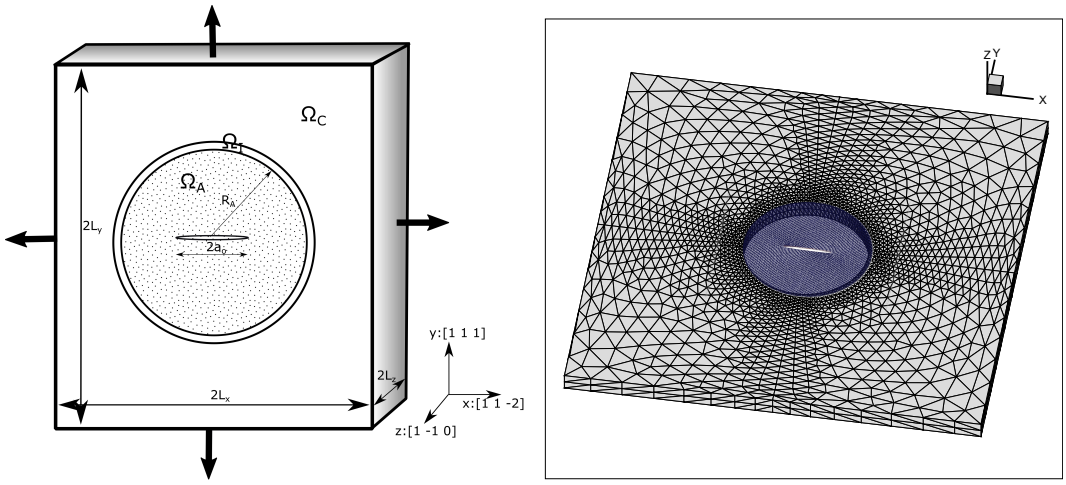

(a) (b)

Figure 7.6: Computational specimen modeled by the concurrent atomistic-continuum model for crack propagation,(a) the details of the geometry, the dimensions and loading and (b) discretization of the atomistic and the continuum domain.

dislocations in quick succession. The macroscopic strain at the onset of nucleation of the first dislocation is found to be $\epsilon_{11} = \epsilon_{22} = 2.9\%$. The critical SIF for dislocation nucleation at the corresponding macroscopic strain is found to be approximately $1.26MPa\sqrt{m}$. To compute the SIF, equation 7.2 is used. Figure 7.8(b) shows the evolution of the crack length as a function of applied macroscopic strain. It can be seen that the crack starts to propagate at a critical applied strain of $\epsilon_{11} = \epsilon_{22} = 3.1\%$. The simulation is terminated as crack reaches very close to the interface region Ω_I. It has been observed (see figure 7.7(b)) that even though the initial crack was along the xz-plane but at the onset of propagation, the crack deviates from the xz-plane at an angle of 70.5^o. The new plane corresponding to the propagation of the crack is a slip plane. It has also been observed that crack does not evolve symmetrically from both the crack-tip.

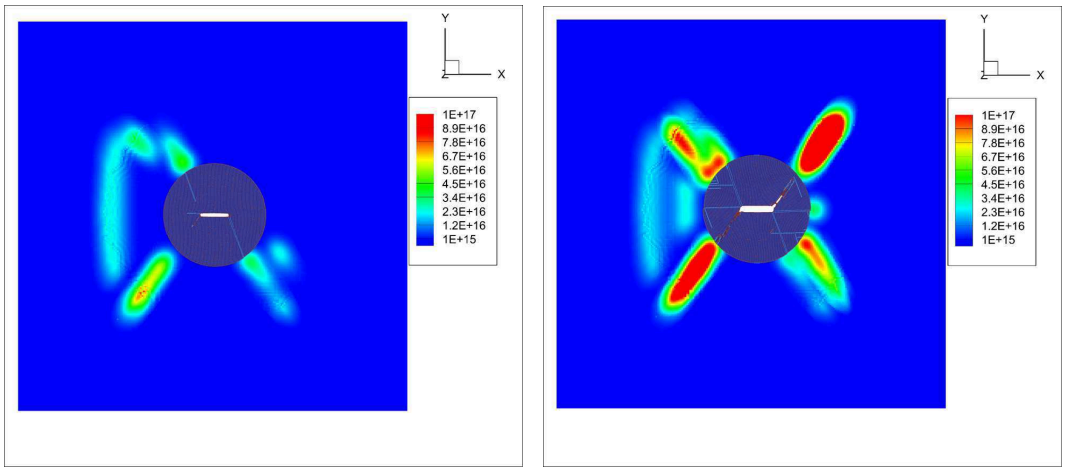

(a) (b)

Figure 7.7: Contour plot of the Dislocation Density. At macroscopic strain of (a)$\epsilon_{11} = \epsilon_{22} = 3.1\%$ and (b)$\epsilon_{11} = \epsilon_{22} = 3.4\%$

The evolution data of dislocation density obtained from the simulation is fitted to a predetermined form assumed as,

$$\rho_{nucl} = a_1 \rho_0 (\epsilon - \epsilon_c)^{a_2} \mathcal{H}(K - K_{IC}) \tag{7.10}$$

where, K_{IC}, a_1 *and* a_2 are material parameters. K_{IC} is the critical SIF for the first dislocation to nucleate. ρ_0 is the reference dislocation density which has a value of $1.0e14m^{-2}$ and $\mathcal{H}$ is the Heaviside step function.

Since the atomistic part of the concurrent model has time acceleration incorporated in it, it is possible to study the nucleation process at a much lower strain rate than that of the conventional MD without time-acceleration. The lowest strain rate that is studied here is $\dot{\epsilon} = 5.0e4$. The values of the parameters are investigated for three strain rates viz. $\dot{\epsilon} = 1.0e6, 1.0e5$ *and* $5.0e4$, values are given in table 7.5. ϵ_c

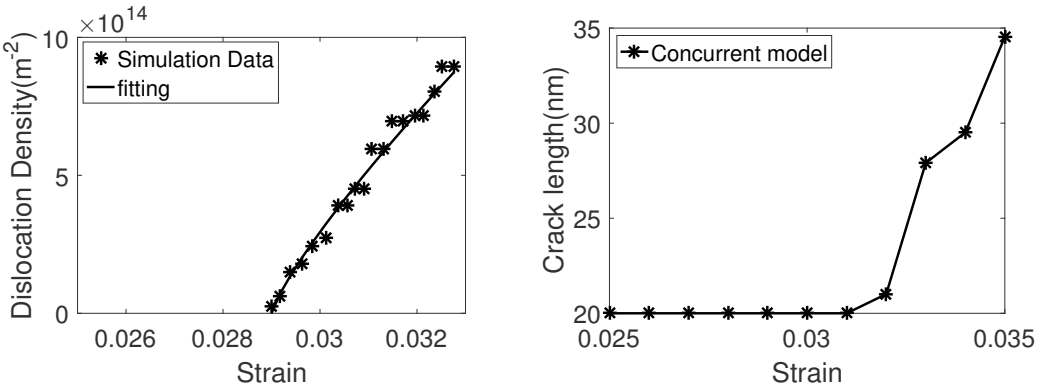

(a) (b)

Figure 7.8: Evolution of (a) dislocation density and (b) crack length as a function of applied strain at rate $\dot{\epsilon} = 1.0e6$.

is the critical strain corresponding to the critical SIF value. The numerical value of ϵ_c is obtained during the simulation itself by identifying the value of ϵ the moment the SIF reaches to K_{IC}. It can be seen from table 7.5 that the K_{IC} is almost the same at both strain rate but the other two parameters i.e, a_1 *and* a_2 has a strong dependence on the strain rate. It implies that the critical state corresponding to the nucleation of the first dislocation is almost the same and can efficiently be represented by critical SIF values, but the subsequent evolution of the dislocation density has a strong dependence on the strain rate.

Strain Rate $\dot{\epsilon}$ (s^{-1})	K_{IC} $(MPa.\sqrt{m})$	a_1	a_2
$1.0e^6$	1.260	8.5	0.82
$1.0e^5$	1.245	7.5	0.78
$5.0e^4$	1.230	7.1	0.75

Table 7.5: Calibrated values of the dislocation density parameters in equation (7.10) obtained from the simulations with the concurrent model at different strain-rates.

Figure 7.9 shows the strain rate and temperature dependence of the three param-

eters (K_{ic}, a_1 *and* a_2). It can be seen that K_{IC} has mild dependence on strain rate but a strong dependence on temperature. On the other hand, for a_1 *and* a_2 the effect of strain rate is more prominent in comparison with temperature.

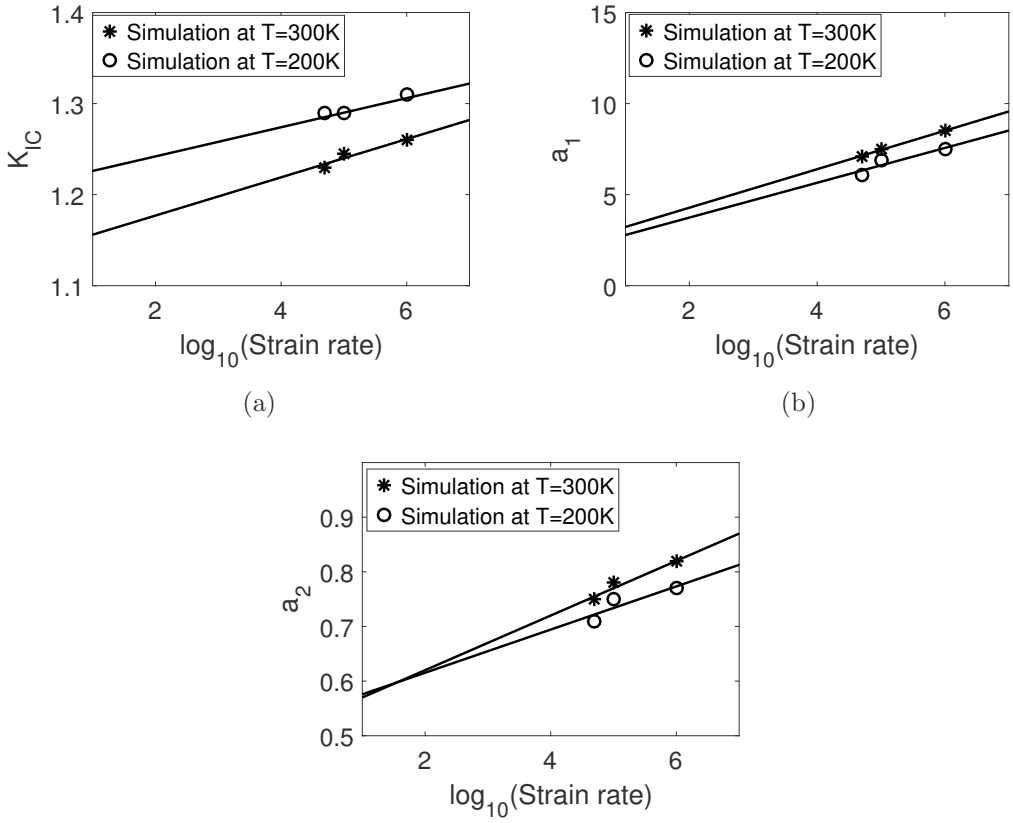

Figure 7.9: Applied strain rate(in logarithmic scale) and temperature dependence of: (a) critical stress intensity factor (K_{IC}), (b) the value of a_1 and (c) the value of a_2 in Eq. 7.10.

7.4 Deriving the energy functional of the Phase-field model for ductile failure using the concurrent model

The phase-field model is a special kind of gradient damage model which became very popular in recent times for modeling fracture in the material at continuum scale [97, 98, 107]. In the phase-field model, the strong discontinuity of a crack is represented by a regularized scale field variable. The success of the phase-field model relies on an appropriate construction of the free energy of the system. The free energy density of a system can be partitioned into different components, the recoverable elastic energy, the fracture energy due to the crack surface and the inelastic defect energy due to the presence of the defects e.g, dislocations.

The evolution law of the nucleated dislocation density derived from the concurrent model is used to augment the free energy functional of continuum phase field model. A crystal plasticity based phase field model developed in [107] is adopted here. According to the model, the phase-field free energy density functional can be constructed as:

$$\rho_0\psi = \rho_0\psi_e(\boldsymbol{E^e}, s) + \rho_0\psi_c(s, \boldsymbol{\nabla_X} s) + \rho_0\psi_d(\boldsymbol{\eta}, s) \tag{7.11}$$

where ρ_0 is the density of the material in reference configuration. The first term i.e,

ψ_e in the right hand side of equation 7.11 is the stored elastic energy density which is given as,

$$\rho_0 \psi_e = \frac{1}{2} \tilde{\mathbf{E}} : \mathbf{C^e} : \tilde{\mathbf{E}} \tag{7.12}$$

where $\tilde{\mathbf{E}}$ is the modified Green-Lagrange strain tensor and $\boldsymbol{C^e}$ is the fourth order elasticity tensor. To incorporate the tension compression asymmetry in the presence of a crack, the elasytic deformation gradient $\mathbf{F^e}$ is decomposed into a volumetric and isochoric part, i.e, $\boldsymbol{F}^e = \boldsymbol{F}^e_{iso} \boldsymbol{F}^e_{vol}$ where the isochoric deformation gradient is $\boldsymbol{F^e_{iso}} = (det \boldsymbol{F^e})^{-\frac{1}{3}} \boldsymbol{F^e}$ and the volumetric deformation gradient is $\boldsymbol{F}^e_{vol} = (det \mathbf{F^e})^{\frac{1}{3}} \boldsymbol{I}$. Then the modified Green-Lagrange $\tilde{\boldsymbol{E}}$ is expressed as,

$$\begin{gathered} \tilde{\boldsymbol{E}} = g_1(J^e, s) \boldsymbol{E^e_{vol}} + g_2(s) \boldsymbol{E^e} \\ \text{where, } g_1(J^e, s) = \mathcal{H}(1 - J^e)(1 - \kappa_s)s \text{ and} \\ g_2(s) = 1 - (1 - \kappa_s)s \end{gathered} \tag{7.13}$$

where, $\boldsymbol{E^e_{vol}}$ is the volumetric part of the Green-Lagrange strain, $\boldsymbol{E^e_{vol}} = \frac{1}{2}(\boldsymbol{F^{eT}_{vol} F^e_{vol}} - \boldsymbol{I})$ and the Jacobian $J^e = det(\boldsymbol{F^e})$. $\mathcal{H}(x)$ is the Heaviside step function. s is the phase field order parameter and $\kappa_s = 0.001$ is a small positive parameter incorporated for numerical stability.

The second term ψ_c in equation 7.11 is the crack surface energy density, and is

given as,

$$\rho_0\psi_c = \frac{g_c}{2l_c}(s^2 + l_c^2\,(\boldsymbol{\nabla}_{\boldsymbol{X}} s.\boldsymbol{\nabla}_{\boldsymbol{X}} s)) \tag{7.14}$$

where g_c is the fracture energy per unit surface and l_c is a length-scale associated with the regularization of the crack density using the phase field variable s.

The third term ψ_d in the right hand side of equation 7.11 is the stored defect energy density due to the defect structures within the material such as dislocations. The degrading stored defect energy is given as [107],

$$\rho_0\psi_d = g(s)\rho_0\hat{\psi}_d(\boldsymbol{\eta}) = g(s)\frac{1}{2}\sum_{\alpha,\beta}^{N_{slip}} h^{\alpha,\beta}|\eta^\alpha||\eta^\beta| \tag{7.15}$$

where η^α *and* η^β are the internal variables corresponding to defects on the α and β slip systems respectively. $g(s) = 1 - s$ is the degradation function and $h^{\alpha,\beta}$ is the interaction matrix between α *and* β slip systems to the defect energy. Using the principle of maximum plastic dissipation, it has been shown in [107] that $\eta^\alpha = |\gamma^\alpha|$, γ^α is the accumulated plastic slip in the α slip system. Then the defect energy becomes,

$$\rho_0\psi_d = g(s)\frac{1}{2}\sum_{\alpha,\beta}^{N_{slip}} h^{\alpha,\beta}|\gamma^\alpha||\gamma^\beta| \tag{7.16}$$

The accumulated plastic slip γ^α has contribution from the two sources of dislocations. One is due to the evolution of the preexisting dislocation density and another one is the contribution from the new dislocations nucleating from the crack tip, i.e,

$$\gamma^{\alpha} = \gamma^{\alpha}_{preexisting} + \gamma^{\alpha}_{nucl} \tag{7.17}$$

where $\gamma^{\alpha}_{preexisting}$ is the plastic slip due to the evolution of the preexisting dislocations and γ^{α}_{nucl} is the extra contribution to the plastic slip coming from the nucleated dislocation from the crack tip. Figure 7.11 shows the phase-field simulation of the crack in a nickel single crystal. The physical dimension of the domain is taken as $200nm \times 200nm \times 4.2nm$ which contains a central crack of length 20nm. The initial crack is represented by setting the phase field variable s to one. The sample is deformed along x and y-axis by applying a displacement controlled loading at a strain rate of $\dot{\epsilon} = 5.0e4$.

To make the phase-field model more physics-based and atomically informed, the parameters of the phase-field model has been derived from the concurrent model by comparing the energetics and the dynamics of the evolution of the crack. The most important parameters that control the crack evolution in this phase-field model is g_c (see eq. 7.14). On the other hand, the set of parameters $h^{\alpha,\beta}$, in equation 7.15, represents the interaction between the dislocation in α *and* β slip system on their contribution in the defect energy (eq. 7.16). These parameters need to be calibrated. Several phase-field simulations are conducted to calibrate the value of g_c and $h^{\alpha,\beta}$ by comparing the evolution of the crack length, fracture energy and defect energy. The specimen dimension of the continuum phase-field model is kept the same as the specimen dimension of the concurrent model. Figure 7.10(a) shows the evolution of

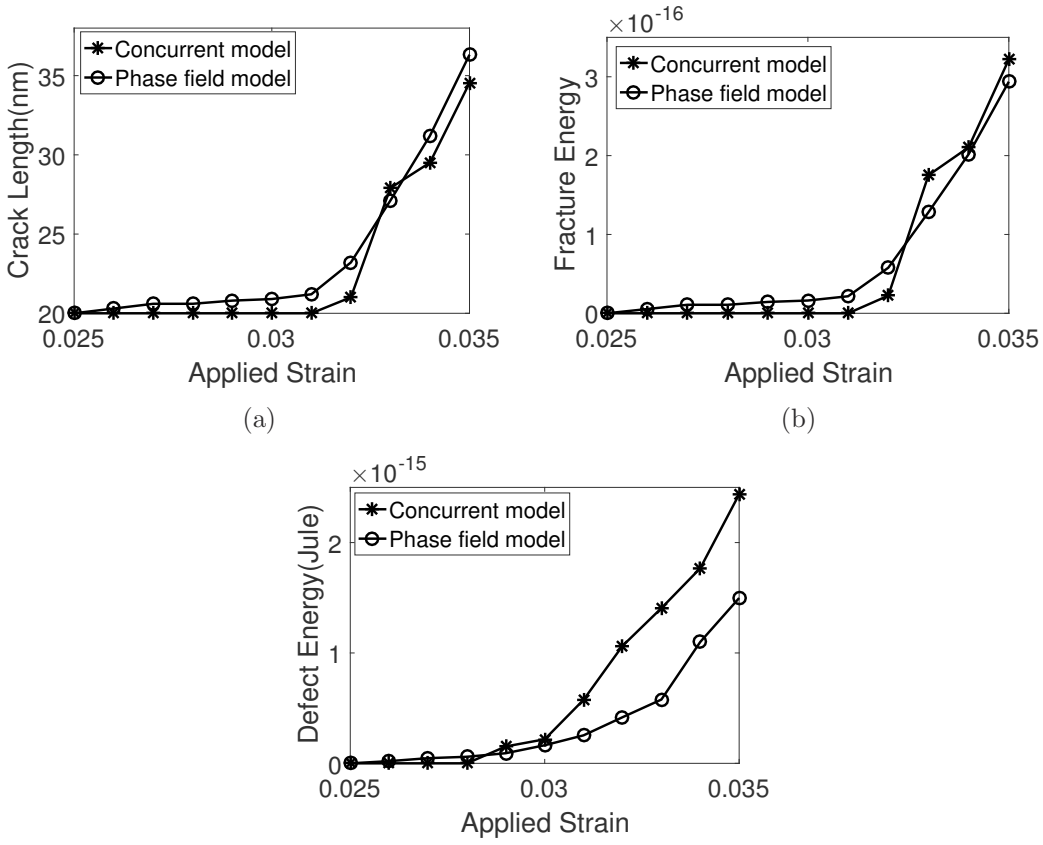

Figure 7.10: Comparison of the evolution of the crack length and different energies between the concurrent model and the phase field model. Evolution of (a) crack length (b) fracture energy and (c) defect energy as a function of applied macroscopic strain.

the crack length with respect to the macroscopic applied strain. It can be seen that for both the concurrent and the phase-field model the evolution of the crack resembles very well. It is worthwhile to mention that, for the phase-field model, the parameter g_c plays the most critical role in the initiation of the evolution of the crack. Hence it is crucial to calibrate the value of g_c accurately. The calibrated value of g_c is found to be $5.35 Jule/m^2$. For the calibration of the components of the interaction matrix

$h^{\alpha,\alpha}$ it is assumed that $h^{\alpha,\beta}$=1.00 ($\alpha \neq \beta$) i.e all off-diagonal terms are assumed to be unity. The calibrated value of the diagonal term i.e $h^{\alpha,\alpha}$ is found to be 1.56. The evolution of the fracture energy is shown in figure 7.10(b). A trend similar to crack length is observed for the evolution of the fracture energy also. Figure 7.10(c) shows the evolution of the defect energy for concurrent and the phase-field model. It can be seen that the evolution pattern of the defect energy is very similar for both the concurrent and the phase-field model but they differ quantitatively. This signifies that the present assumed form of the defect energy (eq: 7.16) for the phase-field model is not complete.

For a better understanding of the importance of nucleated dislocations for crack propagation, the phase-field study is conducted for two samples. One without considering the plastic slip contribution from the nucleated dislocations, the only contribution of the plastic slip was from the evolution of the preexisting dislocations. Another one has a contribution from both the preexisting dislocations as well as from the dislocations nucleated at the crack tip. For the evolution of the nucleated dislocation density, the evolution law obtained from the concurrent model is used (equ. 7.10). Figure 7.11 shows the evolution of the crack in the form of the phase-field parameter s. It can be seen from figure 7.11 that at the same applied strain of $\epsilon_{11} = \epsilon_{22} \approx 3.4\%$ the phase-field model with additional plasticity due to the crack tip dislocations shows significant evolution of the crack. This implies that the plastic slip contribution from the nucleated dislocations has a significant impact on the evolution of the crack.

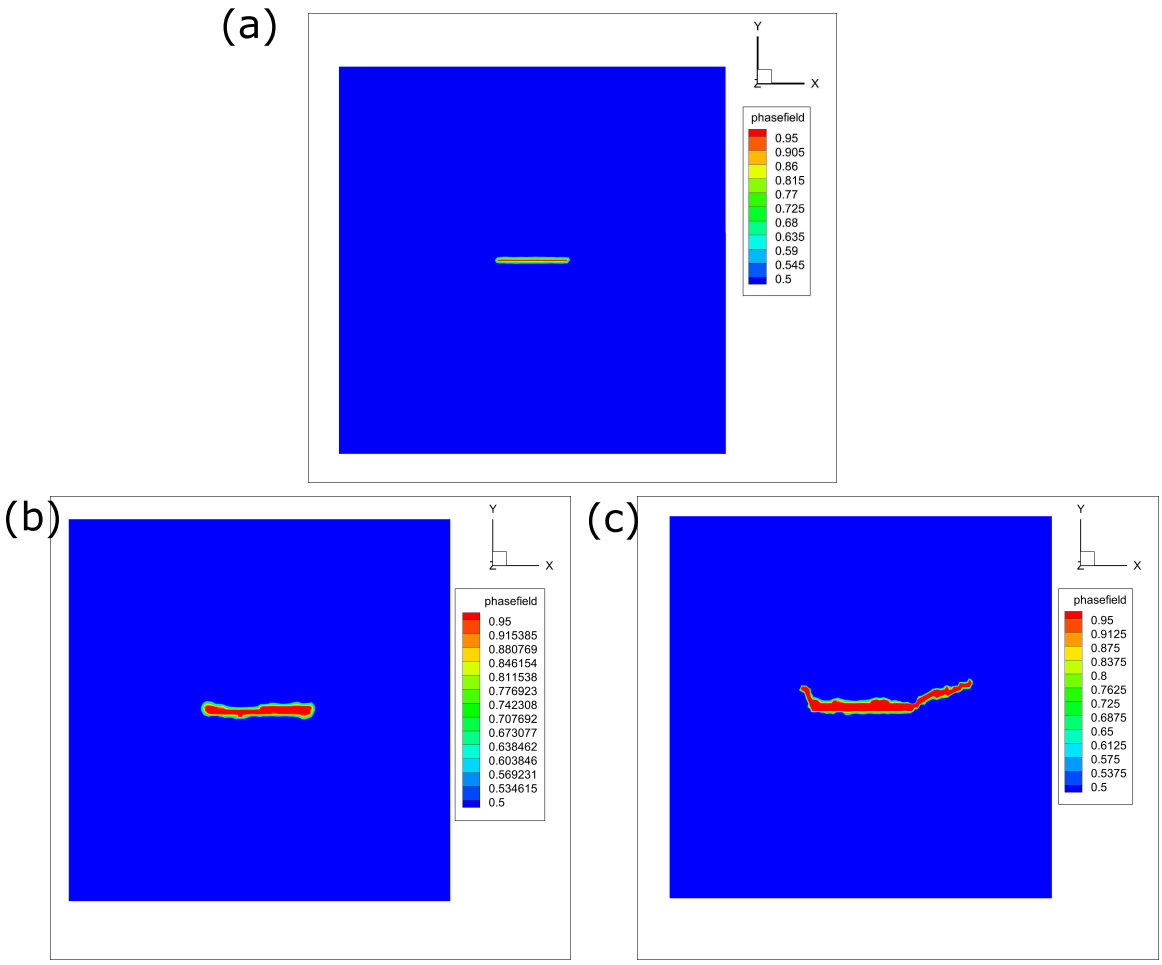

Figure 7.11: Contour plot of the phase-field parameter (s). (a) Initial configuration of the crack. Evolution of the crack at macroscopic strain of $\epsilon_{11} = \epsilon_{22} \approx 3.4\%$ (b)without and (c)with consideration of the additional plasticity contribution from the crack tip.

7.5 Conclusions

In this chapter, the developed concurrent model is used to obtain the evolution of the density of the dislocations nucleating from the crack tip. A predetermined nonlinear form with three material parameters is used to approximate the evolution law. The simulation data from the concurrent model is used to calibrate the material parameters of the evolution law. The calibrated values of the material parameters

are given for two different strain rate viz. $\dot{\epsilon} = 1.0e6$ *and* $5.0e4$.

The obtained evolution law of the nucleated dislocations density is used to investigate the crack propagation within a full continuum phase-field model. A comparative study with the nucleated dislocation density and without it, is used to assess the influence of the nucleated dislocations on the propagation of the crack. It is found that the extra plasticity contributed by the nucleated dislocations has a strong influence on the propagation of the crack. This signifies the importance of quantifying the deformation mechanisms at atomistic accuracy using the concurrent model.

Chapter 8

Conclusion And Future Work

In this dissertation, a concurrent coupled atomistic-continuum multiscale model is developed to study the fracture process in the metallic materials. The model consists of an atomistic region that is modeled using time accelerated Molecular Dynamics(MD) using the modified version of LAMMPS code and a continuum region which is modeled using density-based Crystal Plasticity. Traction reciprocity and displacement compatibility are enforced in the interface region. A selfconsistent incremental iterative scheme is used to solve the governing differential equations to obtain the equilibrium configuration of the coupled system. A new framework is developed to characterize, quantify and transfer the dislocations from the atomistic region to the continuum. DXA is used for the extraction of dislocations from the atomic configuration. A noble propagation model for dislocation in the density form is developed. The propagation model incorporates the advection form of density migration for a

scalar conserved quantity. This model keeps the scalar quantity conserved during the propagation. A particle-based mesh-less method, Reduced Kernel Particle(RKPM), is used for the numerical implementation of the propagation model. For better efficiency, the numerical solution of the propagation model is only invoked in localized regions.

To overcome the high strain rate associated with the conventional MD simulation, the Hyperdynamics based time acceleration is incorporated to accelerate the evolution of the time of the atomistic domain. The effect of the strain rate on the deformation mechanism is demonstrated by using an atomistic model of nickel single crystal with a crack embedded in it. Two specific crack-crystal orientation is used to demonstrate this effect. It has been observed that for some particular crack-crystal orientation there is a change in the deformation mechanism from twin domination at the higher strain rate to dislocation domination at lower strain rate. This also demonstrates the capability of Hyperdynamics to achieve a lower strain rate atomistic simulation. This time acceleration technique is used to match the time-scale between the atomistic and the continuum region after each load increment. This makes sure that both the region in the concurrent model is experiencing the same strain rate.

The developed time accelerated concurrent coupled Atomistic-Continuum model is used to study the crack propagation in metallic materials. A nickel single crystal is used for this study which contains a crack embedded in it. The kinetics of the crack and the evolution of the plastic variable in the form of dislocation density

is extracted from the concurrent model. These evolution laws are extracted in a predetermined parametric form which can be used in the full continuum simulation with a much bigger computational domain. The concurrent model is further used to extract the crucial energetic related to the fracture process such as the 'fracture energy' related to the creation of the new free-surface as crack evolves and the 'defect energy' which is related to the energy associated with the creation of the plastic variable e.g, dislocations. This information related to the fracture-energy and defect-energy are used to augment the construction of the Phase-field free energy functional to study the fracture process within the full continuum scale.

A future possible extension of the present model would be to develop a framework to pass the nucleated twins from the crack tip as it reaches the interface. This is of particular importance for the application of the present concurrent model for HCP crystals e.g, Magnesium, where the twin is one of the most dominant plastic deformation mechanisms. The incorporation of dislocation reaction in the density form is also a feature that will enrich this model.

Bibliography

[1] J. Zhang, S. Chakraborty, and S. Ghosh. Concurrent atomistic-continuum model for developing self-consistent elastic constitutive modeling of crystalline solids with crack. *Int. J. Multiscale Comp. Eng.*, 15:99–119, 2017.

[2] S. Ghosh and J. Zhang. Elastic crack propagation model for crystalline solids using a self-consistent coupled atomistic-continuum framework. *Int. J. Fract.*, 208:171–189, 2017.

[3] S. Keshavarz and S. Ghosh. Hierarchical crystal plasticity fe model for nickel-based superalloys: Sub-grain microstructures to polycrystalline aggregates. *Int. J. of Solids and Structures*, 55:17 – 31, 2015.

[4] J. Knap and Sieradzki K. Crack tip dislocation nucleation in fcc solids. *PRL*, 82(8), 1999.

[5] Y. Mishin, D. Farkas, M. J. Mehl, and D. A. Papaconstantopoulos. Interatomic potentials for monoatomic metals from experimental data and *ab initio* calculations. *Phys. Rev. B*, 59(3393), 1999.

[6] J. Li. Atomeye: an efficient atomistic configuration viewer. *Modelling Simul. Mater. Sci. Eng.*, 11:173–177, 2003.

[7] D.J. Honeycutt and H.C. Anderson. Molecular dynamics study of melting and freezign of small lennard-jones clusters. *J. Chem. Phys.*, 91:4950–4963, 1987.

[8] R. P. Reed, J. H. Smith, and B. W. Christ. The economic effects of fracture in the united states. *Technical report, NATIONAL BUREAU OF STANDARDS*, 1983.

[9] Office of Rail Regulation. Train derailment at hatfield : A final report by the independent investigation board, 2000.

[10] CBC News. Cracks blamed for 2002 china airlines crash, 2002.

[11] Wikipedia. Viareggio train derailment, 2009.

[12] K. Kadau, T.C. Germann, and P.S. Lomdahl. Molecular dynamics comes of age: 320-billion-atom simulation on bluegene/l. *Int. J. Mod. Phys. C*, 17:1755–1761, 2006.

[13] S. J. Zhou, D. M. Beazley, P. S. Lomdahl, and B. L. Holian. Large-scale molecular dynamics simulations of three-dimensional ductile failure. *Phys. Rev. Lett.*, 78(3):479–482, 1996.

[14] V. Yamakov, D. Wolf, S. R. Phillpot, A. K. Mukherjee, and H. Gleiter. Dislo-

cation processes in the deformation of nanocrystalline aluminium by molecular-dynamics simulation. *nature materials*, 1:45–49, 2002.

[15] V. Yamakov, D. H. Warner, E. Zamora, Saether, W. A. Curtin, and E. H. Glaessgen. Investigation of crack tip dislocation emission in aluminum using multiscale molecular dynamics simulation and continuum modeling. *J. Mech. Phys. Solids*, 65:35–53, 2014.

[16] J. Zhang and S. Ghosh. Md based study and characterization of deformation mechanisms near a crack. *J. Mech. Phys. Solids*, 61:1670–1690, 2013.

[17] E. B. Tadmor. *The Quasicontinuum Method*. PhD thesis, Brown University, 1996.

[18] L.E. Shilkrot, R. E. Miller, and W. A Curtin. Coupled atomistic and discrete dislocation plasticity. *Phys. Rev. Lett.*, 89:025501, 2002.

[19] E. Saether, V. Yamakov, and E. H. Glaessgen. An embedded statistical method for coupling molecular dynamics and finite element analyses. *Int. J. for Numerical Methods in Eng.*, 78(11):1292–1319, 2009.

[20] F. Pavia and W. A. Curtin. Parallel algorithm for multiscale atomistic/continuum simulations using LAMMPS. *Model. and Simul. in Mater. Sci. and Eng.*, 23(5):055002, 2015.

[21] S. Badia, P. Bochev, R. Lehoucq, J. Parks, M. Fish, M. A. Nuggehally, and

M. Gunzburger. A force-based blending model for atomistic-to-continuum coupling. *Int. J. for Multiscale Comput. Eng.*, 5(5):387–406, 2007.

[22] R. E. miller and E. B. Tadmor. A unified framework and performance benchmark of fourteen multiscale atomistic/continuum coupling methods. *Model. and Simul. in Mater. Sci. and Eng.*, 17:053001, 2009.

[23] V.B. Shenoy, R. Miller, E.b. Tadmor, D. Rodney, R. Phillips, and M. Ortiz. An adaptive finite element approach to atomic-scale mechanics-the quasicontinuum method. *J. of the Mech. and Phys. of Solids*, 47(3):611 – 642, 1999.

[24] W. K. Kim, M. Luskin, D. Perez, A. F. Voter, and E. B. Tadmor. Hyper-qc: An accelerated finite-temperature quasicontinuum method using hyperdynamics. *J. of the Mech. and Phys. of Solids*, 63:94 – 112, 2014.

[25] S. Chakraborty and S. Ghosh. Hyperdynamics accelerated concurrent atomistic-continuum model for developing crack propagation models in elastic crystalline materials. *Computational Materials Science*, 154:212 – 224, 2018.

[26] L. Xiong, Q. Deng, G. Tucker, D. L. McDowell, and Y. Chen. A concurrent scheme for passing dislocations from atomistic to continuum domains. *Acta Materialia*, 60(3):899 – 913, 2012.

[27] I. Tembhekar, J. S. Amelang, L. Munk, and D. M. Kochmann. Automatic adaptivity in the fully nonlocal quasicontinuum method for coarse-grained atom-

istic simulations. *International Journal for Numerical Methods in Engineering*, 110(9):878–900, 2017.

[28] G. Anciaux, T. Junge, M. Hodapp, J. Cho, J.-F. Molinari, and W.A. Curtin. The coupled atomistic/discrete-dislocation method in 3d part i: Concept and algorithms. *J. Mech. Phys. Solids*, 118:152–171, 2018.

[29] J.S. Amelang, G.N. Venturini, and D.M. Kochmann. Summation rules for a fully nonlocal energy-based quasicontinuum method. *Journal of the Mechanics and Physics of Solids*, 82:378 – 413, 2015.

[30] M. Hodapp, G. Anciaux, J.-F. Molinari, and W.A. Curtin. Coupled atomistic/discrete dislocation method in 3d part ii: Validation of the method. *J. Mech. Phys. Solids*, 119:1–19, 2018.

[31] J. Cho, J. Molinari, W. A. Curtin, and G. Anciaux. The coupled atomistic/discrete-dislocation method in 3d. part iii: Dynamics of hybrid dislocations. *J. Mech. Phys. Solids*, 118:1–14, 2018.

[32] A. Ma and F. Roters. A constitutive model for fcc single crystals based on dislocation densities and its application to uniaxial compression of aluminium single crystals. *Acta Materialia*, 52(12):3603 – 3612, 2004.

[33] A. Ma, F. Roters, and D. Raabe. A dislocation density based constitutive model

for crystal plasticity fem including geometrically necessary dislocations. *Acta Materialia*, 54(8):2169 – 2179, 2006.

[34] Shahriyar Keshavarz, Somnath Ghosh, Andrew C.E. Reid, and Stephen A. Langer. A non-schmid crystal plasticity finite element approach to multi-scale modeling of nickel-based superalloys. *Acta Materialia*, 114:106 – 115, 2016.

[35] S. Keshavarz and S. Ghosh. Multi-scale crystal plasticity finite element model approach to modeling nickel-based superalloys. *Acta Materialia*, 61(17):6549 – 6561, 2013.

[36] D. H. Warner, W. A. Curtin, and S. Qu. Rate dependence of crack-tip processes predicts twining trends in f.c.c metals. *Nature Materials*, 6:876–881, 2007.

[37] S. Hara and J. Li. Adaptive strain-boost hyperdynamics simulations of stress-driven atomic processes. *Phys. Rev. B.*, 82(184114), 2010.

[38] S.J. Plimpton. Fast parallel algorithms for short-range molecular dynamics. *J. Comput. Phys.*, 117:1–19, 1995.

[39] S. Ghosh. *Micromechanical Analysis and Multi-Scale Modeling Using the Voronoi Cell Finite Element Method*. CRC Press/Taylor & Francis, 2011.

[40] U. F. Kocks, A. S. Argon, and A. F. Ashby. *Thermodynamics and kinetics of slip*. Oxford, 1975.

[41] A Arsenlis and D.M Parks. Crystallographic aspects of geometrically-necessary and statistically-stored dislocation density. *Acta Materialia*, 47(5):1597 – 1611, 1999.

[42] J.F Nye. Some geometrical relations in dislocated crystals. *Acta Metallurgica*, 1(2):153 – 162, 1953.

[43] H. Dai. *Geometrically-necessary dislocation density in continuum plasticty theory, FEM implementation and applications*. PhD thesis, Massachusetts Institute of Technology, 1997.

[44] S. Dai and J. C. M. Li. Dislocation-free zone at the crack tip. *Scripta Metallurgica*, 16(2):183 – 188, 1982.

[45] D. Hull and D. J. Bacon. *Introduction to Dislocations*. Elsevier, 2011.

[46] D. W. Lee, H. Kim, A. Strachan, and M. Koslowski. Effect of core energy on mobility in a continuum dislocation model. *Phys. Rev. B*, 83(104101), 2011.

[47] S. Chakraborty, J. Zhang, and S. Ghosh. Accelerated molecular dynamics simulations for characterizing plastic deformation in crystalline materials with crack. *Computational Materials Science*, 121:23–34, 2016.

[48] B. Dunweg and W. Paul. Brownina dynamics simulations without gaussian random numbers. *Int. J. of Modern Physics C*, 02(03):817–827, 1991.

[49] A. F. Voter. Hyperdynamics: Accelerated molecular dynamics of infrequent events. *Phys. Rev. Lett.*, 78(3908), 1997.

[50] A. Stukowski and K. Albe. Extracting dislocations and non-dislocation crystal defects from atomistic simulation data. *Modelling Simul. Mater. Sci. Eng.*, 18:085001, 2010.

[51] J. P. Hirth and J. Lothe. *Theory of Dislocations*. Krieger, 1982.

[52] R. A. Gingold and J. J. Monaghan. Smoothed particle hydrodynamics: theory and application to non-spherical stars. *Monthly Notices of the Royal Astr. Soc.*, 181(3):375–389, 12 1977.

[53] W. K. Liu, S. Jun, and Y. F. Zhang. Reproducing kernel particle methods. *Int. J. for Num. Meth. in Fluids*, 20(89):1081–1106, 1995.

[54] W. K. Liu, Y. Chen, S. Jun, J. S. Chen, T. Belytschko, R. A. Pan, C. Uras, and C. T. Chang. Overview and applications of the reproducing kernel particle methods. *Archives of Comp. Methods in Engg: State of the Art Reviews*, 3:3–80, 1996.

[55] N. R. Aluru. A reproducing kernel particle method for meshless analysis of microelectromechanical systems. *Comp. Mech.*, 23(4):324–338, May 1999.

[56] N. R. Aluru. A point collocation method based on reproducing kernel approximations. *Int. J. for Num. Meth. in Engg.*, 47(6):1083–1121, 2000.

[57] S. Fernndez-Mndez and A. Huerta. Imposing essential boundary conditions in mesh-free methods. *Comp. Methods in Appl. Mech. and Engg.*, 193(12):1257 – 1275, 2004.

[58] S. Beissel and T. Belytschko. Nodal integration of element free galerkin method. *Comp. Methods in Appl. Mech. and Engg.*, 139:49 – 74, 1996.

[59] J. Dolbow and T. Belytschko. Numerical integration of the galerkin weak form in meshfree methods. *Computational Mechanics*, 23(3):219–230, Apr 1999.

[60] Estefania Vidal-Henriquez, Vladimir Zykov, Eberhard Bodenschatz, and Azam Gholami. Convective instability and boundary driven oscillations in a reaction-diffusion-advection model. *Chaos: An Interdisciplinary Journal of Nonlinear Science*, 27(10):103110, 2017.

[61] D. S. Balsara. von neumann stability analysis of smoothed particle hydrodynamicssuggestions for optimal algorithms. *Journal of Computational Physics*, 121(2):357 – 372, 1995.

[62] T. Zhu, J. Li, A. Samanta, A. Leach, and K. Gall. Temperature and strain rate dependence of surface dislocation nucleation. *Phys. Rev. Lett.*, 100(025502), 2008.

[63] A. F. Voter. Parallel replica method for dynamics of infrequent events. *Phys. Rev. B.*, 57(22):R13985(R), 1998.

[64] B. P. Uberusga, S. J. Start, and A. F. Voter. Parallel replica dynamics for driven systems: derivation and application to strained nanotubes. *Phys. Rev. B.*, 75(014301), 2007.

[65] M. R. Sorensen and A. F. Voter. Temperature-accelerated dynamics for simulation of infrequent events. *The J. of Chem. Phys.*, 112(9599), 2000.

[66] A. F. Voter. A method for accelerating the molecular dynamics simulation of infrequent events. *The J. of Chem. Phys.*, 106(4665), 1997.

[67] A. Laio and F. L. Gervasio. Metadynamics : a method to simulate rare events and reconstruct the free energy in biophysics, chemistry and material sciencea. *Rep. on Prog. in Phys.*, 71(126601), 2008.

[68] E. A. Carter, G. Ciccotti, J. T. Hynes, and R. Kapral. Constrained reaction coordinate dynamics for the simulation of rare events. *Chem. Phys. Lett.*, 156:472–477, 1989.

[69] J. Kastner. Umbrella integration in two or more reaction coordinates. *The J. of Chem. Phys.*, 131(034109), 2009.

[70] J. Kastner. Umbrella sampling. *Comp. Mol. Sci.*, 1(6):932–942, 2011.

[71] B. A. Berg and T. Neuhaus. Multicanonical ensemble : A new approach to simulate first-order phase transitions. *Phys. Rev. Lett.*, 156(1):472–477, 1992.

[72] A. Kushima, X. Lin, J. Li, J. Eapen, J. C. Mauro, X. Qian, P. Diep, and S. Yip. Computing the viscosity of supercooled liquids. *The J. of Chem. Phys.*, 130(224504), 2009.

[73] X. Yan, P. Cap, W. Tao, P. Sharma, and H. S. Park. Atomistic modeling at experimental strain rates and timescale. *J. Phys. D: Appl. Phys.*, 49(493002), 2016.

[74] K. L. Baker and D. H. Warner. Extended timescale atomistic modelling of crack tip behavior in aluminum. *Model. and Simul. Mater. Sci. Eng.*, 20(065005), 2012.

[75] H. Eyring. The activated complex in chemical reactions. *The J. of Chem. Phys.*, 3:107, 1935.

[76] D. G. Truhlar and B. C. Garrett. Variational transition-state theory. *Acc. Chem. Res.*, 13(12):440–448, 1980.

[77] E. Vanden-Eijnden and F. A. Tal. Transition state theory: Variational formulation, dynamical corrections and error estimates. *The J. of Chem. Phys.*, 123:184103, 2005.

[78] W. K. Kim and M. L. Falk. A practical perspective on the implementation of hyperdynamics for accelerated simulation. *The J. of Chem. Phys.*, 140:044107, 2014.

[79] A. Miron and K. A. Fichthorn. Accelerated molecular dynamics with the bond-boost method. *The J. of Chem. Phys.*, 119, 2003.

[80] H. Huang, D. Perez, and A. F. Voter. Hyperdynamics boostfactor achievable with an ideal bias potential. *The J. of Chem. Phys.*, 143(074113), 2015.

[81] J. A. Zimmerman, D. J. Bammann, and H. Gao. Deformation gradient for continuum mechanical analysis of atomistic simulation. *Int. J. Solids and Struct.*, 46:238–253, 2009.

[82] W. K. Kim and M. L. Falk. Accelerated molecular dynamics simulation of low-velocity frictional sliding. *Model. and Simul. Mater. Sci. Eng.*, 18:034003, 2010.

[83] D. Perez and A. F. Voter. Accelerating atomistic simulations through self-learning bond-boost hyperdynamics. *LA-UR-08-5519*, 2008.

[84] D. Perez, B. P. Uberuaga, Y Shim, J. G. Amar, and A. F. Voter. Accelerated molecular dynamics methods: introduction and recent developments. *Annual Reports in Computational Chemistry, Elsevier*, 5:1574–1400, 2009.

[85] I. Akio, S. Ogata, H. Kimizuka, and J. Li. Adaptive-boost molecular dynamics simulation of carbon diffusion in iron. *Phys. Rev. B.*, 85(064303), 2012.

[86] S. Nose. A unified formulation of the constant temperature molecular-dynamics methods. *Jour. Chem. Physics*, 81(1):511519, 1984.

[87] W. G. Hoover. Canonical dynamics: Equilibrium phase-space distributions. *Phys. Rev. A*, 31(3):16951697, 1985.

[88] L. Verlet. Computer "Experiments" on classical fluids. I. thermodynamical properties of lennard-jones molecules. *Phys. Rev.*, 159(1):98–103, 1967.

[89] J.E. Angelo, N.R. Moodym, and M.I. Baskes. Trapping of hydrogen to lattice defects in nickel. *Modelling Simul. Mater. Sci. Eng.*, 3(3):289–307, 1995.

[90] Sang Ho Oh, Marc Legros, Daniel Kiener, and Gerhard dehm. In situ observation of dislocation nucleation and escape in a submicrometre aluminium single crystal. *Nature Materials*, 8:95–100, 2009.

[91] P. Haasen. Plastic deformation of nickel single crystals at low temperatures. *Phil. Mag.*, 3:384–418, 1958.

[92] L. Murr and E. Esquivel. Observations of common microstructural issues associated with dynamic deformation phenomena: Twins, microbands, grain size effects, shear bands, and dynamic recrystallization. *J. Mater. Sci.*, 39:1153–1168, 2004.

[93] V. Yamakov, J. D. Hochhalter, W. P. Leser, J. E. Warner, J. A. Newman, G. P. Pujara Pun, and Y. Mishin. Multiscale modeling of sensory properties of co-ni-al shape memory particles enbeded in an al metal matrix. *J. Mater Sci.*, 51:1204–1216, 2016.

[94] G. R. Irwin. Analysis of stresses and strains near the end of a crack traversing a plate. *J. App. Mech.*, 24:361–364, 1957.

[95] T. L. Anderson. *Fracture Mechanics: fundamentals and applications.* CRC press, 2005.

[96] H. Tada, P. C. Paris, and G. R. Irwin. *The stress analysis of cracks handbook.(2nd Ed.).* Paris Production Inc., 1985.

[97] C. Miehe, F. Welschinger, and M. Hofacker. Thermodynamically consistent phasefield models of fracture: Variational principles and multifield fe implementations. *Int. J. Numer. Meth. Engng*, 83:1273–1311, 2010.

[98] A. Shahba and S. ghosh. Coupled phase field finite element model for crack propagation in elastic polycrystalline microstructures. *Comp. Method in App. Mech. and Engg.*, 219:31–64, 2019.

[99] W. R. Tyson and W. A. Miller. Surface free energies of solid metals - estimation from liquid surface tension measurement. *Surf. Sci.*, 62:267–276, 1977.

[100] M. Tanaka, S. Sadamatsu, G. S. Liu, H. Nakamura, K. Higashida, and I. M. Robertson. Sequential multiplication of dislocation sources along a crack front revealed by high-voltage electron microscopy and tomography. *Journal of Materials Research*, 26(4):508513, 2011.

[101] M. Huang, L. Zhao, and J. Tong. Discrete dislocation dynamics modelling of

mechanical deformation of nickel-based single crystal superalloys. *Int. J. of Plasticity*, 28(1):141 – 158, 2012.

[102] C. T. Sun and Z. H. Jin. *Fracture Mechanics*. Elsevier, 2012.

[103] C. B. Carter and S. M. Holmes. The stacking-fault energy of nickel. *The Philosophical Magazine*, 35(5):1161–1172, 1977.

[104] H. J. C. Berendsen, J. P. M. Postma, W. F. van Gunsteren, A. DiNola, and J. R. Haak. Molecular dynamics with coupling to an external bath. *The Journal of Chemical Physics*, 81(8):3684–3690, 1984.

[105] James R. Rice. Dislocation nucleation from a crack tip: An analysis based on the peierls concept. *J. Mech. Phys. Solids*, 40(2):239 – 271, 1992.

[106] K. Sieradzki and R. C. Cammarata. Surface stress effects on the ductile-brittle transition. *PRL*, 73(7), 1994.

[107] J. Cheng, X. Tu, and S. Ghosh. Wavelet-enriched adaptive hierarchical fe model for coupled crystal plasticity-phase field modeling of crack propagation in polycrystalline microstructures. *Comp. Method in App. Mech. and Engg.*, 361:112757, 2020.

Vita

Subhendu Chakraborty is from the state of West Bengal in India. He has completed his undergraduate in the year of 2009 from the Department of Civil Engineering in Jadavpur University(JU), Kolkata. After his undergraduate, he pursued his higher education in the Indian Institute of Science(IISc), Bangalore. There he completed his Master's degree in the year of 2011 from the Department of Aerospace Engineering. The research in his masters was to use Extended Finite Element(XFEM) within the framework of Polygonal Finite Element(PFEM) to study the crack propagation in an anisotropic material. After completion of his maters, he continued in IISc as Project Assistant for two more years. During these two years, he has worked on the atomistic simulation of metallic materials. He subsequently moved to Johns Hopkins University, USA to start his graduate school as a PhD student in the year of 2013 in the Department of Mechanical Engineering. The research topic for his PhD was to develop a concurrent coupled Atomistic-Continuum Model to study the ductile fracture in metallic materials.